Simulation of representative nocturnal satellite imagery for urban areas with high spectral and high spatial resolution

Simulation of representative nocturnal satellite imagery for urban areas with high spectral and high spatial resolution

Master Thesis

Leibniz Universität Hannover
Faculty of Civil Engineering and Geodetic Science
Institute of Photogrammetry and GeoInformation

submitted by

Jasper Kris R. De Meester

Matriculation number: 10006730
Hanover, 30 September 2019

First examiner, Prof. Dr.-Ing. C. Heipke
Second examiner, Prof. Dr. M. Motagh
Supervisor, Dr. T. Storch

Declaration of authorship

I hereby declare that this thesis was entirely my own work and that any additional sources of information have been duly cited.

I certify that, to the best of my knowledge, my thesis does not infringe upon anyone's copyright nor violate any proprietary rights and that any ideas, techniques, quotations, or any other material from the work of other people included in my thesis, published or otherwise, are fully acknowledged in accordance with the standard referencing practices.

I declare that this thesis has not been submitted for a higher degree to any other University or Institution.

Jasper Kris R. De Meester
Hanover, September 2019

Table of contents

List of figures

List of tables

List of acronyms

BOA bottom-of-atmosphere.

BRDF bidirectional reflectance distribution function.

CCT correlated colour temperature.

CIE Commission Internationale de l'Eclairage (International Commission on Illumination).

CRI colour rendering index.

CUMULOS CUbesat MULtispectral Observing System.

CW central wavelength.

DLR Deutsches Zentrum für Luft- und Raumfahrt e.V. (German Aerospace Center).

DMSP Defense Meteorological Satellite Program.

DN digital number.

DNB Day/Night Band.

DoG Difference of Gaussians.

DSLR digital single-lens reflex.

EM electromagnetic.

EROS-B Earth Remote Observation System-B.

EULUMDAT European Lumen Data.

FN false negative.

FP false positive.

FWHM full width at half maximum.

GRD ground resolved distance.

GSD ground sample distance.

IESNA Illuminating Engineering Society of North America.

IFOV instantaneous field of view.

ISS International Space Station.

JLI-3B Jilin-1 03B.

KNN k-nearest neighbour.

LE luminous efficacy.

LED light-emitting diode.

LER luminous efficacy of radiance.

LJ 1-01 Luojia 1-01.

MAE mean absolute error.

MS multispectral.

N8 Nacht/Night.

NER noise-equivalent radiance.

NiteLite Night Imaging of Terrestrial Environments.

NPP National Polar-orbiting Partnership.

OA overall accuracy.

OLS Operational Linescan System.

POV-Ray Persistence of Vision Raytracer.

PSF point spread function.

RGB red-green-blue.

SAC Satélite de Aplicaciones Científicas (Scientific Application Satellite).

SIFT scale-invariant feature transform.

SNR signal-to-noise ratio.

SPICE Spacecraft Planet Instrument Camera matrix Events.

TN true negative.

TOA top-of-atmosphere.

TP true positive.

USGS United States Geological Survey.

VIIRS Visible Infrared Imaging Radiometer Suite.

VNIR visible and near-infrared.

Abstract

Contrary to its daytime counterpart, nighttime visible and near-infrared satellite imagery are currently limited in both spectral resolution and spatial resolution. That does not mean, however, that the relevance of such a sensor is non-existent, with possible applications including the estimation of light pollution, energy consumption and socio-economic information, among others. In order to determine the optimal spectral bands, the required radiometric sampling and the spatial resolution, synthetic top-of-atmosphere spectral radiance values are simulated. These are computed through the combination of lamp spectra libraries, surface reflectance libraries, radiative transfer for the estimation of atmospheric effects, and typical luminance values based on well-established lighting standards.

Various spectral band combinations are then evaluated for their ability to correctly estimate a number of important lighting quality parameters, as well as to discriminate between different lighting types. The tested lighting indicators include (1) luminous efficacy of radiance, or the effiency to produce visible light; (2) spectral G index, which serves as an indicator for emissions in the blue part of the spectrum; and (3) correlated colour temperature, which assesses the perceived colour of a light source. An optimal nanometre-level band selection is found for one panchromatic band and five additional multispectral bands. The selected multispectral bands are located in the blue, green, yellow, orange-red and near-infrared part of the spectrum, respectively, thereby offering a good spread over the full visible and near-infrared part of the spectrum. Since their choice is specifically adjusted to suit the spectra of artificial lights, however, spectral bands differ significantly from the typical daytime situation with the Sun as main illuminator, essentially emitting light equally across the spectrum. Whereas the main interest of daytime optical remote sensing is in surface reflectance, nighttime optical remote sensing focuses on the light sources.

With respect to other nighttime sensor proposals and existing sensors, the recommended spectral bands reduce the estimation error of luminous efficacy of radiance with 73% relatively, the G index error with 86% and the correlated colour temperature error with 68%. Similarly, the classification performance of lighting types improves with about 10%. Based on the generated top-of-atmosphere radiances, detection limits of 10^{-8} to 10^{-7} W m^{-2} sr^{-1} nm^{-1} and saturation values of 10^{-4} to 10^{-3} W m^{-2} sr^{-1} nm^{-1} are recommended for the selected spectral bands. Additionally, results indicate that 12 or more bits are required for information storage.

Finally, some road lighting patterns are simulated using a physically-based rendering software, in order to generate representative imagery. These are then used to determine the required spatial resolution for individual lighting detection. It is found that a ground sample distance of 10 m is required in most cases. Overall,

this thesis shows that significant improvements can be made in terms of the sensor design for nighttime visible and near-infrared remote sensing, opening the door to a new world of applications.

1

Introduction

1.1. Context

Nocturnal optical remote sensing in the visible and near-infrared (VNIR) part of the electromagnetic (EM) spectrum is largely inferior both to its daytime counterpart, as well as to the traditional nighttime remote sensing in the thermal infrared part of the spectrum. Not only is there a large gap in terms of the amount and the diversity of available products, but also in terms of understanding its mechanisms and its potential applications. This does not mean, however, that the demand for such nighttime products is non-existent. Currently, there is a growing interest in optical nighttime products, as is evident from an increasing number of applications [1–3]. These include the monitoring of human settlements and settlement dynamics [4], the estimation of demographic and socio-economic information [5], light pollution and its influence on ecosystems and human health [6, 7], energy consumption and demands [8], detection of gas flares [9], forest fires [10] and fishing vessels [11], natural disaster assessment [12] and the evaluation of political crises and wars [13]. Most of these applications are derived from data linked to artificial nighttime lights, which emit mainly in the VNIR part of the electromagnetic spectrum. A stronger focus on optical nighttime remote sensing is, therefore, well-founded.

Early experiments with taking aerial images at night were already performed during the first World War [14]. However, it wasn't until the emergence of space-borne missions that their potential was realised. Satellite-based observations of artificial light at night were first made possible using low-light imaging data from the Defense Meteorological Satellite Program (DMSP) Operational Linescan System (OLS) in the seventies of the previous century [15]. Although the principal purpose of DMSP-OLS is the determination of a global cloud cover and cloud top temperatures, detecting nocturnal VNIR emission sources has been a widely used by-product ever since [2]. The OLS system, part of the DMSP Block 5D series and first flown in 1976, was the first remote sensing system to be sensitive enough to detect both moonlit clouds and nocturnal light sources at radiances as low as

10^{-8} W m^{-2} sr^{-1} nm^{-1} [16]. This can be ascribed to the intensification of signals from the VNIR band with a photomultiplier tube at night. However, due to its relatively low spatial resolution of almost three kilometres and various other shortcomings [17], the number of nighttime light applications remained limited. Digital archives of DMSP-OLS are available to the public extending from 1992 to 2013.

Sensor	Spatial resolution [m]	Radiometric resolution [bit]	Spectral bands [nm]	Detection limit [W m^{-2} sr^{-1} nm^{-1}]	Coverage	Reference
DMSP-OLS	2700	6	400 - 1100	5×10^{-9}	global, daily	[18]
NPP VIIRS DNB	742	14	505 - 890	2×10^{-10}	global, daily	[2]
SAC-C	300	8	450 - 850	1.5×10^{-6}	global, weekly	[19]
SAC-D	200 - 300	10	450 - 900	1.5×10^{-6}	global, weekly	[20]
CUMULOS	133	10	400 - 900	unknown	target areas	[21]
LJ 1-01	130	12	460 - 980	unknown	global, 15 days	[22]
AeroCubes	120	10	400 - 512 480 - 590 560 - 850	unknown	target areas	[23]
ISS astronaut photographs	10 - 200	14	420 - 500 490 - 585 580 - 640	unknown	target areas	[24]
JLI-3B	0.92	8	430 - 512 489 - 585 580 - 720	7×10^{-6}	target areas	[25]
EROS-B	0.65	10	500 - 900	unknown	target areas	[26]

Table 1.1: Overview of operational and decommissioned VNIR spaceborne nighttime sensors, ranked by their spatial resolution.

October 2011 onwards, a considerable improvement in spatial resolution and detection limits has been made possible with the arrival of its follow-on, the Suomi National Polar-orbiting Partnership (NPP) Visible Infrared Imaging Radiometer Suite

(VIIRS) Day/Night Band (DNB) [27]. Like its predecessor, however, the main focus remains on cloud detection. An overview of other operational and decommissioned satellite-based sources is given in Table 1.1.

Besides satellite-based nighttime images, nighttime optical data comes in the form of photographs taken by astronauts aboard the International Space Station (ISS) [24] or dedicated airborne campaigns [28]. Astronaut photographs of cities at night have been around for decades and are freely available to the public. Whereas early attempts resulted in blurry images because of the long exposure times, ISS's large velocity and vibrations, recent advancements have brought forward spatial resolutions of up to 10 m [18]. An additional advantage is that the images are taken with a digital single-lens reflex (DSLR) camera and, thus, consist of three channels in the visible range. However, the lack of geolocation, consistency, quantitative interpretation and global availability limits the potential of such astronaut images [18]. Another endeavour worth mentioning is the recent Night Imaging of Terrestrial Environments (NiteLite) mission, which focuses on the mapping of nocturnal light pollution from stratospheric high-altitude balloon missions [29].

1.2. Problem statement

Notwithstanding the availability of a number of nightlight data sources, a need for finer spatial and spectral resolutions has been expressed many times [30–32]. For example, a conversion from a high pressure sodium lamp to a white light-emitting diode (LED) is incorrectly observed as a decrease in power by a panchromatic sensor. Despite the proposal for a Nightsat mission by Elvidge et al. [17] in 2007, however, there is still no dedicated nighttime VNIR mission with medium spatial resolution (i.e. around 50 m), multiple spectral bands and global coverage up until today. This might change with the arrival of Nacht/Night (N8), a dedicated optical remote sensing system for nighttime VNIR imagery [33]. While still in its early stages, a feasibility study by Deutsches Zentrum für Luft- und Raumfahrt e.V. (German Aerospace Center) (DLR) shows great promise as a global multi-spectral nighttime low-light mission. In order to determine the optimal characteristics of such a dedicated sensor (i.e. spectral band ranges, spatial resolution and radiometric resolution), it is important to have a better understanding of the different factors at play. However, currently available data provide only panchromatic imagery, are either lacking in spatial or radiometric resolution, have insufficient detection limits or have a limited spatial or temporal coverage (Table 1.1). Hence, these sources cannot satisfactorily determine the optimal parameters required by a future dedicated nighttime mission. Instead, an end-to-end sensor simulation is required to predict optimal sensor performance.

1.3. Objectives

The objective of this thesis is to determine recommended nighttime sensor parameters that are needed to support the science community's requirements, as well as those of the lighting engineering community and the general public, with a main focus on urban environments and the detection and differentiation of artificial outdoor

radiance sources. Natural nighttime radiation sources, such as auroras, bioluminescence and lighting, either occur rarely or have insufficient intensities to be detected by current sensors. For that reason, they are not considered in this thesis. Currently, there is no nighttime satellite data available which ticks all the boxes required to make plausible recommendations for a new nighttime mission (see Section 1.2). Therefore, a first objective of this thesis will be the simulation of reference spectra. In other words, it is important to know which signals arrive at a spaceborne sensor at night, taking into account spectral, spatial and radiometric resolutions. This data can then be utilised to answer the principal question of this thesis: is it possible to discriminate between different radiation sources from spaceborne images, and if yes, at what spectral and spatial resolution? Answering these questions is not as straightforward as one would think. Its complexity exceeds that of the traditional classification task, where the illumination source is known (e.g. sunlight or radar) and the surface object types are unknown. Additionally, in the nighttime case, the illumination source is also unknown. Analogously to daytime imagery, several other components further change the composition of the signal on its way from the light source to the sensor. These include, for example, the interactions with atmosphere and surface. Furthermore, radiances produced by artificial lights are sometimes mixed with moonlight. It is, therefore, important to know how different moon phases affect top-of-atmosphere (TOA) radiances and the discrimination of lighting types. Knowing the type of radiation source can shed light on a number of important light characteristics. Some essential considerations of lighting, however, cannot be linked to lamp type on a one-to-one basis. As a consequence, it is necessary to look at the current dominant criteria in the planning of nighttime lighting, and whether these indicators can potentially be derived from VNIR imagery. Table 1.2 gives a complete summary of the main research questions disscussed in this thesis.

1.4. Methodology

Similar questions to the ones mentioned in Table 1.2 have been investigated previously. For example, Elvidge et al. [34] based their findings on spectrometer measurements of outdoor lighting spectra. However, as only light source spectra have been taken into account, a large part of the complexity is ignored. It neglects, for example, the variability in surface reflectances, atmospheric composition and sensor noise. For instance, two identical LED lamps will look different when illuminating a patch of grass compared to a stretch of road asphalt. Similarly, they will look different under hazy conditions compared to on a clear night. Additionally, the number of spectral band combinations that the authors have tested was limited to eight and does not cover the full range of possibilities. Their recommendations can nonetheless be used as a starting point and reference for this thesis.

In order to perform a realistic and precise examination, two strategies are applied. On the one hand, a spectral library is constructed which combines spectra from different lamp types, different surface types and different atmospheric compositions. The resulting spectra are then subjected to different spectral band combinations and analysed using a multiclass one-vs-all k-nearest neighbour (KNN)

Main question	Sub-question
Can artificial light characteristics be extracted from TOA spectra?	What are the principal indices used in nighttime lighting planning?
	Which indices can be estimated from TOA spectra?
	What are the optimal bands for their estimation?
Can nighttime light source types be identified from top-of-atmosphere (TOA) spectra?	What are the main nighttime light source types?
	How many spectral bands are required for identification?
	What spectral bands are optimal for identification?
	What is the influence of different surface types on identification?
	What is the influence of different atmospheric compositions on identification?
	What is the influence of different moon phases on identification?
	What values are recommended as detection limit and saturation of the sensor?
What spatial resolution is required for lighting type identification?	For typical light source spacing, what is the minimum spatial resolution required to identify individual light sources?
	What is the influence of a light source's distribution pattern?
	To what extent is light type identification hindered by overlapping light sources?

Table 1.2: Overview of main research questions.

classification to identify the light source type. Additionally, a couple of lighting indices are estimated as well. This approach does not, however, take into account any spatial information such as a lamp's intensity distribution pattern or the overlapping of different lights. Therefore, a second additional approach is executed, where satellite imagery is simulated with various spatial resolutions, using a physically-

based rendering software. In this thesis, a modified version of Persistence of Vision Raytracer (POV-Ray) [35], a ray-tracing software which generates images from a text-based scene description, is used. This approach is applied to the simulation of some simple toy examples, hypothetical environments that offer a controlled environment and focus on the understanding of the influence of individual components, e.g. the spacing of different lamps, with respect to spatial resolution.

1.5. Structure

Chapter 2 focuses on the physics and characteristics of nighttime radiation and offers a theoretical background in physically-based rendering and in the different analysis methods that are applied in this thesis. In Section 2.1, the terminology of radiometry and photometry is discussed, giving an insight into the most important physical quantities and their units. Section 2.2 gives an overview of the main nighttime light sources, including different types of artificial lighting, the moon and other nighttime light sources. Section 2.3 discusses the principal lighting quality parameters used in the planning of nighttime lights. Next, the propagation of EM waves from its source to the sensor is described in Section 2.4, along with their fundamental interactions. Section 2.5 describes the conversion from TOA radiances to digital image, including the discussion of spectral, radiometric and spatial resolution. This chapter concludes by explaining the basics of physically-based rendering in Section 2.6 and a description of the different analysis methods that are used in this thesis in Section 2.7.

Chapter 3 presents the reader with the different data sources that are used, in a logical sequence from light source to sensor. These include (i) artificial light source spectra, intensities and intensity distributions; (ii) lunar irradiance modelling; (iii) surface reflectance data; and (iv) radiative transfer modelling.

Chapter 4 focuses on the derivation of the principal parameters for a dedicated VNIR nighttime sensor, i.e. spectral resolution, radiometric resolution and spatial resolution. In order to determine the required spectral bands, a spectral library is set up, which combines the spectra of artificial lights, surface reflectance data and atmospheric transmittance spectra. In other words, it generates theoretical TOA radiances for different lights, surfaces and atmospheric compositions. Based on these spectra, optimal spectral bands are derived for the estimation of lighting quality parameters and radiation source type. After the determination of the optimal band combination, typical TOA radiance values are analysed for different bands, in order to determine the optimal radiometric resolution. While the spectral library focuses on homogeneous single-pixel environments, the toy examples look at some hypothetical two- and three-dimensional environments. They offer the opportunity to focus on the influence of individual factors, such as the distance between lamps, on the resulting image, enabling the determination of the required spatial resolution. This way, an increased understanding of nighttime images at high spatial and spectral resolutions is gradually gained.

Finally, Chapter 5 contains the conclusion, a recommendation for sensor parameters, as well as an overview of possible future research.

2

Background theory

2.1. Terminology

The physics behind nighttime radiation doesn't differ much from its daytime counterpart. There are major differences, however, in what drives the content of the imagery. Compared to the typical daylight situation, there is no uniform light source (i.e. the Sun), which illuminates all objects in a homogeneous manner and would nullify almost all other sources of EM waves in the VNIR part of the spectrum. This leaves room for other light sources to become more apparent, although at lower intensities. Nighttime radiance in the VNIR part of the spectrum is dominated by artificial light sources. With their focus on human vision, it is important to mention the differences between radiometry and photometry. Radiometry is the general field concerned with the measurement of EM waves and their physical quantities [36]. In contrast, photometry additionally takes into account the human perception. Since the human perception is of great importance in the design of artificial light sources, lamp characteristics are predominantly described using photometric terminology. Table 2.1 gives an overview of all relevant radiometric and photometric quantities and units.

2.1.1. Radiometry

Radiometric quantities describe various aspects of EM radiation, e.g. energy, power and power density with respect to direction and area, or both. Radiant energy Q_e is defined by the amount of energy that travels in the form of EM waves, while radiant power or radiant flux Φ_e describes the flow of radiant energy over time and is measured in watts (W).

In order to understand the subsequent quantities, first the concept of solid angles needs to be introduced. Essentially, a solid angle Ω defines how large an object seems from a particular viewpoint. In other words, a small object nearby can have the same solid angle as a large object further away. Solid angles are measured in steradian (sr), with 1 sr corresponding to a surface area of 1 square

Radiometric terminology			Photometric terminology		
Quantity	Definition	Unit	Quantity	Definition	Unit
Radiant energy Q_e		joule [J]	Luminous energy Q_v		lumen second [lm s]
Radiant power Φ_e	$\frac{\partial Q_e}{\partial t}$	watt [W]	Luminous power Φ_v	$\frac{\partial Q_v}{\partial t}$	lumen [lm]
Radiant intensity I_e	$\frac{\partial \Phi_e}{\partial \omega}$	watt per steradian [W sr^{-1}]	Luminous intensity I_v	$\frac{\partial \Phi_v}{\partial \omega}$	candela [cd]
Radiant exitance M_e	$\frac{\partial \Phi_e}{\partial A}$	watt per square metre [W m^{-2}]	Luminous exitance M_v	$\frac{\partial \Phi_v}{\partial A}$	lumen per square metre [lm m^{-2}]
Radiance L_e	$\frac{\partial^2 \Phi_e}{\partial A \partial \omega \cos\theta}$	watt per square metre per steradian [W $m^{-2} sr^{-1}$]	Luminance L_v	$\frac{\partial^2 \Phi_v}{\partial A \partial \omega \cos\theta}$	candela per square metre [cd m^{-2}]
Irradiance E_e	$\frac{\partial \Phi_e}{\partial A}$	watt per square metre [W m^{-2}]	Illuminance E_v	$\frac{\partial \Phi_v}{\partial A}$	lumen per square metre [lm m^{-2}]
Spectral radiance $L_{e\lambda}$	$\frac{\partial L_e}{\partial \lambda}$	watt per cubic metre per steradian [W $m^{-3} sr^{-1}$]	Spectral luminance $L_{v\lambda}$	$\frac{\partial L_v}{\partial \lambda}$	candela per cubic metre [cd m^{-3}]
Spectral irradiance $E_{e\lambda}$	$\frac{\partial E_e}{\partial \lambda}$	watt per cubic metre [W m^{-3}]	Spectral illuminance $E_{v\lambda}$	$\frac{\partial E_v}{\partial \lambda}$	lumen per cubic metre [lm m^{-3}]

Table 2.1: Radiometric and photometric quantities and units. Note that the photometric unit candela equals lumen per steradian.

metre on a sphere with a radius of 1 metre. Since the total surface of this sphere equals 4π square metres, it follows that the total solid angle about a point is 4π sr.

Radiant intensity I, measured in watt per steradian (W sr^{-1}), can then be defined as the radiant power from a point source per unit solid angle in the considered direction. Radiant exitance M, in watt per squared metre (W m^{-2}), is the radiant power per unit area that leaves a surface. A widely used quantity in remote sensing is that of radiance L_e, defined as the radiant power leaving a surface per unit solid angle and per unit projected area. It is measured in watt per square metre per steradian (W m^{-2} sr^{-1}) and is the preferred quantity for sensor images. Irradiance, on the other hand, is the radiant power received by a surface per unit area, measured in

watt per square metre (W m^{-2}). Since most of the above-mentioned quantities are dependent upon wavelength, additional terms, e.g. spectral radiance $L_{e\lambda}$ and spectral irradiance $L_{e\lambda}$, are also of importance for the remaining of this thesis. They represent radiance and irradiance, respectively, per unit wavelength.

2.1.2. Photometry

Photometric quantities, mostly recognised by the prefix *luminous*, can be derived from their radiometric counterparts using Eq. 2.1. Here Φ_v represents luminous power (i.e. the photometric quantity), K_{max} is the greatest luminous efficacy which can theoretically be achieved at 555 nm, equalling 683 lm W^{-1}, $V(\lambda)$ is the Commission Internationale de l'Eclairage (International Commission on Illumination) (CIE) photopic spectral luminous efficiency or the human eye's relative sensitivity under well-lit conditions, and Φ_e represents radiant power (i.e. the radiometric quantity). Note that Φ_v and Φ_e can be replaced by any other photometric or radiometric quantity, respectively.

$$\Phi_v = K_{max} \int_0^\infty V(\lambda) \frac{d\Phi_e(\lambda)}{d\lambda} d\lambda \tag{2.1}$$

It is important to elaborate here on the difference between photopic, scotopic and mesopic vision. Photopic vision is the standard in normal well-lit conditions where the luminance exceeds 3 cd m^{-2}. Under these circumstances, human vision is dominated by the eye's cones, which are good at discriminating different colours. Scotopic vision, on the other hand, is dominated by rods. These rods are more sensitive to light, but are less efficient at discriminating colours, and are, therefore, very effective in low light conditions (i.e. below 0.003 cd m^{-2}). Whereas the highest sensitivity of photopic vision is centred around 555 nm, scotopic vision has its peak around 507 nm (Fig. 2.1). For intermediate luminances, both cones and rods are used, a state called mesopic vision. Since luminances as a result of artificial lighting usually approximate the values for photopic vision, the spectral luminous efficiency curve for photopic vision is frequently used in lighting design.

2.2. Radiation sources

So far, the identification of light source types and intensities from aerial or spaceborne imagery has been challenging due to a limited spatial and spectral resolution. While it is possible to give an extensive overview of the different sources of radiation in the VNIR part of the spectrum, relative worldwide frequencies are difficult to determine. Instead, most research has focused on associating the amount of reflected light with land use classes. One such example is the aerial campaign executed by Kuechly et al. [30] for the city of Berlin. After a thorough analysis of light emission, streets were found to be responsible for 31.6% of the total light emitted, although only covering an area of 13.6%. Other large contributions were coming from industrial areas (15.6%), public service areas (9.6%), block buildings (7.8%) and the city centre (6.3%). The concentration of nighttime radiation around the major transportation axes (Fig. 2.2) hints at the fact that nocturnal light is mostly

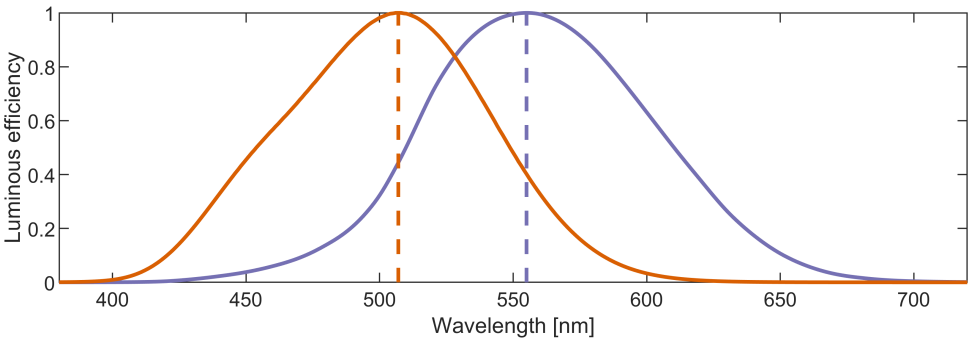

Figure 2.1: CIE photopic (purple) and scotopic (orange) spectral luminous efficiency curves, representing the sensitivity of the human eye to different wavelengths under well-lit and low-light conditions, respectively. Note the bell-shaped forms centred around 555 nm and 507 nm.

restricted to urban areas, in contrast to rural regions. Even though these outcomes do not tell anything on lighting types directly, it shows that artificial lights are the dominant emission sources.

2.2.1. Artificial lights

The sources used by humans to produce lighting have changed drastically throughout history, going from open fires to candles and oil lamps over natural gas to electrical light. An estimate made by the Joint Research Centre of the European Commission [37] shows that, among artificial light sources, high-pressure sodium lights were responsible for about half of the artificial light in the European Union in 2015, although a trend towards the use of LED lights is to be expected in the near future. Below follows an overview of the most common exterior lighting types used today and a description of their principal emission peaks, i.e. those wavelengths for which a particular light emits most of its light.

Incandescent

The incandescent lamp emits light by heating a tungsten filament inside a vacuum enclosed by a glass bulb. When electricity passes through the filament, it heats up, thereby producing a spectrum similar to that of a blackbody of the same temperature. However, these bulbs come with a major shortcoming, as most of the emitted light falls in the infrared part of the spectrum (Fig. 2.3c). Emission for incandescent light bulbs usually peaks around 1000 nm.

High- and low-pressure sodium

High- and low-pressure sodium lamps are a type of gas discharge lamp which use sodium in an excited state. Gas discharge lamps generate radiation by sending electricity through an ionised gas, thereby releasing energy in the form of photons. Different gasses typically result in their own characteristic emission lines. In the case of high-pressure sodium lamps, the strongest is at 819 nm (Fig. 2.3d). Secondary lines lie between 560 nm and 620 nm. Low-pressure sodium lamps have

Figure 2.2: Nighttime image of Berlin, Germany, September 11, 2010. Reprinted from "Aerial survey and spatial analysis of sources of light pollution in Berlin, Germany," by H.U. Kuechly, C.C.M. Kyba, T. Ruhtz, C. Lindemann, C. Wolter, J. Fischer and F. Hölker, 2012, *Remote Sensing of Environment, 126,* p. 44.

an additional outer vacuum surrounded by glass covered with an infrared reflected layer. This limits the emission of infrared light, leaving only a strong emission peak at 589 nm (Fig. 2.3e). Sodium vapour lamps typically emit a bright yellow-orange light.

Mercury vapour

Mercury vapour lamps are another type of gas discharge lamps, using mercury and providing a more blue-green color because of its peak emissions between 540 nm and 580 nm (Fig. 2.3f). In contrast to other discharge lamps, it additionally resembles the curve of an incandescent lamp, with a blackbody peak around 1250 nm [34].

Metal halide

Metal halide lamps are similar to mercury vapour lamps, but with an additional mixture of metal halides added to the mercury. Metal halide lamps generally have a strong peak at 819 nm, with other peaks strongly depending on the composition of the halides [34] (Fig. 2.3g).

Fluorescent

Fluorescent lamps are low-pressure gas discharge lamps using fluorescence to produce radiation. Like with mercury vapour lamps, they make use of mercury gas. However, the inner surface of the glass tube in which the gas resides contains a fluorescent coating of phosphors. This results in two main emission peaks at 544 nm

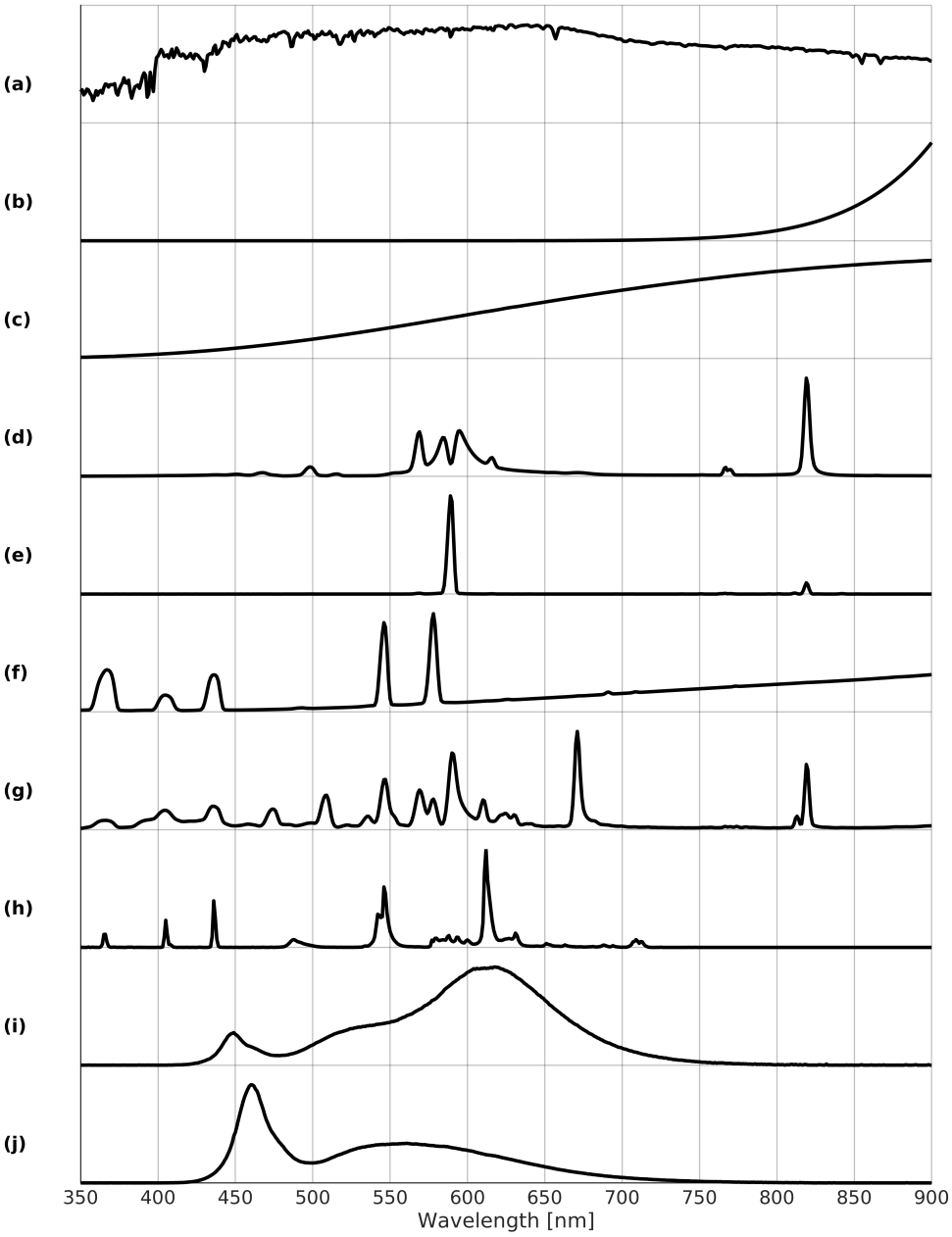

Figure 2.3: Typical emission spectra for different nighttime radiation sources: (a) full moon; (b) fire, 700 K; (c) incandescent bulb; (d) high-pressure sodium lamp; (e) low-pressure sodium lamp; (f) mercury vapour lamp; (g) metal halide lamp; (h) fluorescent lamp; (i) warm LED lamp; and (j) cool LED lamp [34]. Note that the y-axis represents relative radiances.

and 611 nm (Fig. 2.3h). Near-infrared emission are smaller than for mercury vapour lamps.

Light emitting diodes

LED lamps consist of one or more LEDs, which are semi-conductors with electrons moving to a lower energy state when electrical current runs through it, thereby releasing photons. Different types of semi-conductors can be used to create a wide range of colours. Therefore, it is difficult to pinpoint specific emission peaks for LED lamps. They can, however, be identified by relatively narrow symmetrically shaped emission bands and a lack of near-infrared emissions [34]. White LEDs generally have two primary peaks, i.e. one in the blue and another one in the green to red region (Fig. 2.3i-j). Because of their long lifespan and high efficiency, LED lights are becoming more and more the standard for both indoor and outdoor lighting.

2.2.2. Moon

Apart from the artificial light sources mentioned above, there are in fact a number of natural light sources emitting light in the visible part of the spectrum during nighttime. The most prominent of those is the Moon, reflecting sunlight arriving at its surface onto Earth. Hence, the Moon is actually not a light source in itself, but instead acts as a reflecting object. The intensity of moonlight is rather small in comparison to direct sunlight or artificial lighting (see Table 2.2 for comparison). In contrast to artificial lighting, however, the emitted light is not focused, but instead homogeneous across the surface. Therefore, moonlight can become significant, even though its intensity is relatively limited. Additionally, moonlight is crucial in the detection of clouds from DMSP or VIIRS imagery. It also explains the relatively low detection limits of both of these sensors, as their principal focus is on cloud detection. Additionally, moonlight facilitates the possibility to observe snow and ice features from space [38]. Compared to the spectrum of artificial lighting, lunar spectral irradiances are relatively homogeneous across the VNIR spectrum (Fig. 2.3a).

2.2.3. Other

Another relatively common source of nighttime radiation is that caused by fires. Fire emission spectra (Fig. 2.3b) can be described using Planck's law for blackbodies:

$$L_{e\lambda} = \frac{2hc^2}{\lambda^5} \frac{1}{e^{hc/\lambda k_B T} - 1}, \tag{2.2}$$

where $L_{e\lambda}$ represents the spectral radiance, h denotes Planck's constant, c is the speed of light, k_B is Boltzmann's constant and T is the absolute temperature of the material. For typical fires with temperatures ranging between 400 K and 1200 K, emission peaks are located in the thermal infrared part of the spectrum. Other sources, usually less frequent or at lower intensities, include lightning, auroras, gas flares, luminous bacteria and dinoflagellates (i.e. bioluminescence), and skyglow [2] (Fig. 2.4). As the focus is on urban areas, however, the latter sources are not considered during the remainder of this thesis.

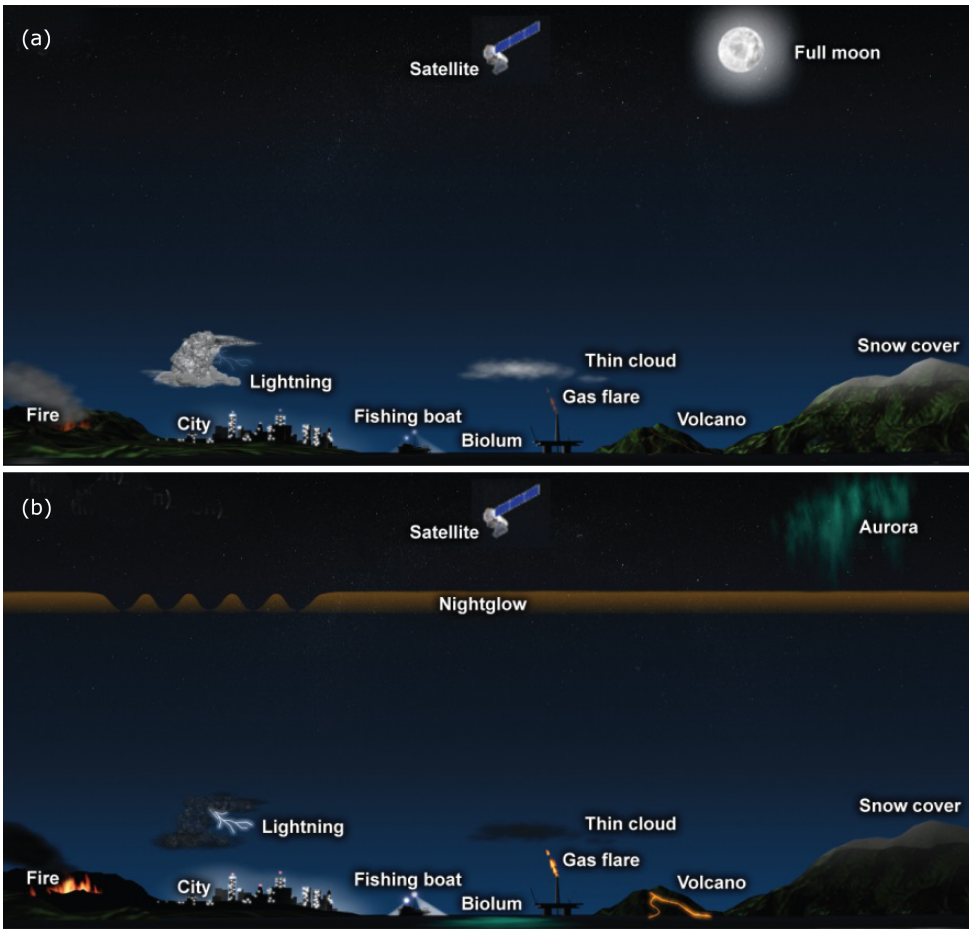

Figure 2.4: Conceptual diagram of observable features at night under different conditions, with (a) full moon conditions; and (b) new moon conditions. Courtesy of Steven Dayo, University Corporation for Atmospheric Research COMET program [39].

Situation	Illuminance [lm m^{-2}]
Full sunlight	103 000
Partly sunny	50 000
Cloudy day	1 000 - 10 000
Main road street lighting	15
Lighted parking lot	10
Residential side street	5
Urban skyglow	0.15
Full moon, cloud-free	0.1 - 0.3
Quarter moon	0.01 - 0.03
Clear starry night	0.001
Overcast night sky	0.00003 - 0.0001

Table 2.2: Typical illuminance values for different situations. Reprinted from "The ecological impacts of nighttime light pollution: a mechanistic appraisal," by K.J. Gaston, J. Bennie, T.W. Davies and J. Hopkins, 2013, *Biological Reviews, 88*(4), p. 913.

2.3. Lighting quality parameters

As it is not effective to share full lamp spectra with consumers, the technical description of artificial lighting generally consists of only a limited number of performance parameters or indices. These define, e.g., how much of the full spectrum can be seen by the human eye, or how much light is emitted in the blue part of the spectrum. Below, the most common spectral indices in lighting engineering are discussed, based on a recent report on road lighting and traffic signals by the Joint Research Centre of the European Commission, put together by researchers and some of the industry's stakeholders [37].

2.3.1. Radiant power

The first light parameter that plays an important role is the intensity or radiant power that corresponds to a certain luminaire system. Its estimation from satellite images, however, is not straightforward, as it depends on a number of different parameters, e.g. surface reflection, atmospheric transmittance and the ratio of emitted power within the measured spectrum. Whereas it is possible to estimate radiant power of lamps, uncertainties remain relatively high, e.g. because of missing aerosol data at high spatial resolutions [40]. Usually, rather than the radiant power, it is the required electrical power that is of interest. However, estimating the latter is further

complicated by the need for data on electrical power efficacy, which describes the ability to transform electrical power into optical power, and the amount of lamp shielding. Advances in this area requires additional research, but remains outside the scope of this thesis. Moreover, such estimations do not depend on the choice of spectral bands and will, therefore, not be discussed further here.

2.3.2. Luminous efficacy

In designing artificial lighting, achieving a high luminous efficacy (LE) is crucial. Luminous efficacy rates the amount of visible light that is produced, in lumen, divided by the total amount electrical power that is required. Therefore, it is a measure for the efficiency of a particular luminaire system. Not only does LE take into account emissions outside of the visual spectrum, but also power losses in control gear or a decreased lumen output as a result of dirt collection on the luminaire. As LE is usually difficult to estimate without any ground-based information, it is often interchanged with luminous efficacy of radiance (LER), which can be computed as the ratio between luminous power Φ_v and optical radiant power Φ_e (Eq. 2.3). Typical LE values for road lighting range from 50 lm W^{-1} for mercury lamps, through 80 lm W^{-1} for fluorescent lamps and 100-140 lm W^{-1} for LED lamps, to 140-170 lm W^{-1} for low-pressure sodium lamps [37]. Values of over 200 lm W^{-1} are expected for future LED road lighting.

$$LER = \frac{\Phi_v}{\Phi_e} = \frac{K_{max} \int_0^\infty V(\lambda) \frac{d\Phi_e(\lambda)}{d\lambda} d\lambda}{\int_0^\infty \frac{d\Phi_e(\lambda)}{d\lambda} d\lambda} \tag{2.3}$$

2.3.3. Spectral G index

Light pollution, especially in the blue part of the spectrum, has gained substantial attention in recent years. Well-known examples are the disruptive effect of artificial lights on the nocturnal behaviour of different species, as well as on human health [6, 7]. For a long time, CCT has been the principal indicator for the amount of emitted blue light, despite its inability to sufficiently describe a lamp's spectrum (see Section 2.3.4). Recently, however, the European Commission's Joint Research Centre has published a report in which it recommends the use of the so-called C(L500,V) or spectral G index instead [37]. This index can be computed as the total amount of luminous power divided by the amount of radiant power emitted between 380 nm and 500 nm (Eq. 2.4), with high values corresponding to low blue light emissions [41]. Note the similarities between the enumerator of this equation and the one of Eq. 2.3. This means that, later on, the enumerator can be estimated by the same spectral band. With most of modern streetlights being non-Planckian radiators, for the remainder of this thesis, more emphasis will be placed on the estimation of the spectral G index, as opposed to estimating CCT.

$$G = 2.5 \log_{10} \frac{\int_0^\infty V(\lambda) \frac{d\Phi_e(\lambda)}{d\lambda} d\lambda}{\int_{380}^{500} \frac{d\Phi_e(\lambda)}{d\lambda} d\lambda} \tag{2.4}$$

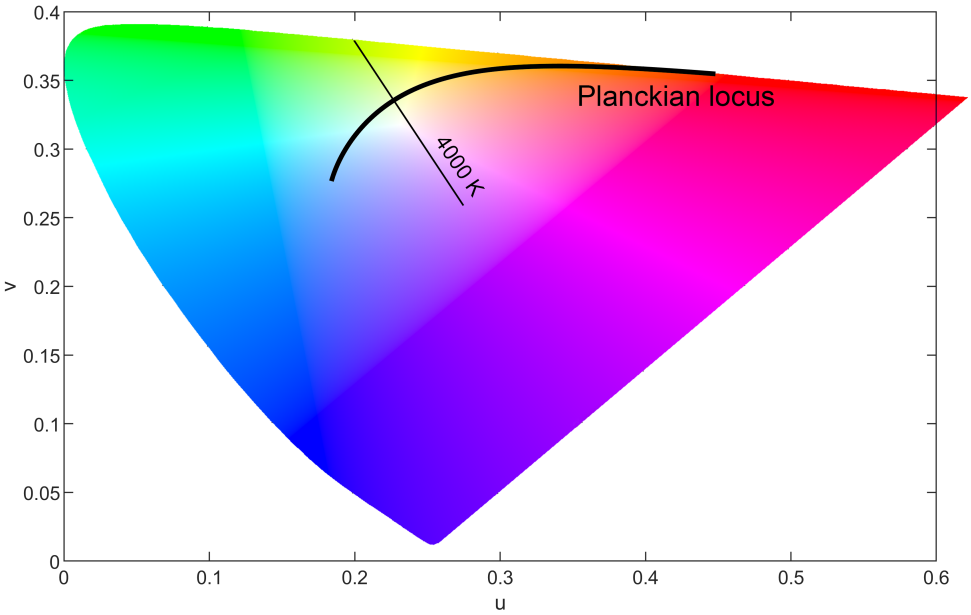

Figure 2.5: CIE 1960 colour space, with the Planckian locus line representing ideal blackbody radiators. The isotherm perpendicular to the Planckian locus represents all positions in the CIE 1960 colour space with a correlated colour temperature of 4000 K.

2.3.4. Correlated colour temperature

In order to assess the perceived colour of the light emitted by a particular lamp, its spectrum is compared to a range of blackbody radiators, which follow Planck's law (Eq. 2.2). The absolute temperature of the blackbody that most closely resembles the spectrum of the lamp, defines the so-called correlated colour temperature (CCT). It needs to be noted that, while the computation of CCT values is relevant for lamps that closely resemble the spectrum of a Planckian source, e.g. in the case of incandescent lamps, it is no longer relevant for other lighting technologies such as discharge lamps or LED lamps. Despite its limited ability to describe a lamps' spectrum, CCT remains a widely applied indicator, as it is relatively straightforward to grasp its meaning.

The computation of the CCT value of a lamp is based on its spectral power distribution, which can in this case be exchanged by its irradiance spectrum $E_{e,\lambda}$ [42]. In a first step, the so-called tristimulus values X, Y and Z are computed using Eq. 2.5-2.7. Here, $\bar{x}$, $\bar{y}$ and $\bar{z}$ represent the CIE's color-matching functions, as given by the CIE. Note that K is chosen, in order for Y to equal 100. In the next step, the chromaticity coordinates x and y in the CIE 1931 coordinate system are computed (Eq. 2.8-2.9). From these, the chromaticity values u and v in the CIE 1960 UCS diagram need to be computed (Eq. 2.10-2.11). Within this diagram (Fig. 2.5), the Planckian radiator whose coordinates are nearest to the computed chromaticity values u and v, determines the temperature, and hence the CCT of the lamp.

$$X = K \cdot \int_0^\infty \bar{x} \cdot E_{e,\lambda} \cdot d\lambda \tag{2.5}$$

$$Y = K \cdot \int_0^\infty \bar{y} \cdot E_{e,\lambda} \cdot d\lambda \tag{2.6}$$

$$Z = K \cdot \int_0^\infty \bar{z} \cdot E_{e,\lambda} \cdot d\lambda \tag{2.7}$$

$$x = \frac{X}{X + Y + Z} \tag{2.8}$$

$$y = \frac{Y}{X + Y + Z} \tag{2.9}$$

$$u = \frac{4x}{-2x + 12y + 3} \tag{2.10}$$

$$v = \frac{6y}{-2x + 12y + 3} \tag{2.11}$$

Another frequently cited parameter to describe a light source's spectrum is that of the colour rendering index (CRI), which expresses a lamp's ability to faithfully reproduce different colours along the spectrum, compared to a blackbody radiator with the same CCT. Typically, incandescent lamps have high CRI values close to the maximum value of 100. Low-pressure sodium lights, on the other hand, have only one narrow peak in its spectrum and, therefore, yield low CRI values, near 0. As has been expressed before by Elvidge et al. [34], estimating CRI requires a very high spectral resolution, which is not cost-effective for current nighttime satellite sensors. As a consequence, the estimation of CRI will not be considered in this thesis.

2.4. Propagation of electromagnetic radiation

In optical radiation, light is modelled as transverse sinusoidal waves, which oscillate electric and magnetic fields perpendicular to the direction of propagation. Hence, they are called electromagnetic (EM) waves. The intensity of radiation that can be measured is encoded in the amplitude of these waves. Once leaving a light source, such EM waves travel to the Earth's surface, interact with the surface or any other object and travel through a whole series of atmospheric layers up to the sensor. When EM waves interact with matter, the electrons, molecules and/or nuclei are put into motion, thereby transferring energy from the wave to the object [43]. Below, the interaction of waves with materials is subdivided into two sections, namely the energy interaction with the Earth's surface (Section 2.4.2) and energy interactions in the atmosphere (Section 2.4.3).

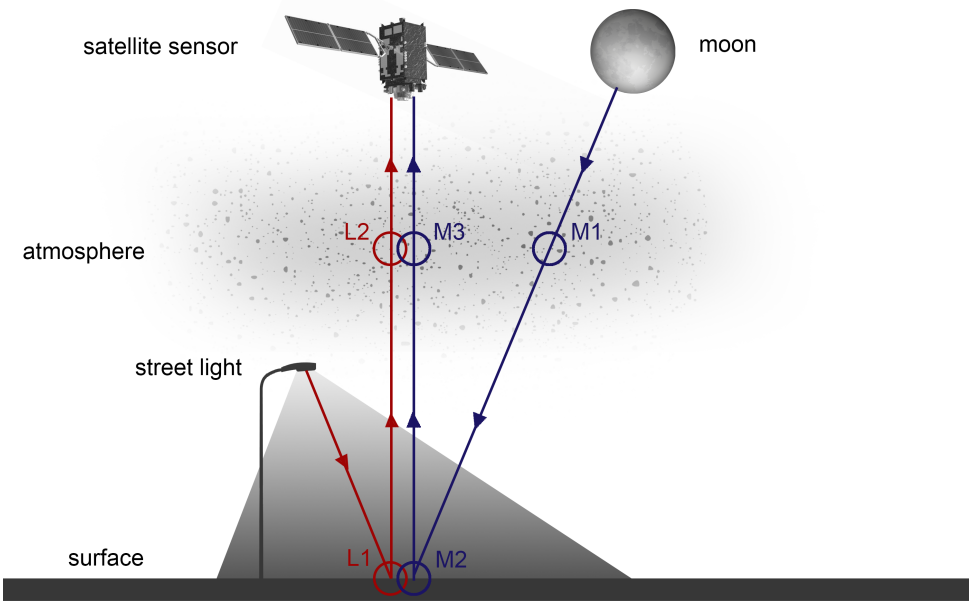

Figure 2.6: Simplified illustration of propagation of nighttime radiation in optical remote sensing, with (L1) surface interaction with lamp EM waves; (L2) upward atmosphere interaction with lamp EM waves; (M1) downward atmosphere interaction with lunar EM waves; (M2) surface interaction with lunar EM waves; and (M3) upward atmosphere interaction with lunar EM waves. Note that only cloud-free conditions are considered.

2.4.1. Pathway

Figure 2.6 represents a simplified illustration of the path of EM waves under cloud-free nighttime conditions. The model consists of two fundamental light sources, i.e. artificial lights or street lights (prefix L) and the Moon (prefix M). Note that, although it is strictly not a light source, the Moon is considered as one for ease of computation. Lunar radiation, a result of reflected sunlight, passes through the Earth's atmosphere twice, as is the case for sunlight in daytime optical remote sensing. Artificial light sources, on the other hand, are usually relatively close to the Earth's surface. Therefore, it can be assumed that only upward paths are of importance, restricting the atmospheric transmission problem to a conversion from bottom-of-atmosphere (BOA) radiances to top-of-atmosphere (TOA) radiances. Contrary to the presented diagram (Fig. 2.6), it needs to be noted that real-world environments are much more complex, since waves can be scattered, absorbed or reflected multiple times, the Earth's atmosphere is not a homogeneous or static environment, the cloud-free assumption usually doesn't hold and path radiance or adjacency effect are not considered. For the determination of optimal spectral and spatial resolutions, however, a simplified model of EM wave propagation is sufficient.

2.4.2. Surface interaction

When incident EM waves come into contact with the Earth's surface, their energy may be absorbed, transmitted or reflected. The proportion of each of these energy interactions strongly depends on both wavelength and material characteristics. For example, two different materials (e.g. grass and asphalt) look different in a satellite image as a result of different material properties. Similarly, a patch of grass reflects a different amount of red light compared to green light. A widely used characteristic of surface features is spectral reflectance, which measures the amount of reflected energy with respect to the amount of incident energy as a function of the wavelength.

Another important consideration is the direction in which incoming energy is reflected. This depends mostly on the roughness of the object, where specular reflectors and diffuse reflectors can be distinguished. Specular reflectors are flat surfaces that result in mirror-like reflections. In other words, light is reflected in a single direction, with the reflection angle equalling the incidence angle. Diffuse or Lambertian reflectors, on the other hand, are rough surfaces that reflect uniformly in all directions. Most real-world surfaces or objects are neither perfectly specular nor perfectly Lambertian and are a combination of both. Therefore, it is obvious that spectral reflectance curves do not fully grasp the complexity of surface interaction, as they usually don't take the incidence angle of incoming light and the viewing angle into consideration. For this reason, the bidirectional reflectance distribution function (BRDF) was introduced (Eq. 2.12), with f_r representing the BRDF, L_r the reflected radiance, E_i the incoming irradiance, ϕ_r and θ_r the azimuth and zenith angle of the reflected radiance, respectively, and ϕ_i and θ_i the azimuth and zenith angle of incoming light. As radiance is measured in W m^{-2} sr^{-1} and irradiance in W m^{-2}, the BRDF has the unit sr^{-1}.

$$f_r = \frac{dL_r(\phi_r, \theta_r)}{dE_i(\phi_i, \theta_i)} \tag{2.12}$$

Deriving BRDF values from spaceborne or airborne sensors, however, is not straightforward. Instead, the assumption that all surface objects are perfect Lambertian reflectors is applied in most cases. In other words, the incoming light is assumed to reflect equally in all directions and the direction from which the light is coming is of no importance. This allows for the complex BRDF to be replaced by the rather uncomplicated determination of spectral reflectance. It has to be noted, however, that this simplification does not always stroke with reality. One such case is the example of a wet road surface, which closely resembles a purely specular reflector. As the presence of wet road surfaces is highly correlated with the presence of clouds, and only cloud-free optical imagery are taken into account, this effect has only limited implications and can, thus, be neglected.

2.4.3. Atmosphere interaction

After interacting with the surface and assuming there is no path radiance, the reflected EM waves continue on their path to the sensor through different layers of the atmosphere, i.e. troposphere, stratosphere, mesosphere, thermosphere and exo-

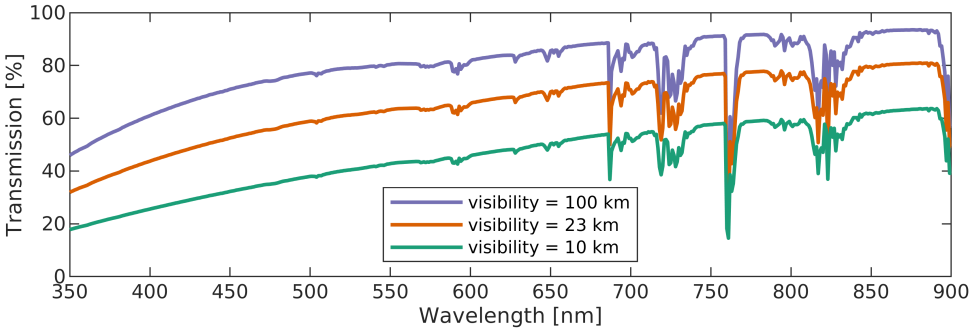

Figure 2.7: Variation in atmospheric transmission curves for a mid-latitude summer atmosphere with urban aerosol model at sea level.

sphere. Here, three fundamental interactions can occur: transmission, absorption and scattering. Whereas scattering changes the direction of the waves, absorption and transmission determine the amount of energy that passes through the atmosphere. Various molecules, such as water vapour, carbon dioxide and ozone, can absorb EM energy and convert it into other forms of energy. As a consequence, the energy does no longer reach the sensor and information is lost. Different constituents absorb energy of different wavelengths. Their cumulative effect causes the atmosphere to become almost completely impenetrable in certain wavelength ranges (Fig. 2.7). Absorption can vary strongly for different atmospheric conditions. For example, the amount of water vapour above the tropics is significantly larger than the amount above the poles. Hence, for wavelengths prone to absorption by water vapour, transmission will be lower above tropical regions.

Atmospheric scattering, or diffusion of radiation by atmospheric particles, can severely reduce the information content of remote sensing data as EM waves are redirected from their original path. This leads to an uncertain origin of the sensed radiation. Three different types of scattering take place, i.e. Rayleigh scattering, Mie scattering and non-selective scattering. Rayleigh scattering is dominant when atmospheric particles interact with waves that have a wavelength much larger than the size of the particle. Such particles include tiny dust specks, nitrogen and oxygen. Shorter wavelengths are more affected by Rayleigh scattering than longer wavelengths, as the effect is inversely proportional to the wavelength. This causes RGB satellite images to look blue when taken from a high altitude. Additionally, it reduces the contrast of spaceborne images. When the size of the particles is similar to the wavelength (e.g. pollen, dust or smog), Mie scattering occurs. In contrast to Rayleigh scatter, Mie scatter affects more the wavelengths from near-ultraviolet to mid-infrared and is especially significant during overcast conditions. In such conditions, it produces a general haze in the image. Lastly, non-selective scattering comes about when the particles are much larger than the wavelength, as is the case, e.g., for water droplets in clouds. As non-selective scattering is independent of the wavelength in the VNIR part of the spectrum, with equal quantities of blue, green, red and near-infrared light scattered, clouds appear white in VNIR images.

2.5. Optical imaging system

2.5.1. Spectral sampling

Optical systems have the purpose of producing a radiance image on the focal plane array of an imaging system from incoming EM waves. In the case of multi-spectral imaging, it does so in different spectral bands, with each band sensitive to a particular range of wavelengths. This can be seen as a form of spectral sampling, with the smallest difference in wavelengths that can be distinguished, to be interpreted as its spectral resolution. To compute the signal that arrives at a sensor, through combining radiances from different wavelengths, there are two options, i.e. the band-integrated radiance and the band-averaged spectral radiance. The band-integrated radiance L_{band}, defined as the peak normalised effective radiance value over the detector bandpass, can be computed by applying

$$L_{band} = \int_0^\infty L_{e\lambda} \cdot R_{\lambda,band} \cdot d\lambda, \tag{2.13}$$

where $L_{e\lambda}$ represents the spectral radiance and $R_{\lambda,band}$ is the instrumental spectral response function or slit function for a given band [44]. It is measured in W m^{-2} sr^{-1}. The band-averaged spectral radiance $L_{\lambda,band}$, on the other hand, is the weighted average of the normalised effective radiance value over the detector bandpass (Eq. 2.14) and is measured in W m^{-2} sr^{-1} nm^{-1}. As the band-averaged spectral radiance is better at comparing radiance values across different bands, it is generally the preferred variable.

$$L_{\lambda,band} = \frac{\int_0^\infty L_{e\lambda} \cdot R_{\lambda,band} \cdot d\lambda}{\int_0^\infty R_{\lambda,band} \cdot d\lambda} \tag{2.14}$$

Slit functions are difficult to be synthesised accurately beforehand. As a general rule, however, such filters are described by an analytical function which behaves as a combination of a rectangular function and a Gaussian function. Commonly, a so-called symmetric 'super-Gaussian' function of the form

$$R_\lambda = 2^{-\left|2\frac{\lambda-\lambda_c}{\Delta\lambda}\right|^k} \tag{2.15}$$

is used, where λ_c represents the central wavelength (CW) of the band, $\Delta\lambda$ is the full width at half maximum (FWHM) or bandwidth and k denotes a parameter which defines the shape of the function [45]. For high k values, the function resembles a rectangular function, while for k values close to 2 the Gaussian function is approximated. For optical remote sensing purposes, k = 6 usually results in realistic slit functions (Fig. 2.8) [46].

2.5.2. Noise model

The signal that constitutes an optical satellite image does not only contain radiances originating from the light sources mentioned in Section 2.2. Additionally, it might include background radiances from sunlit objects in the case of relatively

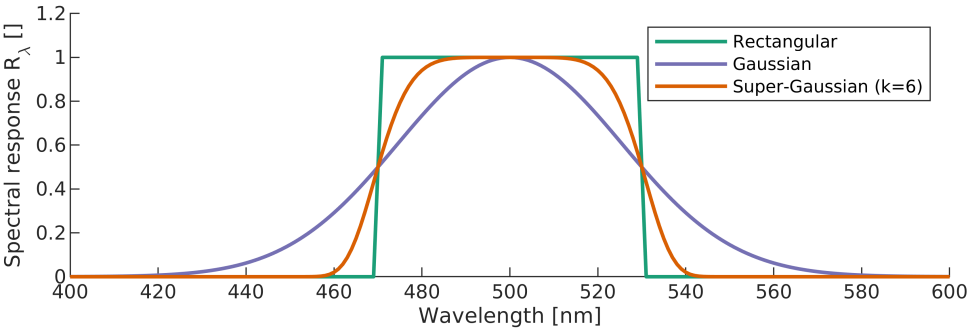

Figure 2.8: Different analytic slit functions for a band with a central wavelength of 500 nm and an FWHM of 60 nm.

low solar zenith angles, stray light in case the satellite is directly lit by sunlight, and high energy particles. Moreover, noise can be introduced during the charge transfer process caused by detectors and electronic devices. Here, the focus lies on radiometric or system noise because other noise sources, such as straylight, are relatively straightforward to model. To compare the amount of desired signal power to the level of background noise, signal-to-noise ratio (SNR) is defined as

$$SNR = \frac{N_{signal}}{N_{noise}}, \tag{2.16}$$

where N_{signal} and N_{noise} are the signal electron number and noise electron number, respectively. The largest radiometric noise contribution is a result of the random incidence of photons, thereby randomly generating photo-generated electrons. This type of noise is called photon shot noise σ_{photon}, measured in electron number. Assuming photon shot noise to be dominant and other contributions negligible, the noise electron number can be rewritten as the square root of the signal electron number (Eq. 2.17), thereby obeying a Poisson distribution [47]. The signal electron number N_{signal} itself can be found by converting the incoming spectral radiance to electron content (Eq. 3.2), with A being the detector's effective area, equalling the pixel area times the pixel's fill factor, τ is the system's optical transmittance, η is the quantum efficiency, t is the integration time, $f/\#$ is the f-number, h is Planck's constant and c is the speed of light [48]. Typical sensor values for a nighttime VNIR sensor are given in Table 2.3.

$$N_{noise} \approx \sigma_{photon} = \sqrt{N_{signal}} \tag{2.17}$$

$$N_{signal} = \frac{L_{\lambda,band} \cdot A \cdot \pi \cdot \tau \cdot \eta \cdot t \cdot \Delta\lambda \cdot \lambda_c}{(4(f/\#)^2 + 1) \cdot h \cdot c} \tag{2.18}$$

The so-called noise-equivalent radiance (NER), i.e. the amount of noise measured in W m^{-2} sr^{-1} nm^{-1}, can then be defined as

$$NER = N_{noise} \cdot \frac{\left(4(f/\#)^2 + 1\right) \cdot h \cdot c}{A \cdot \pi \cdot \tau \cdot \eta \cdot t \cdot \Delta\lambda \cdot \lambda_c}$$
$$\approx \sqrt{\frac{L_{\lambda,band} \cdot A \cdot \pi \cdot \tau \cdot \eta \cdot t \cdot \Delta\lambda \cdot \lambda_c}{(4(f/\#)^2 + 1) \cdot h \cdot c}} \cdot \frac{\left(4(f/\#)^2 + 1\right) \cdot h \cdot c}{A \cdot \pi \cdot \tau \cdot \eta \cdot t \cdot \Delta\lambda \cdot \lambda_c} \tag{2.19}$$
$$= \sqrt{\frac{L_{\lambda,band} \cdot (4(f/\#)^2 + 1) \cdot h \cdot c}{\Delta\lambda \cdot \lambda_c \cdot A \cdot \pi \cdot \tau \cdot \eta \cdot t}}$$

meaning that the NER depends on the square root of the band-averaged spectral radiance $L_{\lambda,band}$, and on the inverse square root of both the FWHM $\Delta\lambda$ and CW λ_c.

2.5.3. Radiometric sampling

Assuming detectors have a linear response, the conversion from an incoming band-averaged spectral radiance $L_{\lambda,band}$ to a digital number (DN) is computed using

$$DN = \left(L_{\lambda,band} - b\right) \cdot c^{-1}, \tag{2.20}$$

where

$$b = L_{min}, \quad c = \frac{L_{max} - L_{min}}{DN_{max}}, \tag{2.21}$$

with b and c denoting the offset and gain of the system, respectively. L_{min} and L_{max} represent the detection limit and the saturation of the sensor, while DN_{max} is the maximum digital number that can be attained (e.g. 255 for 8 bit images). The radiometric resolution of a sensor system can be defined as both the amount of bits that is used for storage, as well as the radiance which corresponds to a single DN.

2.5.4. Spatial sampling

Similar to the spectral and radiometric cases, spatial resolution can be seen as a form of sampling, i.e. a form of sampling of the ground surface. Primarily, the definition of ground sample distance (GSD) is used, which defines the distance at the surface between two adjacent pixel centres. This metric does not, however, necessarily act as an accurate surrogate for spatial resolution. For example, an image can be spatially oversampled and contain closely spaced, but blurry pixels. Therefore, ground resolved distance (GRD) should be considered additionally. It defines the geometric size of the smallest object which can be detected by a sensor [48]. This measure depends heavily on the so-called point spread function (PSF) of a sensor, which characterises its response to a point source. Based on the definition of PSF, the instantaneous field of view (IFOV) can be interpreted as the angle α between specified cutoff levels of the PSF. The GRD, then, represents the geometric projection of this IFOV on the ground surface. With most remote sensing systems designing the pixel spacing (i.e. GSD) closely resembling the GRD, both can usually be interchanged without much issues.

Variable	Value
Band-averaged spectral radiance	250 W m^{-3} sr^{-1}
Pixel pitch	$7 \cdot 10^{-6}$ m
Pixel fill factor	0.95
Effective area	$4.66 \cdot 10^{-11}$ m^2
Optical transmittance	0.8
Quantum efficiency	0.85
Integration time	$2.2 \cdot 10^{-3}$ s
Time delayed integration	256
Effective integration time	$5.63 \cdot 10^{-1}$ s
Bandwidth	$100 \cdot 10^{-9}$ m
Central wavelength	$560 \cdot 10^{-9}$ m
F-number	2.5
Projected solid angle	$1.21 \cdot 10^{-1}$ sr
Planck's constant	$6.63 \cdot 10^{-34}$ W s^2
Speed of light	$3.00 \cdot 10^{8}$ m s^{-1}
Signal	160 e^-
Photon shot noise	12.6 e^-

Table 2.3: Example computation of signal electron content and photon shot noise for a typical nighttime situation, based on Elvidge et al. [17] and IMEC's CCD-in-CMOS multispectral sensor [49].

2.6. Physically-based rendering

Rendering is a part of computer graphics that deals with generating, or rendering, a two-dimensional image from a textual description of, e.g., a virtual camera, three-dimensional objects and light sources [50]. The appearance of the objects in the final image is determined by different characteristics, including material properties, textures and shading properties. The field of rendering is especially popular in product design, architecture, advertising, computer games and movies. As a subfield of rendering, physically-based rendering focuses on accurately resembling the propagation of light as it takes place in reality. Its ultimate goal is to generate an image that is indistinguishable from a photograph of the same scene. There-

fore, physically-based rendering is the fitting tool for generating realistic nighttime satellite imagery at high spatial and spectral resolutions. In this thesis, Persistence of Vision Raytracer (POV-Ray) is the rendering software of choice. For a full description of the software and its possibilities, readers are referred to the POV-Ray manual [51].

2.6.1. Rendering equation

The rendering equation (Eq. 2.22) forms the foundation of physically-based rendering and global illumination algorithms [52]. In essence, it illustrates the transport of light using a recursive integral equation. It describes, in other words, the total amount of outgoing radiance L_o from a point **p** along a viewing direction **v**, given a function for the incoming radiance L_i (Eq. 2.23) and a BRDF $f(\mathbf{l},\mathbf{v})$. Here, L_e represents the emitted radiance from a surface at point **p**, **l** is the incoming direction, Ω the hemisphere of directions above **p**, $(\mathbf{n}\cdot\mathbf{l})^+$ the dot product between **n** and **l** with negative values replaced by zero, and $r(\mathbf{p},\mathbf{l})$ a ray tracing function which returns the location of the first surface point which is hit by a traced ray from **p** in direction **l**. Essentially, Equation 2.23 means that the radiance coming into a point **p** along direction **l** is equal to the radiance going out from some other point in the opposite direction -**l**. Hence, it is a recursive term computed ad infinitum. Algorithms, therefore, need some kind of stopping conditions. An important property of the rendering equation is its linearity with respect to the emitted radiation. It is linear in the sense that if a certain light source becomes twice as strong, the lit object's radiance will have doubled as well.

$$L_o(\mathbf{p},\mathbf{v}) = L_e(\mathbf{p},\mathbf{v}) + \int_{\mathbf{l}\in\Omega} f(\mathbf{l},\mathbf{v}) L_i(\mathbf{p},\mathbf{l})(\mathbf{n}\cdot\mathbf{l})^+ d\mathbf{l} \tag{2.22}$$

$$L_i(\mathbf{p},\mathbf{l}) = L_o(r(\mathbf{p},\mathbf{l}),-\mathbf{l}) \tag{2.23}$$

Solving the full rendering equation, however, is not a simple task. Algorithms that solve it can create extremely photorealistic images. At the same time, they are also computationally very expensive. Two of the most common ways of solving the rendering equation are finite element methods (e.g. the radiosity method) and Monte Carlo methods (e.g. the ray tracing method). POV-Ray has the possibility to use a combination of both approaches. Below, the two approaches are briefly described.

2.6.2. Ray tracing

Ray tracing is the most widely used Monte Carlo technique used for solving the rendering equation. In general, Monte Carlo integration schemes use random numbers in order to evaluate integrals, with the expected value exactly equalling the value of the integral. As is the case with Monte Carlo techniques, a physically correct image can thus be generated as long as the algorithm runs for a long enough time. As the name implies, ray tracing uses the tracing of rays to determine the transportation of light between different scene elements. However, in contrast to the direction of light waves in the real world, ray tracing is done backwards. This means that rays

start at the camera and are shot out into the scene. The reason for this is that the vast majority of light waves coming from a source never hit the camera. In that case, precious computation time would be wasted on rays that do not even contribute to the final image. However, as only an estimate of the integral is computed, many rays are needed to compute reliable results. Too few rays will usually result in noisy images.

After a certain ray leaves the camera, information is required on the location of the first intersection point, the amount of incident light and how this incident light is scattered by an object [53]. Computing the intersection between the ray and the closest object is relatively straightforward, by computing the intersection point with different objects and retaining only the nearest object. Secondly, the amount of incident light at the intersection point is computed. In order to do this, it should be determined by which light sources the point is lit, using so-called shadow rays (i.e. rays from the intersection point to the different light sources) to check whether intersections can be found (i.e. the point is in the shadow) or not. For each light, the differential irradiance dE_e at a point with a tiny surface patch dA can then be computed using Eq. 2.24. The radiant power of the light source is represented by Φ_e, r is the distance from the intersection point to the light source and θ is the angle between the surface normal and the vector between the surface point and the light source. Equation 2.24 is thus a combination of the falloff of light with distance and the falloff of light for tilted surfaces.

$$dE_e = \frac{\Phi_e cos\theta}{4\pi r^2} \tag{2.24}$$

After determining the amount of light reaching the intersection point, it is important to find out how the light is scattered by the object at the intersection point. This can be done using the BRDF, as described previously in Section 2.4.2. It is now possible to determine the amount of light energy that is scattered back to the camera. Additionally, the recursive nature of Monte Carlo techniques makes it possible to include indirect light transportation. Each image location can thus be associated with a whole tree of rays. For more detailed information on ray tracing, readers should refer to Pharr et al. [53].

2.6.3. Radiosity

Ray tracing does have a couple of limitations though. For example, it has problems with simulating diffuse inter-reflections and soft shadows [54]. A finite element method called radiosity was developed to simulate light bouncing between diffuse surfaces, thus solving the issue ray tracing has. The radiosity method is named after the radiometric quantity radiosity, which is computed in the process. Radiosity is similar to radiant exitance, but whereas radiant exitance is the radiant flux emitted by a surface per unit area, radiosity is the radiant flux leaving (i.e. emitted, reflected and transmitted) a surface per unit area. In the radiosity method, the scene is subdivided into different surface elements and for each element radiosity is calculated using Eq. 2.25-2.26 [50].

$$B_i = B_i^e + \rho_{ss} \sum_j F_{ij} B_j \tag{2.25}$$

$$F_{ij} = \frac{1}{A_i} \int_{A_i} \int_{A_j} V(i,j) \frac{cos\theta_i cos\theta_j}{\pi d_{ij}^2} dA_i dA_j \tag{2.26}$$

Here, B_i and B_j represent the radiosity of surface elements i and j, respectively, B_i^e is the radiant exitance emitted by surface element i and ρ_{ss} is the subsurface albedo. F_{ij} denotes the form factor of i and j, representing the fraction of uniform diffuse radiant energy that leaves i and is incident upon j [50]. The area of surface elements i and j is denoted by A_i and A_j, respectively, and $V(i,j)$ represents the visibility function between i and j, equalling one if nothing is blocking the light between the two surfaces and zero otherwise. Finally, the angles θ_i and θ_j correspond to the angles between the respective normal and the vector connecting i and j. After the computation of radiosity values for different surface elements, they are usually smoothed out for better results. Because of the long computation times for complex scenes, radiosity is usually limited to very specific cases.

2.7. Analysis techniques

2.7.1. Spectral analysis

One-versus-all k-nearest neighbours

In order to classify different radiation sources into its respective type, sensor data is compared to a reference spectral library (i.e. training data) with the means of a k-nearest neighbour (KNN) classification. Put simply, a particular radiation source is labelled with the same class as the majority of its k nearest neighbours in feature space. In order to determine the distance, Euclidean distance is the most frequent measure. The reason for using KNN is manifold. For example, the method has very limited training time and additionally produces reliable results, since performing the same classification task will result in identical results repeatedly. The latter is an important advantage over other classifiers, since the goal in this thesis is not to find the best possible classifier. Rather, the classification method should serve as a comparison measure to judge the usefulness of a particular spectral band combination.

One of the main disadvantages of applying a KNN classifier is that adding additional features might deteriorate the overall classification performance, even if it improves the classification of one of the classes. For example, if adding a particular spectral band improves the classification of lamp type one, it might generate large Euclidean distances for other lamp types because of large variances in this band. This disadvantage can, however, be overcome by making a small adjustment to the traditional KNN. With the band-averaged spectral radiances considered as features, a KNN classification is applied to each possible combination of features individually. Then, for each radiation source type, the best feature combination is determined by withholding the combination with the highest classification performance. To combine the resulting binary one-versus-all classification results, a weighted voting is

performed, with the classification performance used as weights. In other words, if a particular lamp is classified as both type one and type two, the one with the best performing classifier will be deciding. For the case where a lamp is not classified as any of light source types, it is labeled as 'no class'.

Classification performance metrics

The so-called confusion matrix (Table 2.4) is used as a starting point for most performance metrics, in particular for the concepts of true positive (TP), true negative (TN), false positive (FP) and false negative (FN). Note that, in this context, 'positive' means that a particular instance belongs to a class. For example, the number of TP's is defined by the number of correctly predicted positives, while the number of TN's is the number of correctly predicted negatives.

	Positive (ground truth)	Negative (ground truth)
Positive (predicted)	True positive (TP)	False positive (FP)
Negative (predicted)	False negative (FN)	True negative (TN)

Table 2.4: Principle of the confusion matrix, true positive, true negative, false positive and false negative.

Frequently used is the accuracy metric, which measures the number of correctly predicted instances, with respect to the total number of instances (Eq. 2.27). However, considering this metric on its own, does not provide sufficient information, especially in the case of imbalanced datasets. For example, when creating a classifier which predicts the presence of a disease, which has a prevalence of only 0.1%, a classifier which predicts everyone to be healthy, results in an accuracy of 99.9%.

$$accuracy = \frac{TP + TN}{TP + TN + FP + FN} \tag{2.27}$$

For this reason, the concepts of recall, precision and F1 score are introduced. Recall describes the ability of a classifier to correctly predict all positive instances (Eq. 2.28), while precision describes the amount of correct predictions among those instances that have been predicted as 'positive' (Eq. 2.29). As both measures are not reliable in itself, a combination of both is required. Therefore, the F1 score is a frequently used metric (Eq. 2.30).

$$recall = \frac{TP}{TP + FN} \tag{2.28}$$

$$precision = \frac{TP}{TP + FP} \tag{2.29}$$

$$F1 = 2 \cdot \frac{recall \cdot precision}{recall + precision} \tag{2.30}$$

The metrics mentioned above are only useful for binary classification, however. In order to translate these metrics to the multiclass problem, overall accuracy (OA) and the macro F1 score are introduced. In a multiclass classification, OA is defined as the total number of TP's divided by the total number of instances. The macro F1 score, on the other hand, takes the average over the individual F1 scores of all classes.

2.7.2. Spatial analysis

In order to determine the required spatial resolution for an optical nighttime satellite sensor, the focus is on finding the minimum spatial resolution that is required to detect individual lamps. Since currently available nighttime imagery do not possess sufficient spatial resolutions for single lamps to be differentiated, lamp detection algorithms are not yet available at the moment. For this reason, a standard keypoint detector is used, i.e. the scale-invariant feature transform (SIFT) algorithm [55], slightly modified to make it better suitable for lamp detection. Whereas SIFT is often applied both as a keypoint detector as well as a keypoint descriptor, here only the detection is of importance. Below follows a short description of the standard SIFT algorithm, together with an explanation of the adjustments.

The SIFT detector consists of two major steps, i.e. scale-space extrema detection and keypoint localisation optimisation. In the first step, an image pyramid is constructed from exposing the image to a series of Gaussian filters with different σ values:

$$L(x, y, \sigma) = G(x, y, \sigma) * I(x, y) \tag{2.31}$$

$$G(x, y, \sigma) = \frac{1}{2\pi\sigma^2} e^{-(x^2+y^2)/2\sigma^2}, \tag{2.32}$$

where $I(x, y)$ denotes the image intensity at position (x,y), $G(x, y, \sigma)$ is the Gaussian filter with scale σ, and $L(x, y, \sigma)$ is the so-called space-scale function. As discussed by Lowe et al. [55], it is then advised to compute the Difference of Gaussians (DoG) $D(x, y, \sigma)$ between subsequent space-scale images in order to detect stable keypoints:

$$D(x, y, \sigma) = L(x, y, k\sigma) - L(x, y, \sigma), \tag{2.33}$$

where k is the step size between two subsequent scales σ, usually set as the square root of two. It has to be noted that such a scale-space pyramid is created for different so-called octaves, with the image being resized to half its size for each octave. In order to detect suitable keypoints, each point in scale-space is then compared to its 3-by-3-by-3 neighbourhood. In other words, it is compared to its eight neighbours within the same DoG level, as well as to its nine neighbours in both the previous and the next DoG level. At this point, the first adjustment is made, i.e. instead of searching for extrema within the neighbourhood, only minima need to be found. The reason for this is that lamps appear bright in images and dark blobs, corresponding to DoG maxima, therefore, do not need to be detected.

Additionally, those minima with limited intensity and those localised along an edge are discarded. For more details, readers are referred to Lowe [55].

The second step of the process, a sub-pixel optimisation of the location of those points, is based on a Taylor expansion of the scale-space function $D(x, y, \sigma)$:

$$D(\mathbf{x}) = D + \frac{\partial D^T}{\partial \mathbf{x}}\mathbf{x} + \frac{1}{2}\mathbf{x}^T \frac{\partial^2 D}{\partial \mathbf{x}^2}\mathbf{x}, \tag{2.34}$$

where D and its derivatives are evaluated at the minima, and $\mathbf{x}$ is the offset from this point, i.e. $\mathbf{x} = (\Delta x, \Delta y, \Delta\sigma)^T$. The optimised location $\hat{\mathbf{x}}$ can then be found by taking the derivative of $D(\mathbf{x})$ with respect to $\mathbf{x}$, and setting the result to zero. Therefore, the offset equals

$$\hat{\mathbf{x}} = -\frac{\partial^2 D}{\partial \mathbf{x}^2}^{-1} \frac{\partial D}{\partial \mathbf{x}}. \tag{2.35}$$

A crucial factor for SIFT to work for lamp detection will be adjusting the lower and upper bounds for the scale parameter σ. In other words, σ should not be too low, in order to avoid detecting small blobs that are not large enough to be the result of lamp radiation. The upper bound, on the other hand, avoids that two different lamps are merged together and are, therefore, detected as one single lamp.

3

Data sources

3.1. Radiation sources

3.1.1. Artificial lights

Spectrum

As has been discussed previously in Section 2.2.1, artificial lights emit light in varying intensities for different wavelengths. For the representation of their spectra, two different datasets have been used, with a focus on outdoor street lighting. The first source is the spectral library collected by Elvidge et al. [34]. The authors measured a variety of light sources in a laboratory environment using a spectrometer, with the measured spectra ranging from 350 nm to 2500 nm at a spectral resolution of 1 nm. The second dataset consists of empirical in-situ data has been collected by Tapia et al. [56] for various lamps in the city of Madrid, Spain. These recorded spectra range from 300 nm to 900 nm at steps of 1 nm. Figure 3.1 gives an indication of the variance of the utilised lamp spectra for different lamp types. While some of these types, e.g. low-pressure sodium lamps, exhibit relatively small variances in their spectra, other types, e.g. LED lamps, vary significantly more. It is important to note here that small errors might have occurred during the recording of the spectra, especially for the in-situ dataset. However, due to the multitude of available spectra, such errors should have only little effect on the outcome.

Intensity

In order to determine the intensity of certain lamps for different wavelengths, the DIN EN 13201 standard for road lighting [57] is used as a reference. Because it is more relevant to know how much reflected light can be seen by the human eye than to know the radiant power of a particular lamp, standard values for average road luminance and illuminance are given instead (Table 3.1). Note that these values are minimum values only and real-world values should never fall below this minimum. Therefore, slightly higher values can be expected in reality. Likewise,

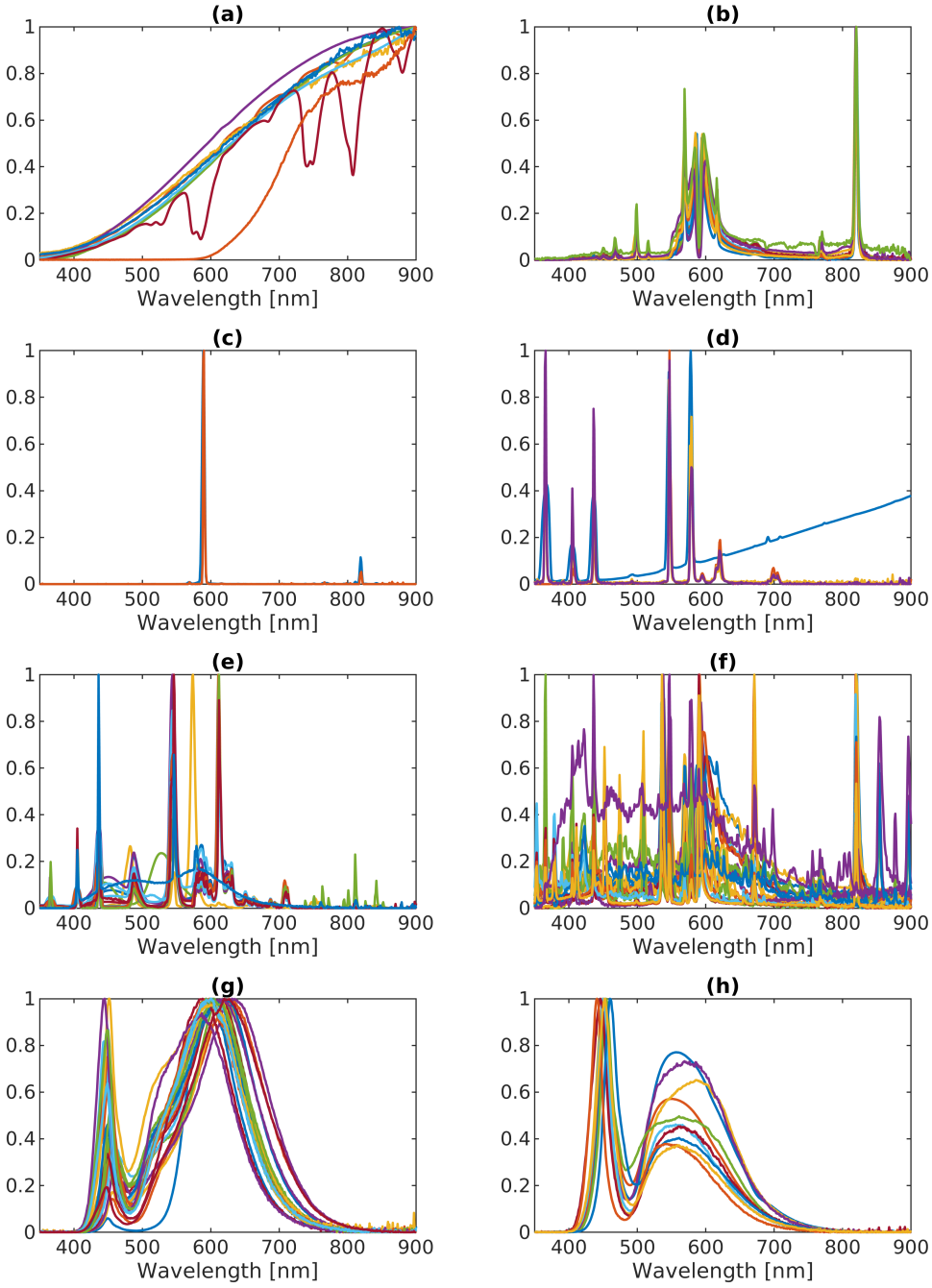

Figure 3.1: Variation in emission spectra for different lamp types with (a) incandescent lamps; (b) high-pressure sodium lamps; (c) low-pressure sodium lamps; (d) mercury vapour lamps; (e) metal halide lamps; (f) fluorescent lamps; (g) warm LED lamps (CCT ≤ 4000 K); and (h) cool LED (CCT > 4000 K). Note that the y-axis represents relative irradiance values.

the lower limit can be expected to be slightly lower, as is the case for some pedestrian or cycle areas. From these luminance recommendations, by applying the inverse of Eq. 2.1, radiances can be deduced. These radiance values should then equal the integral over all spectral radiances. Since relative spectral radiances can be computed from combining lamp spectra with surface reflectances, deducing a lamp's spectral radiance is relatively straightforward.

Road class	Minimum luminance [cd m^{-2}]	Minimum illuminance [lm m^{-2}]
ME1	2.0	30
ME2	1.5	20
ME3	1.0	15
ME4	0.75	10
ME5	0.5	7.5
ME6	0.3	4.5

Table 3.1: DIN EN 13201 standard luminance and illuminance values for road lighting [57]. ME road classes represent roads with medium to high traffic speeds, with the specific class depending on traffic volume and the amount of intersections, among others [57].

Intensity distribution

The light emitted by artificial lighting sources does not only vary with wavelength, but also depends on the direction in which the light is emitted. Therefore, luminous intensity distribution patterns are required, which show the intensity of emitted light for different directions. Usually, luminous intensity is represented by cross sections through the intensity distribution. To define these cross sections, the so-called A, B and C plane systems are used, with the C system being the most frequently implemented. For C planes, the common rotation axis is perpendicular to the axis of the luminaire. Every plane can then be defined by its angle with respect to the luminaire axis, with C_0 perpendicular to the luminaire axis and C_{90} parallel to it. Within such a plane, gamma angles represent the angle between the vertical rotation axis and the direction of light. Intensity distributions of specific lamps can be found relatively easy on the website of their respective manufacturers and usually come in two different file exchange formats, i.e. the Illuminating Engineering Society of North America (IESNA) lm-63-02 (.ies) and the European Lumen Data (EULUMDAT) (.ldt) formats. A typical example of a luminous intensity distribution for a streetlight can be seen in Figure 3.2. During this thesis, different intensity distributions from Leotek's GreenCobra LED series [58], one of the industry's standards, are used.

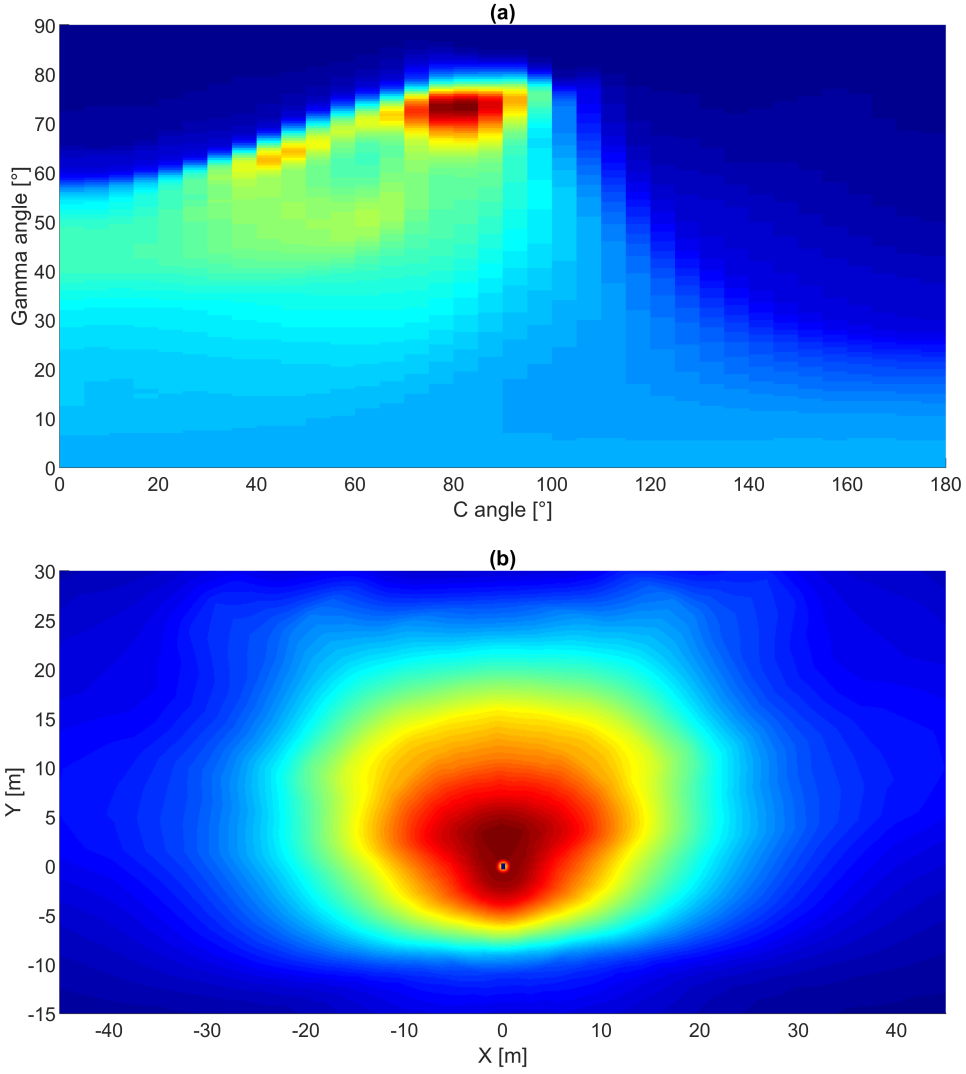

Figure 3.2: Example of a luminous intensity distribution, for a Leotek GCL2-60G-MV-WW-2R-XX-750 lamp, with (a) intensity distribution; and (b) resulting top-view radiance image. Red represents high relative illuminance and radiance values, while dark blue corresponds to low values. Note that C angles only range from 0 to 180 degrees, because of the symmetrical nature of the intensity distribution.

3.1.2. Moon

For lunar irradiance values, the empirical model by Kieffer and Stone [59] has been applied. Based on images of the Moon at 32 wavelengths between 350 nm and 2450 nm, the authors fitted the observations to

$$\ln A_\lambda = \sum_{i=0}^{3} a_{i\lambda} g^i + \sum_{j=1}^{3} b_{j\lambda} \Phi^{2j-1} + c_1\theta + c_2\phi + c_3\Phi\theta + c_4\Phi\phi + d_{1\lambda} e^{-g/p_1} + d_{2\lambda} e^{-g/p_2} + d_{3\lambda} \cos\left[(g - p_3)/p_4\right], \tag{3.1}$$

where A_λ denotes the disk-equivalent reflectance by the Moon for a particular wavelength λ, g is the absolute phase angle of the Moon, θ and ϕ are the selenographic latitude and longitude of the observer, respectively, Φ is the selenographic longitude of the Sun, and $a_{i\lambda}$, $b_{j\lambda}$, c_1, c_2, c_3, c_4, $d_{1\lambda}$, $d_{2\lambda}$, $d_{3\lambda}$, p_1, p_2, p_3 and p_4 are the coefficients as a result of the fitting, which can be found in [59] for the different wavelengths. In order to achieve a spectral resolution of 1 nm, the individual coefficients underwent a piecewise cubic interpolation. The conversion to irradiance values can then be completed by computing

$$E_{M,\lambda} = \frac{A_\lambda \Omega_M E_{S,\lambda}}{\pi}, \tag{3.2}$$

where $E_{M,\lambda}$ represents the irradiance at a certain wavelength λ, Ω_M is the solid angle of the Moon, i.e. $6.4177 \cdot 10^{-5}$ sr, and $E_{S,\lambda}$ is the solar spectral irradiance at wavelength λ. Note that the Spacecraft Planet Instrument Camera matrix Events (SPICE) tool was used for the computation of the Moon's position, lunar phase angle and selenographic coordinates. The solar spectral irradiance values come from the 1985 Wehrli standard extraterrestrial solar irradiance spectrum [60]. Figure 3.3 shows that irradiances under new moon conditions are relatively small (i.e. a maximum value of $2.7 \cdot 10^{-9}$ W m^{-2} nm^{-1} at 638 nm). Even at quarter moon, the influence of moonlight is limited in comparison to the full moon situation. Finally, spectral radiance values can be computed from spectral irradiances by dividing by π for perfect Lambertian reflectors.

3.1.3. Other

Fire is one of the other nocturnal VNIR radiation sources considered, with intensities large enough to be detected by a sensor with large spatial resolutions. Fire spectra for particular temperatures are based on Planck's law for blackbodies as given by Eq. 2.2. Note that these theoretical spectra (Fig. 3.4) differ slightly from empirical data, especially in the thermal infrared part of the spectrum, e.g. because of the production of carbon dioxide and water vapour that accompanies combustion of flames. For VNIR spectral radiances, however, Planck's law serves as a good approximation [61]. As is typical for fires, emissions in the visible part of the spectrum are almost negligible with respect to infrared emissions.

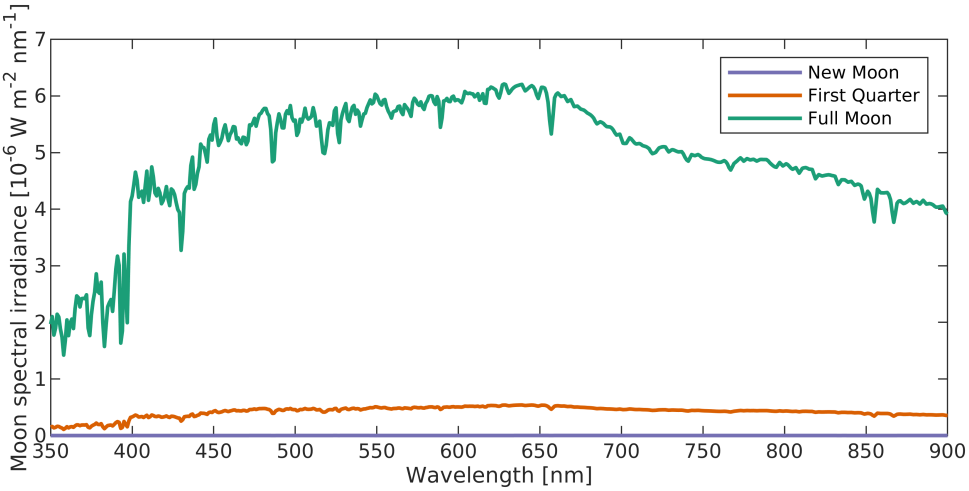

Figure 3.3: Moon spectral irradiance values for lunation 1194 in Munich, Germany. New moon on 2 July 2019, 19:16 UTC, first quarter on 9 July 2019, 10:54 UTC, and full moon on 16 July 2019, 21:38 UTC.

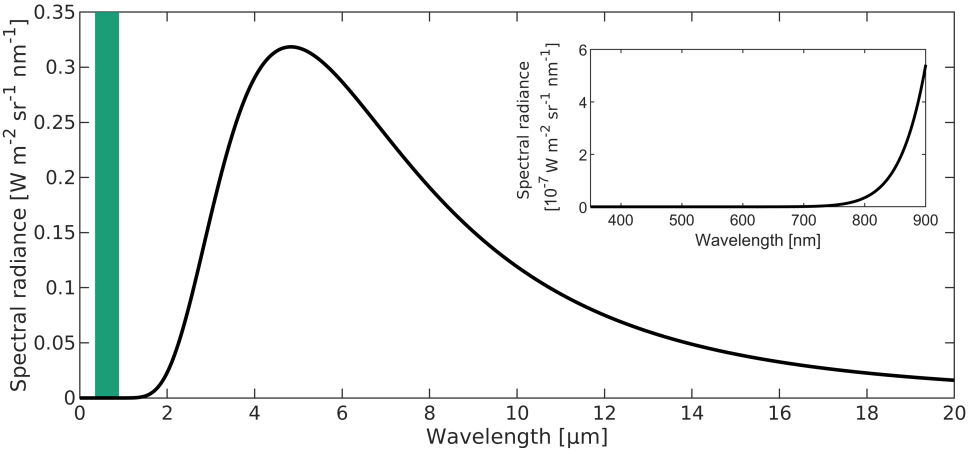

Figure 3.4: Theoretical blackbody radiance spectrum for a blackbody with a temperature of 600 K. The VNIR part of the spectrum is indicated in green and additionally displayed in the inset figure.

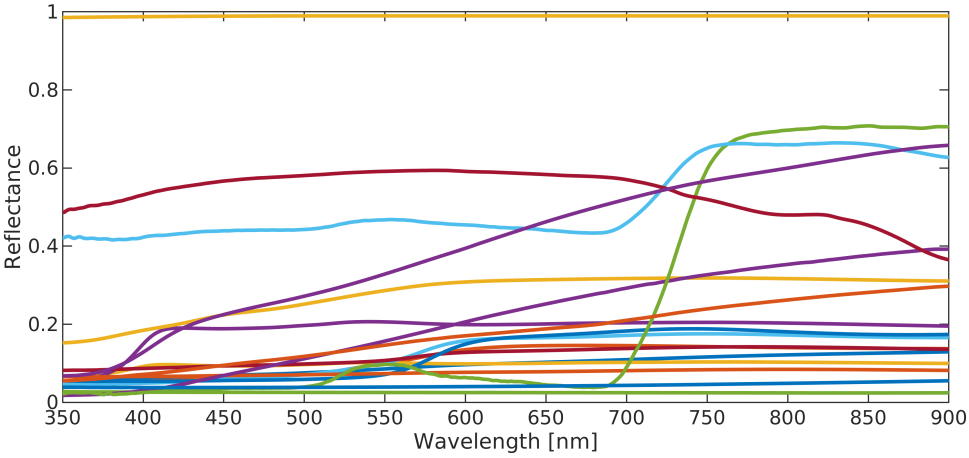

Figure 3.5: Variation in selected surface reflectance spectra.

3.2. Propagation of electromagnetic radiation

3.2.1. Surface interaction

Surface reflectance data is required to generate a spectral library of reflected lamp emissions under the influence of different atmospheric conditions. For this reason, the United States Geological Survey (USGS) spectral library version 7 is used [62] as a source for surface reflectances. Based on laboratory, field and airborne data, the authors measured spectra for various minerals, soils, coatings, liquids, organics, artificial materials and vegetation. The spectra range from 200 nm to 200 µm and have been linearly interpolated to a spectral sampling interval of 1 nm for use in this thesis. For a full description of the data and the applied spectrometers, readers are referred to Kokaly et al. [62]. Selected materials include road asphalt, paved brick, road concrete, grass, snow, sand, wood, asphalt roof shingle and a Spectralon with near-constant reflectance of 99%. Variation in the VNIR part of the spectrum for different selected surfaces is shown in Figure 3.5.

3.2.2. Atmosphere interaction

Radiative transfer is the physical process to transform BOA radiances into TOA radiances, by which radiation interacts with the atmospheric constituents. In this thesis, to quantify atmospheric impacts, libRadtran [63] is the software package of choice. In order to compute transmittance values, a number of input variables are required. These variables include wavelength range, aerosol type, aerosol visibility, aerosol season and atmospheric profiles, to mention a few. For a more detailed understanding of the physics behind radiative transfer and more information on the use of libRadtran, readers are referred to the user guide [64]. With a focus on urban environments, urban aerosols are the preferred aerosol type, with aerosol visibility strongly determining transmittance values. The selected atmospheric profiles are taken from libRadtran's standard library, with standard mid-latitude summer,

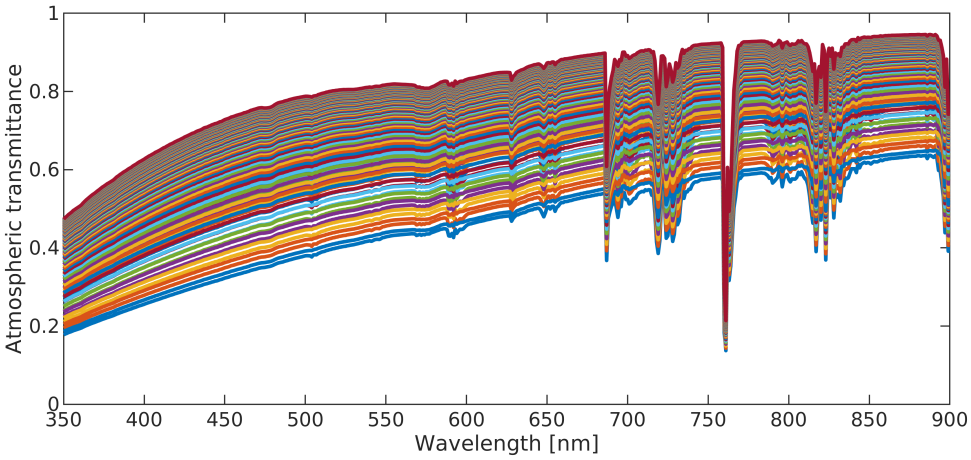

Figure 3.6: Variation in selected atmospheric transmittance spectra.

mid-latitude winter, subarctic summer, subarctic winter and tropical atmospheric profiles among the options. Figure 3.6 gives an idea of the variation within the selected atmospheric transmittance spectra, with a range of 30% to 40% between the highest and lowest atmospheric transmittance. Without further assumptions, this also gives an indicator of the possible error range for atmospheric transmittance estimation, which is the largest error source in the estimation of a lamp's radiant power [40].

4

Sensor simulation

4.1. Spectral sampling

Central to the spectral sampling is the generation of a particular spectral band's sensor signal in a single pixel environment, i.e. without any spatial information. In order to do so, a framework is set up, which consists of two fundamental parts, that is (1) a spectrum modelling block; and (2) a sensor modelling block (Fig. 4.1). Whereas the former is used to determine TOA spectral radiances from input variables such as lamp spectrum, surface reflectance, atmosphere type and luminance values, the latter is a basic sensor model and transforms TOA spectral radiances into a sensor signal for a particular band. Further details of the framework are discussed below. The main goal of this section is to determine those sensor parameters that are optimal for the design of a dedicated nighttime VNIR mission. At first, a spectral library is generated for typical TOA spectral radiances, which serves as a reference for the KNN classification. Afterwards, spectral bands are optimised in order to estimate the aforementioned spectral indices (see Section 2.3), as well as to classify single-pixel spectra according to radiation source type. These bands are selected in an order set by the relative importance of the respective indices, i.e. (1) LER; (2) spectral G index; (3) radiation source type; and (4) CCT. It is important to note here that the radiation source type can serve as a proxy variable for other indices, e.g. radiant power, as well as offer an opportunity for improved estimation of aforementioned indices, e.g. luminous efficacy.

4.1.1. Generation of spectral library

In order to generate a spectral library that contains typical nighttime TOA radiance values, a selection of typical radiation sources, surfaces and atmospheric conditions is required. The fourth input variable, which is part of the spectrum modelling block (Fig. 4.1 top), i.e. luminance (or lamp intensity), can be chosen as a constant value since the spectral library focuses only on relative TOA radiance values. The reason for this is that the KNN classification requires normalised values, as distances in fea-

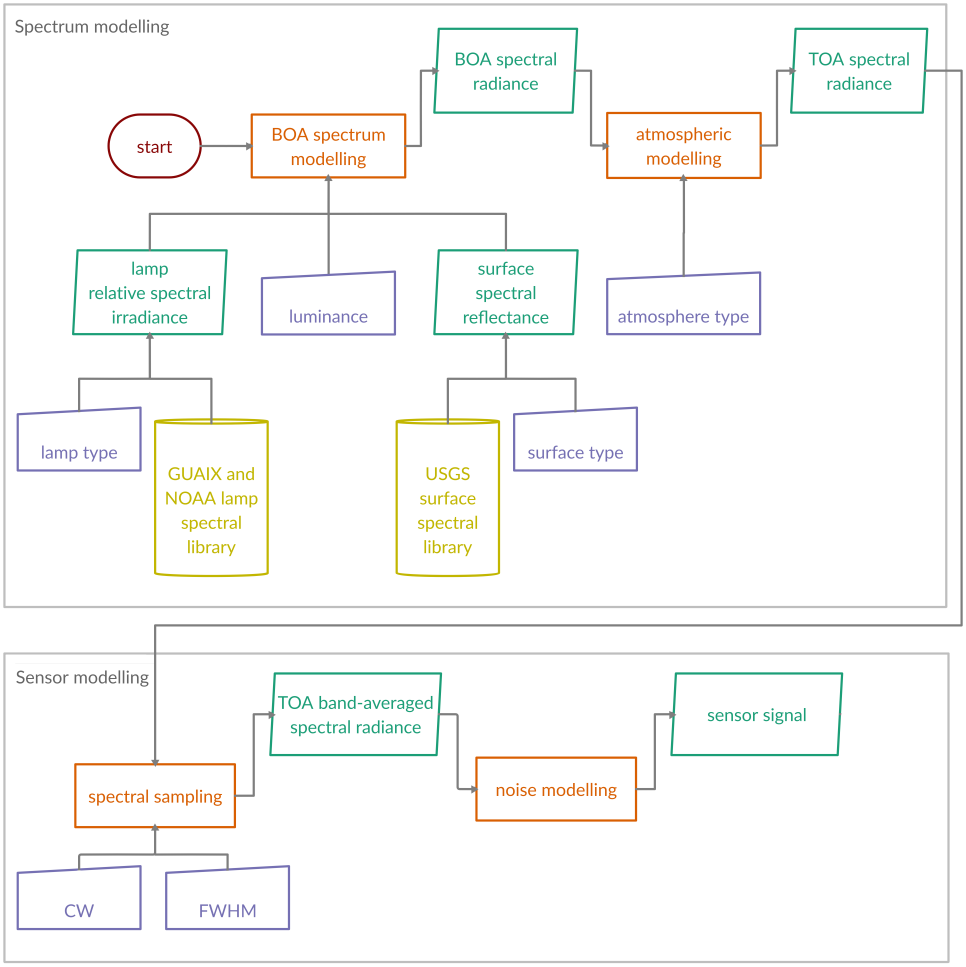

Figure 4.1: Workflow framework for the simulation of a spectral band's sensor signal.

ture space would otherwise depend almost completely on a lamp's intensity or the corresponding luminance, thereby hampering radiation source type classification.

Bottom-of-atmosphere spectrum modelling

As the focus of this thesis is on urban areas, it is self-evident that the main group of radiation sources is that of artificial lights. However, most of these artificial lights do not occur solely in urban areas, but also in rural areas. In these areas, another source of VNIR radiation is that of combustion or fire. Therefore, it is useful to include combustion in the spectral library, even though this type of radiation does not, strictly speaking, occur in urban areas. Introducing combustion enables the distinction between radiation as a result of combustion and that of artificial lights. A full radiation source typology can be found in Table 4.1 and is for the most part based on the work of Elvidge et al. [34] and currently available lamp types (see Section 2.2.1). A distinction is made here between level 1 and level 2 types. Level 1 types include the main groups of radiation sources at night, i.e. (1) combustion or fire; (2) incandescent lamps; (3) gas-discharge lamps; and (4) LED lamps. Note that moonlight is not considered as a radiation class here, since its radiance values are relatively small in comparison. Because of a large variance within its class, both the gas-discharge class and the LED class are further subdivided in the second level. The former comprises the high-pressure sodium, low-pressure sodium, mercury vapour, fluorescent and metal halide classes, while the latter encompasses both the warm LED and cool LED classes. For the distinction of LED classes, a threshold is fixed at a CCT of 4000 K, roughly corresponding to neutral white light.

Fire BOA spectral radiances can be directly modelled from their temperature using Planck's equation (Eq. 2.2), which serves as a good approximation for real-world fire spectra. Surface reflectances do not need to be taken into account here. Typical fire temperatures can range from 400 K for simmering fires to 1200 K for flaming hot fires [65, 66]. For the spectral library, four entries are created with temperatures of 500 K, 700 K, 900 K and 1100 K, respectively, in order to cover a sufficient range without risking the chance of overfitting later on during classification.

Generating BOA spectral radiances as a result of artificial lighting is a slightly more extensive task. To begin with, lamp spectra are taken from both the GUAIX [56] and NOAA [34] spectral libraries. Spectra are then interpolated to the 350 nm to 900 nm range in steps of 1 nm, as it is the range common to both libraries and comprises the VNIR wavelengths of interest for this thesis. Note that absolute values are of no importance here, as has been explained above. For each of the second level lamp types, two representative spectra are selected. At this point, spectral indices such as LER, spectral G index and CCT are calculated according to the equations and algorithms presented in Section 2.3. Subsequently, the lamp spectra are combined with eight typical surface reflectance spectra from USGS's spectral library version 7 [62]. These include asphalt, concrete, grass, snow, sand and a spectralon with constant reflectance. The resulting combined spectra describe relative BOA spectral radiances. These are then adjusted so that luminance values are constant across all lamp type and surface type combinations. In this case, a luminance of 1 cd m^{-2} was chosen. However, the value in itself is of no importance here.

Level 1	Level 2
Combustion	Combustion
Incandescent	Incandescent
Gas-discharge	High-pressure sodium
	Low-pressure sodium
	Mercury vapour
	Fluorescent
	Metal halide
LED	Warm LED (≤ 4000K)
	Cool LED (> 4000K)

Table 4.1: Radiation source typology for different levels.

Atmospheric modelling

In order to derive TOA spectral radiances from BOA spectral radiances, it is required to estimate atmospheric transmittance values. Here, this is done using the libRadtran software [63] across the 350 nm to 900 nm wavelength range. Since the focus of a dedicated nighttime mission is on cloud-free conditions, only such atmospheres are included in the library. Furthermore, whereas a standard atmosphere is usually defined for rural areas, urban aerosols are preferred in this case. For the reference library, ten transmission spectra are computed, i.e. mid-latitude summer atmosphere, mid-latitude winter atmosphere, subarctic summer atmosphere, subarctic winter atmosphere and tropical atmosphere with 20 km or 75 km visibility. Combining these with BOA radiance spectra, this results in 1320 library entries in total.

4.1.2. Generation of test data

Spectrum modelling

With the aim of adjusting spectral bands as to optimise radiation source classification, possessing a spectral library is not sufficient. Test data need to be simulated additionally to examine the estimation and classification performances of different band combinations. The simulation of these test data is, in essence, similar to that of the spectral library, only with more options available to combine from. That way, the robustness of certain spectral bands to slightly differing data is ensured. Moreover, the number of test data is kept constant for different second level radiation source types, i.e. 500 for each class. This is done to keep classification performance metrics comparable for different classes. For fire spectra, temperat-

ures are uniformly randomly chosen between 400 K and 1200 K and used as input to Planck's equation. For each lamp class, 500 spectra are randomly picked from all available lamp spectra. These are then combined with a randomly chosen surface reflectance spectrum, picked from 18 frequently occurring options. For each of the combined relative BOA radiance spectra, a luminance value is chosen at random. The utilised luminance extrema, i.e. 0.3 and 4.0 cd m^{-2}, are based on the European DIN EN 13201-2 standard for road lighting on performance requirements [57] and on measured data [67]. It has to be noted that luminance values can be larger under wet conditions because of specular reflection. However, since wet surfaces generally go hand in hand with cloudy conditions, which block most light from reaching the satellite sensor, higher luminance values do not need to be considered here. Finally, atmospheric transmittance spectra are selected, with visibility randomly chosen between 10 km and 100 km for the five atmospheric profiles mentioned above in Section 4.1.1. This results in a total of 4500 combined TOA radiance spectra.

Sensor modelling

For any given spectral band, the TOA band-averaged spectral radiance can be computed from the TOA radiance spectra using Eq. 2.14. After this step, noise needs to be added to the signal in order to end up with a realistic sensor signal. As a reference for the noise model, the recommendation of Elvidge et al. [17] on SNR is adopted, i.e. an SNR_{ref} of 10 at a band-averaged spectral radiance $L_{\lambda,ref}$ of 2.5 · 10^{-7} W m^{-2} sr^{-1} nm^{-1} for a spectral band with $\lambda_{C,ref}$ = 560 nm and $\Delta\lambda_{ref}$ = 100 nm. Based on Eq. 2.19, with the assumption of all other variables remaining identical, this results in a practical equation for the computation of the standard deviation of noise-equivalent radiance (NER) $\sigma_{NER,band}$ (Eq. 4.1). This standard deviation allows for a noise value to be taken from a Poisson distribution, which can be added to the TOA band-averaged spectral radiance to form the sensor signal. Note that the conversion to a digital number is not advised at this point, due to the fact that some sensor-specific qualities need to be known before detection limits and saturation values can be determined.

$$\sigma_{NER,band} = \frac{L_{\lambda,ref}}{SNR_{ref}} \cdot \sqrt{\frac{L_{\lambda,band}}{L_{\lambda,ref}} \cdot \frac{\Delta\lambda_{ref}}{\Delta\lambda_{band}} \cdot \frac{\lambda_{C,ref}}{\lambda_{C,band}}} \tag{4.1}$$

4.1.3. Band selection: luminous efficacy of radiation

A choice of two bands is required for the estimation of luminous efficacy of radiance (LER). Indeed, when looking at its equation (Eq. 2.3), it is obvious that one band should be used to estimate the radiance emitted across the full spectrum (i.e. the denominator of the equation), while a second band should estimate the amount of radiation which is visible to the human eye (i.e. the numerator). The former will also be used as the sensor's panchromatic band and, additionally, functions as a denominator for the normalisation of other bands' sensor values later on during classification. As the latter band estimates the amount of visible light, its slit function should closely resemble the photopic spectral luminous efficiency curve $V(\lambda)$, used

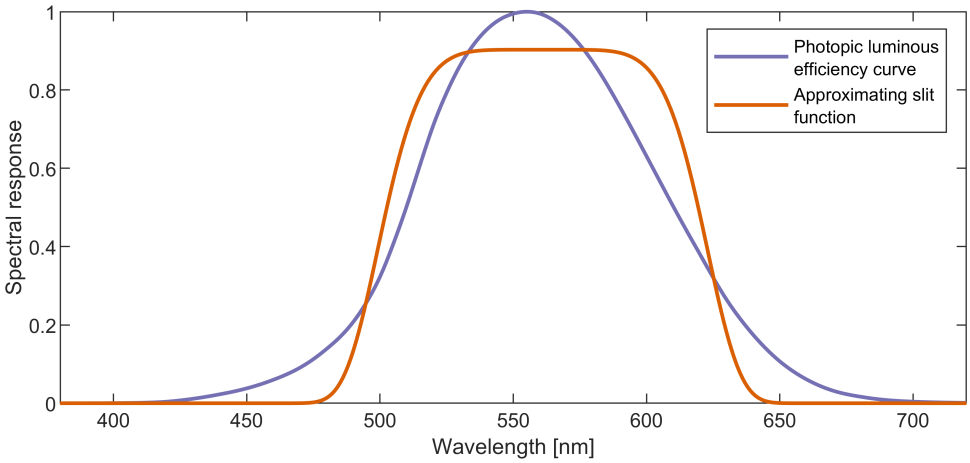

Figure 4.2: Approximation of photopic spectral luminous efficiency function by slit function.

for the computation of the amount of visible light. However, the form of a slit function does differ from the form of $V(\lambda)$. Theoretically, the optimal spectral band to resemble $V(\lambda)$ is reached for a CW of 561 nm and a FWHM of 121 nm (Fig. 4.2). Note that the CW differs slightly from the wavelength at which $V(\lambda)$ reaches its maximum, i.e. 555 nm. This can be ascribed to the asymmetrical form of its curve, with the function having a slightly positive skew. It is expected that this small shift to higher wavelengths will be less significant in practice, as most lamps have almost no emissions around the right base of the function, i.e. around 650 nm.

In order to select the optimal bands for LER estimation, uniformly distributed sampling is used for the two bands' CW and FWHM. For the panchromatic band (B0), FWHM ranges between 300 nm and 550 nm, while the CW ranges between 500 nm and 750 nm. The band used for approximating $V(\lambda)$ (B1), on the other hand, can have FWHM values between 80 nm and 150 nm and a CW between 500 nm and 600 nm. Note that the step size for FWHM is 5 nm for both bands, because of the practical difficulty of achieving sensor filters at nanometre-level accuracy, while CW values change in steps of 1 nm. Estimating LER is eventually achieved by dividing the photopic band values by the panchromatic band values for both the test data and the data within the spectral library. These ratios, however, do not yet represent true LER values and need to be adjusted by applying a multiplication factor a (Eq. 4.2). The estimation of this factor is based on the ratios and true LER values within the spectral library. Its value can be approximated by using Eq. 4.3, although a least-squares estimation based on the spectral library is preferred. Applying the estimated multiplication factor with the band value ratios for the test data eventually results in the estimated LER_{est}. The performance of a given band combination of B0 and B1 is evaluated through the mean absolute error (MAE).

$$LER_{est} = a \cdot \frac{L_{\lambda,B1}}{L_{\lambda,B0}} \tag{4.2}$$

$$a \approx K_{max} \cdot \frac{\Delta\lambda_{B0}}{\Delta\lambda_{B1}} \tag{4.3}$$

An optimum for LER estimation is reached for the following combination of bands: (1) $\lambda_{C,B0}$ = 619 nm and $\Delta\lambda_{B0}$ = 490 nm for the panchromatic band; and (2) $\lambda_{C,B1}$ = 556 nm and $\Delta\lambda_{B1}$ = 125 nm for the 'photopic' band. Note that, as expected, the values for B1 deviate slightly from those reached from approximating the photopic luminous efficiency function directly. The reason for this is the distribution of radiances across the different wavelengths for lamps. For the two bands mentioned above, an MAE for LER of 13 lm W^{-1} is reached. For comparison, the mean LER for the test data equals 307 lm W^{-1}, with a standard deviation of 117 lm W^{-1}. It is important to note that these ground-truth LER values are slightly higher than they will be in reality, since the they are only based on the 350 nm to 900 nm range, with data outside this range missing for some of the spectra. The estimation of the multiplication factor a based on Eq. 4.3 results in a value of 174, while the least-squares estimation yields 151. Applying a similar analysis to the bands recommended by Elvidge et al. ($\lambda_{C,B1}$ = 560 nm and $\Delta\lambda_{B1}$ = 80 nm) [34] results in an MAE of 46 lm W^{-1}, indicating that the proposed bands offer a significant improvement for the estimation of the efficiency of artificial lighting.

4.1.4. Band selection: spectral G index

The estimation of the spectral G index, with a focus on the amount of blue light, again requires two spectral bands. However, this time, the enumerator (Eq. 2.4) does not need an additional band, since it can be approximated by band B1 as optimised above for the estimation of LER. The denominator, on the other hand, comprises the sum of emissions within the 380 nm to 500 nm range of the EM spectrum, and therefore needs an additional band B2. Taking the sum of spectral radiances between 380 nm and 500 nm equals applying a rectangular filter with a CW of 440 nm and an FWHM of 120 nm. This means that the optimal band for a super-Gaussian slit function should not, in practice, differ much from these values. The spectral G index for the test data can be estimated by applying

$$G_{est} = 2.5 \cdot \log_{10}\left(a \cdot \frac{L_{\lambda,B1}}{L_{\lambda,B2}}\right), \tag{4.4}$$

where the multiplication factor a is again estimated from the spectral library. Note that the logarithmic form is at first ignored, in order to more accurately estimate the multiplication factor. Both the CW and the FWHM are again chosen randomly by uniformly distributed sampling, with the former ranging between 420 nm and 460 nm, while the latter can have values between 100 nm and 140 nm. As expected, the optimal band closely resembles the rectangular filter mentioned above, with $\lambda_{C,B2}$ = 443 nm and $\Delta\lambda_{B2}$ = 120 nm. For a multiplication factor of a = 1.15, an MAE of 0.081 is obtained. By comparing this result to the mean and the standard deviation of the test data, i.e. 1.875 and 1.923 respectively, adding a band in the blue part of the spectrum proofs to be beneficial. The Nightsat proposal by Elvidge et al. [34], occasionally criticised for its lack of a dedicated blue band, only reaches

an MAE of 0.569, significantly larger than the value reached by a combination of bands B1 and B2. With common criteria suggesting $G \geq 1.5$ or $G \geq 2.0$ [37], an error of 0.081 is acceptable in most cases. Note that these accuracy values additionally depend on the sensor's characteristics, i.e. detection limits, saturation values and the number of bits used for radiometric sampling. Hence, the G index error will be slightly larger in reality, but should remain acceptable for a sensible choice of sensor parameters.

4.1.5. Band selection: radiation source classification

In order for the k-nearest neighbour (KNN) classification to function properly, normalised band-averaged spectral radiances are required. These can be achieved by dividing a band's signal by the signal of B0, i.e. the signal of the panchromatic band. Classification is then performed using the so-called one-versus-all KNN method, as is described in Section 2.7. For each radiation source type, this method searches for the best possible combination of bands, including bands B1 and B2 that have been fixed above. Note that the distinction between the warm LED and cool LED classes is based solely on the least-squares estimation of CCT. Additional spectral bands are again picked by uniformly distributed sampling with a CW between 350 nm and 900 nm and an FWHM between 10 nm and 200 nm. Table 4.2 gives an overview of the classification performance metrics for individual radiation source classes, for optimal band selections of zero, one and two additional spectral bands. Note that the optimisation is based on the maximisation of the sum of the mean F1 scores for the first level and second level classes.

One additional band

As a reference, the classification performance of the case where no additional bands were added, i.e. by only making use of bands B0, B1 and B2, reaches F1 scores of 67.8% and 62.0% for the first and second level radiation source types, respectively. With the Nightsat proposal [34] band selection reaching values of 82.9% and 79.1% for the same test data, it is evident that improvement is possible, and required, by including more spectral bands. In the case of one additional band, an optimum is reached for $\lambda_{C,B3}$ = 578 nm and $\Delta\lambda_{B3}$ = 15 nm. Corresponding F1 scores significantly increase to 83.2% for the first level classes and 80.2% for the second level classes. These performance levels closely resemble the results obtained by Nightsat's proposed bands, even though only three multispectral (MS) bands are used in comparison to Nightsat's four.

Figure 4.3, which shows normalised band radiance values for different radiation sources, confirms the result of the optimisation process. Whereas for the combination of spectral bands B1 and B2 data are more or less part of one large cluster (Fig. 4.3a), more differentiation is possible by adding B3 (Fig. 4.3b-c). For example, the largest improvement can be seen for mercury vapour lamps, which can now be clearly differentiated from other radiation types. This is further supported by the F1 score, increasing from 15.6% for two MS bands to 86.1% for three MS bands. Other lamp classes that can be distinguished rather well are low-pressure sodium lamps and high-pressure sodium lamps, with F1 scores of 92.1% and 83.8%. The

Level 1 type	F1 score, 2 MS bands	F1 score, 3 MS bands	F1 score, 4 MS bands
Combustion	0.537	0.741	0.791
Incandescent	0.744	0.785	0.856
Gas-discharge	0.793	0.918	0.955
LED	0.638	0.884	0.941
Level 2 type	**F1 score, 2 MS bands**	**F1 score, 3 MS bands**	**F1 score, 4 MS bands**
Combustion	0.537	0.741	0.791
Incandescent	0.744	0.785	0.856
High-pressure sodium	0.697	0.838	0.981
Low-pressure sodium	0.960	0.921	0.961
Mercury vapour	0.156	0.861	0.865
Fluorescent	0.670	0.706	0.767
Metal halide	0.687	0.807	0.884
Warm LED	0.554	0.729	0.926
Cool LED	0.495	0.772	0.956
Mean F1, level 1	0.678	0.832	0.886
Mean F1, level 2	0.620	0.802	0.899

Table 4.2: F1 scores per lamp type for 2, 3 and 4 multispectral bands.

distinction between level 1 types can be made rather well for gas-discharge and LED lamps, while recognising fire and incandescent lamps remains relatively difficult (Table 4.2). This should not surprise, as both fire and incandescent lamps approximate the spectrum of a blackbody. This means that, especially for the shorter wavelengths and incandescent lamps with a low intensity, there is little to differentiate between the two classes. In other words, adding an additional spectral band in the near-infrared part of the spectrum might help to improve classification results for these two first level classes.

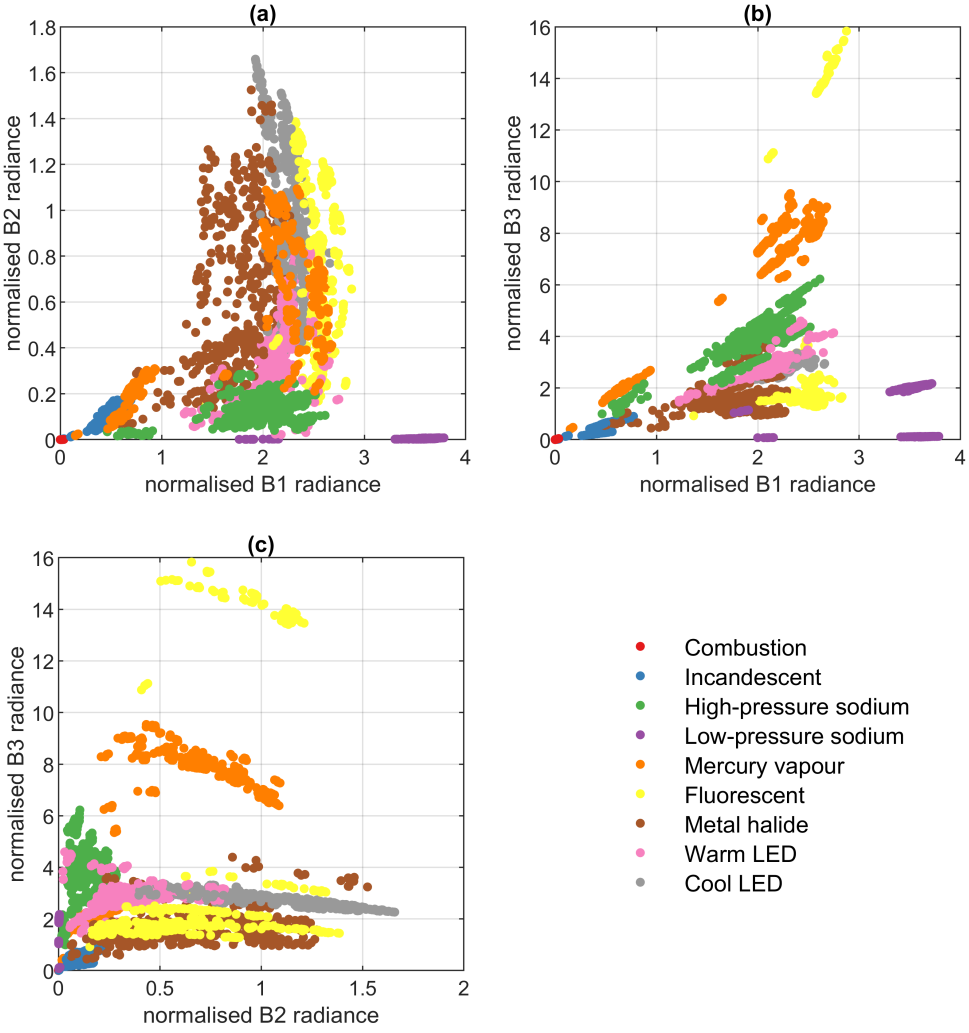

Figure 4.3: Normalised B1, B2 and B3 radiances for different radiation sources, with (1) band B1: $\lambda_{C,B1}$ = 556 nm and $\Delta\lambda_{B1}$ = 125 nm; (2) band B2: $\lambda_{C,B2}$ = 443 nm and $\Delta\lambda_{B2}$ = 120 nm; and (3) band B3: $\lambda_{C,B3}$ = 578 nm and $\Delta\lambda_{B3}$ = 15 nm. Note that the represented radiances do not include a noise factor.

Two additional bands

Although it is expected that the best combination of two additional MS bands probably includes a band identical, or at least similar, to band B3 mentioned above, this is not necessarily the case. The reason for this is that some parts of the spectra might possess high correlations with other parts of the spectra. In other words, joining the two best scoring spectral bands does not necessarily result in a better classification performance if they contain similar, correlated, information. The determination of two additional bands, therefore, needs to start anew from the situation with B0, B1 and B2 fixed, and with slit functions for B3 and B4 being generated randomly.

An optimum is reached for $\lambda_{C,B3}$ = 576 nm, $\Delta\lambda_{B3}$ = 15 nm, $\lambda_{C,B4}$ = 815 nm and $\Delta\lambda_{B4}$ = 35 nm, in the case of two additional MS bands. Band B3 does not, as is expected, differ much from the one found in the case of a single additional band. With respect to that case, this combination of bands B3 and B4 results in a further absolute increase of 5.4% and 9.7% for the level 1 and level 2 F1 scores, respectively (Table 4.2). Especially note the large improvements for the high-pressure sodium class and both of the LED classes. The same can be identified visually from Figure 4.4, e.g. through the two clusters of high-pressure sodium lamps in the B3-B4 combination. Moreover, normalised radiance values exhibit a better spreading for the different radiation source types. In other words, class clusters can be identified more easily. For example, the combination of B1 and B4 shows particularly good clustering capacity for most classes, apart from combustion, LED and fluorescent lamps (Fig. 4.4a). In this four-band combination, only two classes generate F1 scores lower than 80%, i.e. combustion and fluorescent lamps.

A closer look at the level 2 confusion matrix (Table 4.3) reveals the reasons for these low values. For example, fire is sometimes wrongly classified as an incandescent lamp or as a mercury vapour lamp. The confusion with mercury vapour lamps could probably be solved by introducing an extra narrow band around 545 nm, where mercury vapour lamps have one of their emission peaks. However, the relatively low occurrence of both classes in urban areas, and the relatively small improvement of introducing such a band do not justify the costs that accompany the construction of an additional band. Likewise, there is a high correlation between fluorescent and mercury vapour lamps. The reason for this lies in the manufacturing process of a fluorescent lamp. Similarly to mercury vapour lamps, fluorescent lamps make use of mercury gas, resulting in nearly identical emission spectra. Introducing an extra narrow band around 610 nm could possibly solve this issue. However, the question once more remains whether the improvements made justify the costs of introducing a band which sole aim is to distinguish between these two types. An examination of the optimal combination of five MS spectral bands proves that improvements are minimal. For a combination of $\lambda_{C,B3}$ = 575 nm, $\Delta\lambda_{B3}$ = 15 nm, $\lambda_{C,B4}$ = 814 nm, $\Delta\lambda_{B4}$ = 30 nm, $\lambda_{C,B5}$ = 545 nm and $\Delta\lambda_{B5}$ = 10 nm, the level 1 and level 2 F1 scores only show absolute improvements of 0.2% and 1.8%, respectively (Fig. 4.5). Hence, it can be stated that the addition of two MS bands is recommended in order to allow radiation type identification.

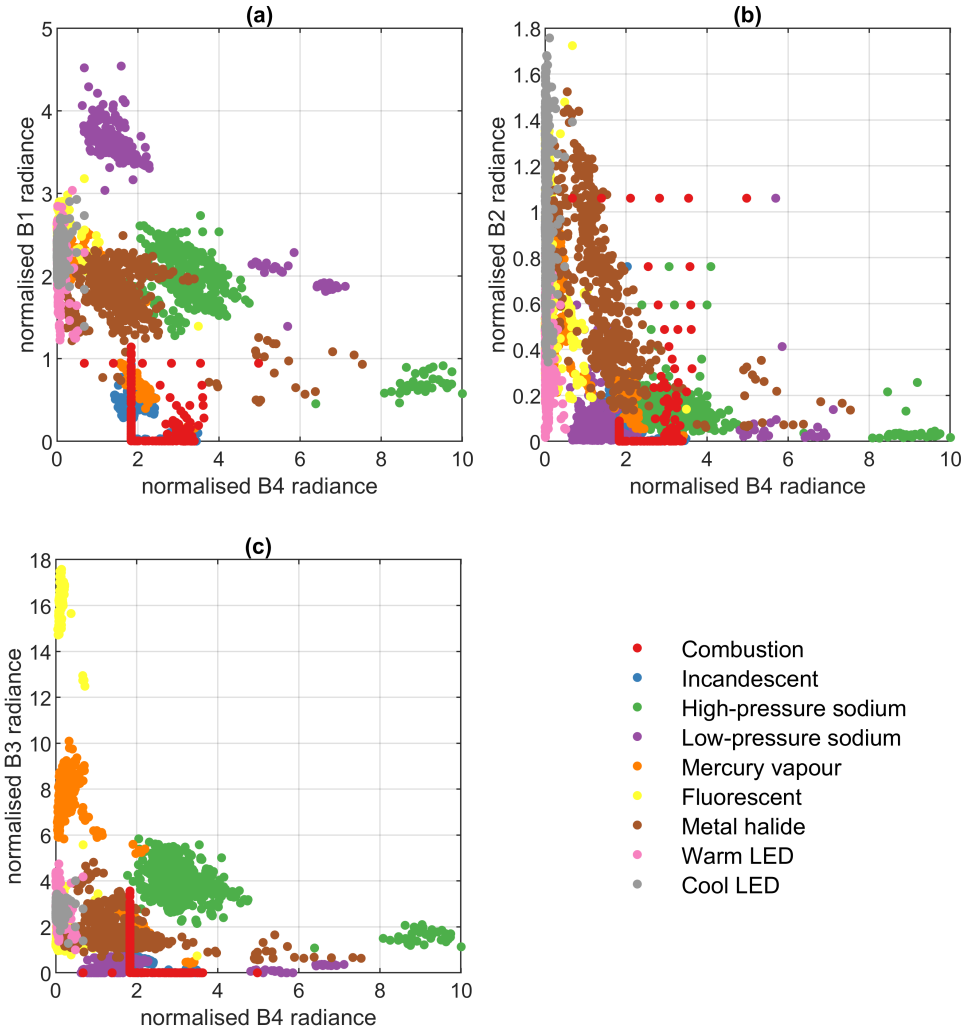

Figure 4.4: Normalised B1, B2, B3 and B4 radiances for different radiation sources, with (1) band B1: $\lambda_{C,B1}$ = 556 nm and $\Delta\lambda_{B1}$ = 125 nm; (2) band B2: $\lambda_{C,B2}$ = 443 nm and $\Delta\lambda_{B2}$ = 120 nm; (3) band B3: $\lambda_{C,B3}$ = 576 nm and $\Delta\lambda_{B3}$ = 15 nm; and (4) band B4: $\lambda_{C,B4}$ = 815 nm and $\Delta\lambda_{B4}$ = 35 nm. Note that the represented radiances do not include a noise factor.

	Class 1	Class 2	Class 3	Class 4	Class 5	Class 6	Class 7	Class 8	Class 9	Total
Class 1	370	43	0	9	2	2	4	1	4	435
Class 2	57	423	0	0	8	0	0	0	0	488
Class 3	0	0	492	0	5	0	6	0	0	503
Class 4	0	0	0	464	0	2	0	0	0	466
Class 5	49	0	0	0	476	75	1	0	0	601
Class 6	0	0	0	0	2	365	19	41	25	452
Class 7	8	0	7	3	1	30	447	6	9	511
Class 8	0	0	0	0	0	24	0	452	0	476
Class 9	0	0	0	0	0	1	4	0	462	467
No class	16	34	1	24	6	1	19	0	0	101
Total	500	500	500	500	500	500	500	500	500	4500

Table 4.3: Level 2 radiation source confusion matrix. Columns and rows represent ground truth classes and predicted classes, respectively. Class 1 = combustion; class 2 = incandescent; class 3 = high-pressure sodium; class 4 = low-pressure sodium; class 5 = mercury vapour; class 6 = fluorescent; class 7 = metal halide; class 8 = warm LED; and class 9 = cool LED. Note that the 'no class' type consists of instances that belong to the 'all' class in all of the one-versus-all KNN classifiers.

4.1.6. Band selection: correlated colour temperature

Although it will most likely lose its value as a lighting metric in the future [37], as it is limited in properly describing a lamp's characteristics, correlated colour temperature (CCT) remains a valuable and frequently mentioned specification as of today. For a proper estimation of CCT, a good distribution of spectral bands along the visible spectrum is required. Looking at the bands that are already fixed for LER and G index estimation, as well as for classification of radiation types, B1 and B2 seem to be good candidates to cover the green and blue part of the spectrum, respectively. The part of the spectrum that is not covered by the existing bands, is located in the

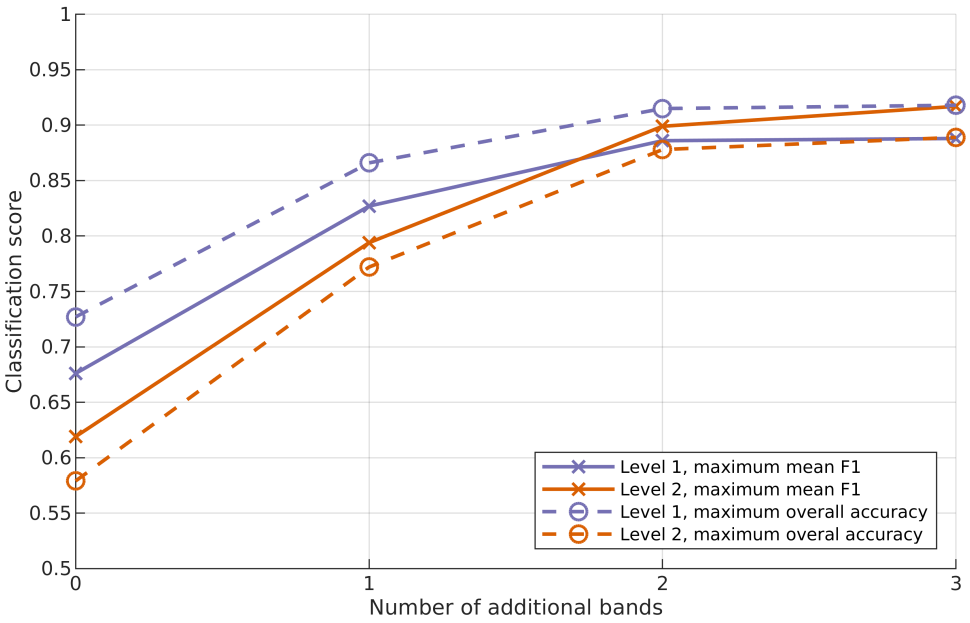

Figure 4.5: Radiation source classification performance for variable number of bands.

red part of the spectrum. It is, therefore, expected that adding a single band in that wavelength range will significantly decrease the estimation error of CCT. Note that CCT is not estimated from the band values directly. Instead the tristimulus values X, Y and Z are estimated through a least-squares adjustment using all band values. From these tristimulus values, CCT was determined using Eq. 2.8-2.11.

As expected, the optimum is reached for a band that covers the red part of the spectrum, i.e. $\lambda_{C,B5}$ = 610 nm and $\Delta\lambda_{B5}$ = 75 nm. By adding this band, the MAE was significantly improved from 994 K to 391 K. An additional advantage of including B5 into the design of a dedicated nighttime VNIR sensor is that it offers the possibility of generating traditional true colour imagery, with B2 corresponding to the blue channel, B1 corresponding to the green channel and B5 corresponding to the red channel.

4.1.7. Performance analysis

The recommended spectral bands are shown in combination with some typical lamp spectra in Figure 4.6. What can be seen immediately is the ability of band B3 to distinguish between different lamp types. Additionally, there is a good spread of the different bands across the VNIR spectrum, except for the wavelengths between 650 nm and 800 nm. This unsurprisingly coincides exactly with that part of the spectrum where lamps emit no light. Due to the nature of nocturnal light sources, the choice of spectral bands differs significantly from the typical daytime optical sensors. Whereas a typical daytime design usually includes the conventional blue, green and red bands, the focus here is different and adjusted to the requirements of

	Nightsat [34]	Sentinel-2	AeroCube	JLI-3B	Proposal (3 MS bands)	Proposal (4 MS bands)	Proposal (5 MS bands)
Band 1 [nm]	450-520	459-525	400-512	430-512	383-503	383-503	383-503
Band 2 [nm]	520-600	542-578	480-590	489-585	493-619	493-619	493-619
Band 3 [nm]	630-690	649-680	560-850	580-720	568-584	568-584	568-584
Band 4 [nm]	700-900	780-886	-	-	-	797-833	797-833
Band 5 [nm]	-	-	-	-	-	-	572-648
MAE (LER)	46.07	114.40	46.58	68.73	12.66	12.66	12.66
MAE (G)	0.569	0.945	0.220	0.370	0.081	0.081	0.081
MAE (CCT)	1207	1134	1264	1442	1884	994	391
Mean F1 score (level 1)	0.829	0.791	0.768	0.750	0.830	0.886	0.886
Mean F1 score (level 2)	0.791	0.806	0.711	0.757	0.798	0.899	0.900
Overall accuracy (level 1)	0.876	0.850	0.779	0.820	0.866	0.915	0.915
Overall accuracy (level 2)	0.727	0.743	0.700	0.704	0.776	0.878	0.880

Table 4.4: Performance comparison with other band combinations. Note that results are based on a panchromatic band with $\lambda_{C,B0}$ = 619 nm and $\Delta\lambda_{B0}$ = 510 nm.

the lighting engineering community and scientific community. This results in some rather atypical bands, e.g. the yellow-orange band around 576 nm.

A performance comparison for the selected bands aith respect to other available band combinations, e.g. the Nightsat proposal, Sentinel-2, AeroCube and JLI-3B satellites, can be found in Table 4.4. As the table reveals, a performance improve-

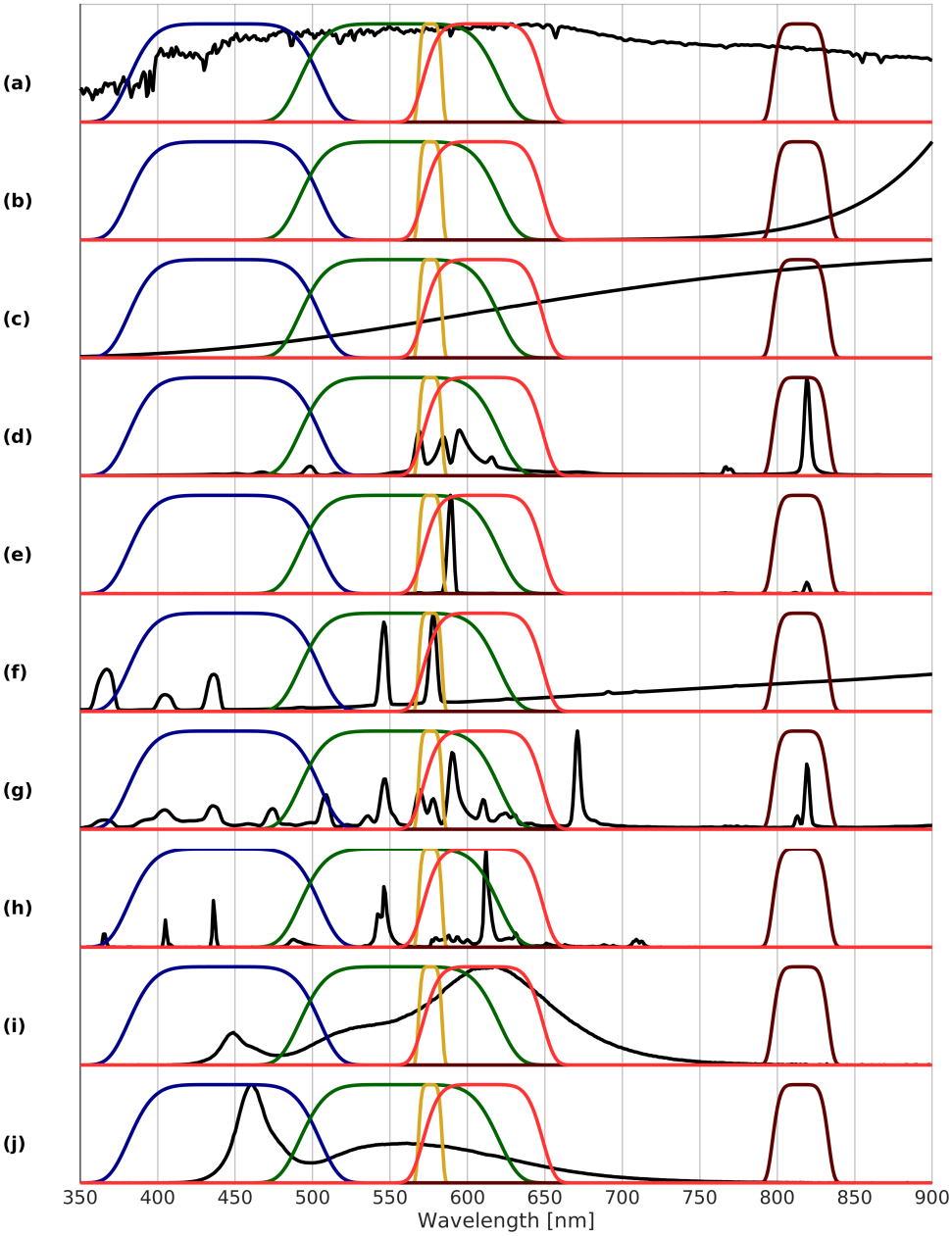

Figure 4.6: Selected band proposal and typical lamp type spectra for (a) full moon; (b) fire, 700 K; (c) incandescent bulb; (d) high-pressure sodium lamp; (e) low-pressure sodium lamp; (f) mercury vapour lamp; (g) metal halide lamp; (h) fluorescent lamp; (i) warm LED lamp; and (j) cool LED lamp [34]. Note that the y-axis represents relative radiances. Band 1 (λ_C = 556 nm, $\Delta\lambda$ = 125 nm) is depicted in green, band 2 (λ_C = 443 nm, $\Delta\lambda$ = 120 nm) in blue, band 3 (λ_C = 576 nm, $\Delta\lambda$ = 15 nm) in yellow, band 4 (λ_C = 815 nm, $\Delta\lambda$ = 35 nm) in dark red and band 5 (λ_C = 610 nm, $\Delta\lambda$ = 75 nm) in red.

ment was achieved for all relevant indices. The Nightsat mission proposal, which can be seen as the standard reference with respect to nighttime VNIR missions, does score relatively well in certain aspects. For example, the classification of level 1 and level 2 radiation source types reaches similar results as the proposal with three MS bands. However, it does not succeed in estimating emissions in the blue part of the spectrum, as is reflected by the large MAE for the spectral G index.

The knowledge on accurate spectral reflectances could offer valuable additional information for the estimation of lighting power. Such reflectance values could come from daytime optical sensors, e.g. from Sentinel-2's 10 m spatial resolution bands. The research on the influence of such synergies with Sentinel-2 bands could be a topic for further research, but remains outside the scope of this thesis. Nonetheless, when using identical spectral bands for a nighttime sensor, it is expected that the estimation of luminous efficiency, as well as the estimation of blue emissions, will be insufficiently covered.

A comparison of the three-, four- and five-band proposals reveals that the capability of all three combinations to estimate luminous efficiency and blue light is identical. The differences can be found in the ability to identify different radiation source types. Here, it is clear that the four- and five-band proposals score considerably better. It is, therefore, recommended to have a sensor with either four or five MS bands and one panchromatic band. Because of the importance of the panchromatic band, e.g. for normalisation and LER estimation, it is recommended to include a second panchromatic band, in case the design of the sensor allows this. This has the additional advantage that a combination of two panchromatic bands, with ample offset between the recording lines, has the option to generate images with a higher spatial resolution. Whether a combination with or without band B5 is preferred, depends on the specific sensor that is used. In case there is room for an extra band, the addition of B5 will increase the ability to estimate CCT. However, as it is an index with decreasing importance, an option without B5 will not sacrifice much of its application options. Other differences between the two options are negligible.

4.2. Radiometric sampling

4.2.1. Detection limit and saturation

For each of the spectral bands, typical band-averaged spectral radiance values are calculated and shown in Table 4.5. These are based on the selected luminance recommendations, lamp spectra, surface types and atmospheric inputs. It is important to note here that some of these parameters are uniformly distributed between a minimum and a maximum value, as is the case for luminance values ranging between 0.3 and 4 cd m^{-2}. Therefore, rather than covering a realistic distribution of real-world values, it reflects a range of possibilities that is evenly distributed.

Previous recommendations for the detection limits and saturation of a MS nighttime VNIR sensor have been made by Elvidge et al. [17] for the Nightsat mission concept. For what the authors called the photopic band, with wavelengths between 510 nm and 610 nm, a detection limit of $2.5 \cdot 10^{-7}$ W m^{-2} sr^{-1} nm^{-1} and a satur-

Quantile [%]	B0 [W m^{-2} sr^{-1} nm^{-1}]	B1 [W m^{-2} sr^{-1} nm^{-1}]	B2 [W m^{-2} sr^{-1} nm^{-1}]	B3 [W m^{-2} sr^{-1} nm^{-1}]	B4 [W m^{-2} sr^{-1} nm^{-1}]	B5 [W m^{-2} sr^{-1} nm^{-1}]
0	$2.9 \cdot 10^{-8}$	$6.3 \cdot 10^{-8}$	$1.4 \cdot 10^{-10}$	$4.1 \cdot 10^{-9}$	0	$8.0 \cdot 10^{-8}$
10	$3.2 \cdot 10^{-7}$	$6.3 \cdot 10^{-7}$	$9.6 \cdot 10^{-9}$	$3.3 \cdot 10^{-7}$	$1.2 \cdot 10^{-8}$	$8.2 \cdot 10^{-7}$
20	$5.4 \cdot 10^{-7}$	$1.1 \cdot 10^{-6}$	$8.2 \cdot 10^{-8}$	$7.6 \cdot 10^{-7}$	$3.8 \cdot 10^{-8}$	$1.4 \cdot 10^{-6}$
30	$8.0 \cdot 10^{-7}$	$1.5 \cdot 10^{-6}$	$1.7 \cdot 10^{-7}$	$1.3 \cdot 10^{-6}$	$9.5 \cdot 10^{-8}$	$2.0 \cdot 10^{-6}$
40	$1.1 \cdot 10^{-6}$	$2.1 \cdot 10^{-6}$	$2.7 \cdot 10^{-7}$	$1.9 \cdot 10^{-6}$	$2.7 \cdot 10^{-7}$	$2.8 \cdot 10^{-6}$
50	$1.4 \cdot 10^{-6}$	$2.7 \cdot 10^{-6}$	$4.1 \cdot 10^{-7}$	$2.9 \cdot 10^{-6}$	$9.6 \cdot 10^{-7}$	$3.7 \cdot 10^{-6}$
60	$2.0 \cdot 10^{-6}$	$3.5 \cdot 10^{-6}$	$6.0 \cdot 10^{-7}$	$4.1 \cdot 10^{-6}$	$2.4 \cdot 10^{-6}$	$4.9 \cdot 10^{-6}$
70	$2.8 \cdot 10^{-6}$	$4.5 \cdot 10^{-6}$	$8.5 \cdot 10^{-7}$	$5.8 \cdot 10^{-6}$	$4.7 \cdot 10^{-6}$	$6.8 \cdot 10^{-6}$
80	$4.4 \cdot 10^{-6}$	$6.7 \cdot 10^{-6}$	$1.4 \cdot 10^{-6}$	$8.6 \cdot 10^{-6}$	$8.8 \cdot 10^{-6}$	$9.4 \cdot 10^{-6}$
90	$8.1 \cdot 10^{-6}$	$1.2 \cdot 10^{-5}$	$2.8 \cdot 10^{-6}$	$1.6 \cdot 10^{-5}$	$1.8 \cdot 10^{-5}$	$1.5 \cdot 10^{-5}$
100	$7.1 \cdot 10^{-4}$	$4.4 \cdot 10^{-5}$	$2.7 \cdot 10^{-5}$	$1.3 \cdot 10^{-4}$	$1.8 \cdot 10^{-3}$	$1.2 \cdot 10^{-4}$

Table 4.5: Top-of-atmosphere radiance values for lamps in proposed bands with (1) B0: λ_C = 619 nm, $\Delta\lambda$ = 510 nm; (2) B1: λ_C = 556 nm, $\Delta\lambda$ = 125 nm; (3) B2: λ_C = 443 nm, $\Delta\lambda$ = 120 nm; (4) B3: λ_C = 576 nm, $\Delta\lambda$ = 15 nm; (5) B4: λ_C = 815 nm, $\Delta\lambda$ = 35 nm; and (6) B5: λ_C = 610 nm, $\Delta\lambda$ = 75 nm. Note that bottom-of-atmosphere luminance values range between 0.3 cd m^{-2} and 4 cd m^{-2}.

ation of $2.5 \cdot 10^{-1}$ W m^{-2} sr^{-1} nm^{-1} have been recommended. For the test data used in this thesis, radiances for the corresponding B1 band range from almost 10^{-7} W m^{-2} sr^{-1} nm^{-1} to $5 \cdot 10^{-5}$ W m^{-2} sr^{-1} nm^{-1}. Note that especially the upper limit is significantly lower than the saturation value recommended for Nightsat. The reasoning behind it is that the authors used the Luxor Sky Beam in Las Vegas as a reference. With a 42 billion candela tunnel of light, it is the strongest light beam in the world, and therefore occurs only once. Moreover, even with a relatively high bit depth of 16 bits and not considering gain settings, 1 DN would equal $3.8 \cdot 10^{-6}$ W m^{-2} sr^{-1} nm^{-1}, which is larger than the TOA radiance of about 60% of the lamps in the test dataset. With luminances between 0.3 and 4 cd m^{-2}, 1 DN corresponds to a luminance of approximately 2.5 cd m^{-2}, a value larger than the standard for the highest road class [57]. For a bit depth of 12 bit, the radiance corresponding to 1 DN is larger than even the largest TOA radiance in the dataset. Therefore, it is recommended for B1 to have a saturation of 10^{-3} W m^{-2} sr^{-1} nm^{-1} in the case of 16 bit and 10^{-4} W m^{-2} sr^{-1} nm^{-1} in the case fewer bits are available.

The detection limit recommended for Nightsat, on the other hand, does seem to be more or less conform to the computed values in this dataset (Table 4.5).

However, decreasing the detection limit to 10^{-7} W m^{-2} sr^{-1} nm^{-1} or lower, would extend the area of operation to the lighting of pedestrian and cycle zones. For the other bands, the distribution of band-averaged spectral radiances seems to follow that of B1 (Table 4.5), with the exception of two bands, i.e. the blue band (B2) and the near-infrared band (B4). The rather low TOA radiances in the blue band can be explained by the fact that some lamps, e.g. low-pressure and high-pressure sodium lamps, barely emit blue light. With the importance of blue light emissions in mind, even for relatively low radiances, it is recommended that the blue band has a slightly lower detection limit of 10^{-8} W m^{-2} sr^{-1} nm^{-1}. Another difference can be seen in the near-infrared band (B4), where higher values were computed, belonging to some of the high-pressure sodium lamps. Therefore, it is recommended that this band has a higher dynamic range, with a saturation value of around 10^{-3} W m^{-2} sr^{-1} nm^{-1}, even for a bit depth lower than 16 bit. Increasing the saturation value of B4 is not only useful for high-pressure sodium lamps, but additionally increases the detection rate of fire, as is discussed below.

Quantile [%]	B0 [W m^{-2} sr^{-1} nm^{-1}]	B1 [W m^{-2} sr^{-1} nm^{-1}]	B2 [W m^{-2} sr^{-1} nm^{-1}]	B3 [W m^{-2} sr^{-1} nm^{-1}]	B4 [W m^{-2} sr^{-1} nm^{-1}]	B5 [W m^{-2} sr^{-1} nm^{-1}]
0	$1.2 \cdot 10^{-14}$	$7.3 \cdot 10^{-21}$	$3.2 \cdot 10^{-26}$	$1.1 \cdot 10^{-21}$	$1.8 \cdot 10^{-14}$	$1.1 \cdot 10^{-19}$
10	$6.4 \cdot 10^{-12}$	$4.3 \cdot 10^{-17}$	$1.2 \cdot 10^{-21}$	$1.2 \cdot 10^{-17}$	$1.3 \cdot 10^{-11}$	$4.8 \cdot 10^{-16}$
20	$6.2 \cdot 10^{-10}$	$2.4 \cdot 10^{-14}$	$2.6 \cdot 10^{-18}$	$9.4 \cdot 10^{-15}$	$1.5 \cdot 10^{-9}$	$2.1 \cdot 10^{-13}$
30	$1.3 \cdot 10^{-7}$	$3.8 \cdot 10^{-11}$	$2.0 \cdot 10^{-14}$	$2.2 \cdot 10^{-11}$	$3.6 \cdot 10^{-7}$	$2.6 \cdot 10^{-10}$
40	$1.7 \cdot 10^{-6}$	$1.4 \cdot 10^{-9}$	$1.6 \cdot 10^{-12}$	$9.5 \cdot 10^{-10}$	$5.1 \cdot 10^{-6}$	$8.0 \cdot 10^{-9}$
50	$2.4 \cdot 10^{-5}$	$5.2 \cdot 10^{-8}$	$1.3 \cdot 10^{-10}$	$4.2 \cdot 10^{-8}$	$7.1 \cdot 10^{-5}$	$2.6 \cdot 10^{-7}$
60	$1.2 \cdot 10^{-4}$	$5.3 \cdot 10^{-7}$	$2.1 \cdot 10^{-9}$	$4.7 \cdot 10^{-7}$	$3.9 \cdot 10^{-4}$	$2.4 \cdot 10^{-6}$
70	$7.8 \cdot 10^{-4}$	$6.4 \cdot 10^{-6}$	$4.5 \cdot 10^{-8}$	$6.2 \cdot 10^{-6}$	$2.6 \cdot 10^{-3}$	$2.6 \cdot 10^{-5}$
80	$3.4 \cdot 10^{-3}$	$5.0 \cdot 10^{-5}$	$5.4 \cdot 10^{-7}$	$5.1 \cdot 10^{-5}$	$1.0 \cdot 10^{-2}$	$1.8 \cdot 10^{-4}$
90	$1.0 \cdot 10^{-2}$	$2.2 \cdot 10^{-4}$	$3.3 \cdot 10^{-6}$	$2.4 \cdot 10^{-4}$	$3.3 \cdot 10^{-2}$	$7.5 \cdot 10^{-4}$
100	$3.3 \cdot 10^{-2}$	$1.1 \cdot 10^{-3}$	$2.4 \cdot 10^{-5}$	$1.3 \cdot 10^{-3}$	$1.0 \cdot 10^{-1}$	$3.6 \cdot 10^{-3}$

Table 4.6: Top-of-atmosphere radiance values for fire in proposed bands with (1) B0: λ_C = 619 nm, $\Delta\lambda$ = 510 nm; (2) B1: λ_C = 556 nm, $\Delta\lambda$ = 125 nm; (3) B2: λ_C = 443 nm, $\Delta\lambda$ = 120 nm; (4) B3: λ_C = 576 nm, $\Delta\lambda$ = 15 nm; (5) B4: λ_C = 815 nm, $\Delta\lambda$ = 35 nm; and (6) B5: λ_C = 610 nm, $\Delta\lambda$ = 75 nm. Note that fire temperatures range between 400 K and 1200 K.

Although the main focus is on urban areas, the detection of fire might be an interesting byproduct of a dedicated nighttime VNIR sensor. Performing a similar

analysis for fire spectra with temperatures between 400 K and 1200 K results in Table 4.6. The highest TOA band-averaged radiances are not surprisingly located in band B4, in the near-infrared part of the spectrum. However, even this band cannot detect all fires, given the detection limit and saturation values recommended for lamps. For a typical atmospheric transmission of 70%, a detection limit of 10^{-7} W m^{-2} sr^{-1} nm^{-1} for B4 roughly corresponds to fires of 550 K, while a saturation value of 10^{-3} W m^{-2} sr^{-1} nm^{-1} for B4 roughly correspond to a temperatures of 750 K. However, the saturation value is less of an issue, as radiance values are lower in the panchromatic band B0, for example, thereby not exceeding the saturation threshold value. As a consequence, most fires with temperatures exceeding 550 K should be detectable by the recommended sensor. These temperatures cover most of the forest fires [66], meaning that the proposed spectral bands, with their detection limits and saturation values, can serve as an additional tool for fire detection programs. Although the VNIR part of the spectrum does not cover the radiation peak of fires, as given by Wien's displacement law, there is an important difference with respect to daytime optical sensors. The lower detection limits that are required for nighttime VNIR sensors offer an opportunity to detect the lower radiances that are emitted by fires in the VNIR region, typically not visible to daytime VNIR sensors.

Another source of VNIR light at night, although at lower intensities, comes from the Moon. For a standard atmosphere (i.e. mid-latitude summer atmosphere, 23 km visibility and urban aerosols) and a constant albedo of 20%, typical for road surfaces, TOA band-averaged spectral radiances for full moon conditions range between $1.5 \cdot 10^{-7}$ W m^{-2} sr^{-1} nm^{-1} for the blue band (B2) and $2.5 \cdot 10^{-7}$ W m^{-2} sr^{-1} nm^{-1} for B5. As these values exceed the recommended detection limit, it is necessary to model out moonlight in most cases. Modelling moon irradiance values should be relatively straightforward, as is explained in Section 3.1.2. Spectral reflectances can be approximated using existing daytime sensors, e.g. Sentinel-2, while atmospheric influences can be modelled through atmospheric correction. Moonlight can also be used for snow cover detection and cloud mask generation. With typical albedo values for snow and clouds around 95% and 70%, their respective TOA radiances range between $5 \cdot 10^{-7}$ W m^{-2} sr^{-1} nm^{-1} and 10^{-6} W m^{-2} sr^{-1} nm^{-1}. This means that under full moon conditions, it should be possible to detect both clouds and snow cover. However, in comparison to other existing nighttime missions, its ability to detect such phenomena would be limited. This can be explained by the lower spatial resolution of other missions, which allows detection limits to be significantly lower. For example, VIIRS DNB data has a detection limit of $2 \cdot 10^{-10}$ W m^{-2} sr^{-1} nm^{-1}. An advantage to those missions, however, is exactly the higher spatial resolution, necessary for the spectral analysis of lighting characteristics. It can, therefore, be concluded that a MS VNIR sensor would be an interesting supplement to the availability of current nighttime data with respect to cloud and snow cover detection.

4.2.2. Bit depth

The performance metrics for LER, spectral G index and classification that have been computed above, are based on sensor signals before they are being converted into a digital number (DN). This means that the results will be slightly worse in a realistic setup, since certain small radiance differences will be lost as a result of radiometric sampling. With the above-mentioned spectral bands and their recommended detection limits and saturation levels, additional analyses have been carried out for different bit depths (Table 4.7). In comparison to the case without radiometric sampling, the F1 score for level 1 classification decreases more than for level 2 classification. This difference can be mainly ascribed to the decrease in classification performance for the fire class, with its F1 score contributing to 25% of the level 1 mean F1 score, compared to only 11.1% contribution to the level 2 F1 score. The reason for this drop in performance can be almost completely attributed to the saturation limit of the near-infrared band (B4).

For most bit depths, classification results are more or less stable, with the exception of an 8 bit conversion, which produces significantly deteriorated F1 scores. While the conversion to 10 bit still succeeds at classifying most of the radiation sources, the ability to estimate luminous efficiency and blue light has drastically declined with respect to larger bit depths, with its values unacceptable for proper use. It is, therefore, recommended to apply a radiometric sampling of at least 12 bit, with higher bit depths not considerably better.

4.3. Spatial sampling

The spatial resolution that is required for a VNIR nighttime sensor depends completely on the objective of such a mission. It depends especially on the scale of the objects that need to be detected. For example, if the mission's focus is on street level, a different resolution will be required, compared to the single-lamp level. Other sensors, such as the VIIRS DNB, rather focus on the city level and block level (Table 1.1). However, for such spatial resolutions, the MS approach makes little sense, since the signal that arrives at the sensor consists of a multitude of lamp signals and lamp types, turning the estimation of LER, G index and radiation type meaningless. Therefore, the focus will be on the single-lamp level here. For such analyses, POV-Ray is used for the simulation of modelled satellite images, as is described in Section 2.6. For simplification reasons, only panchromatic simulations are carried out. Reducing the spectral resolution as such is not likely to change the detectability of lamps. Moreover, intensity distributions are only given for the whole spectrum, with single-nanometre intensity distributions not practical.

4.3.1. Single lamp

First, the single lamp situation is analysed. Although this does not contribute to the determination of ideal spatial resolutions, for which at least two lamps are required, it leads to valuable information on the nature of single-lamp images and on the performance of applying the SIFT algorithm for lamp detection. The first case consists of a single lamp, at a height of 10 m, and a single surface, with a

	∞bit	16 bit	14 bit	12 bit	10 bit	8 bit
MAE (LER)	12.66	35.71	36.38	37.24	116.77	283.10
MAE (G)	0.081	0.118	0.128	0.169	0.715	1.804
MAE (CCT)	391	413	414	414	432	737
Mean F1 score (level 1)	0.886	0.811	0.794	0.809	0.807	0.706
Mean F1 score (level 2)	0.900	0.842	0.861	0.865	0.839	0.690
Overall accuracy (level 1)	0.915	0.855	0.837	0.850	0.834	0.759
Overall accuracy (level 2)	0.880	0.794	0.774	0.787	0.768	0.662

Table 4.7: Performance comparison for different bit depths for proposed band selection, detection limits and saturation values. Note that the 16 bit results are based on a saturation value of 10^{-3} W m^{-2} sr^{-1} nm^{-1} instead of 10^{-4} W m^{-2} sr^{-1} nm^{-1} for the other options.

homogeneous albedo (Fig. 4.7). The elongated shape of its resulting light pattern, usually along the street orientation, is immediately visible. Note that the small black dot in the image represents the physical shape of the lamp itself, which blocks reflected light from reaching the satellite's sensor. Furthermore, to allow lamps to stand at the roadside, most of its light is directed to the side of the lamp at which the road is located. As a consequence, road light patterns differ significantly from the typical point source. To analyse the performance potential of the SIFT algorithm, two one-dimensional cross-sections, going through the lamp's central position, are investigated. Additionally, the Difference of Gaussians (DoG), central to the SIFT algorithm, is computed for different σ values along the cross-section. The local minimum should then, theoretically, lead to the optimal position of the lamp.

For the cross-section that stretches along the road direction, intensity values and their resulting DoG values can be seen in Figure 4.8. In the figure, the lamp's position is indicated by a dotted black line. Along this cross-section, the lamp's intensity signal (Fig. 4.8a) is clearly symmetrical with respect to its centre. Note the through at $x = 0$ m, which corresponds to the physical presence of the luminaire itself. It is obvious, however, that for sensible spatial resolutions, this through, i.e. a small black dot of zero radiance, will no longer be visible in the image. Its detectability is further hampered by the adjacency effect, as a result of atmospheric conditions. The intensity's symmetry is, as expected, also reflected into the DoG

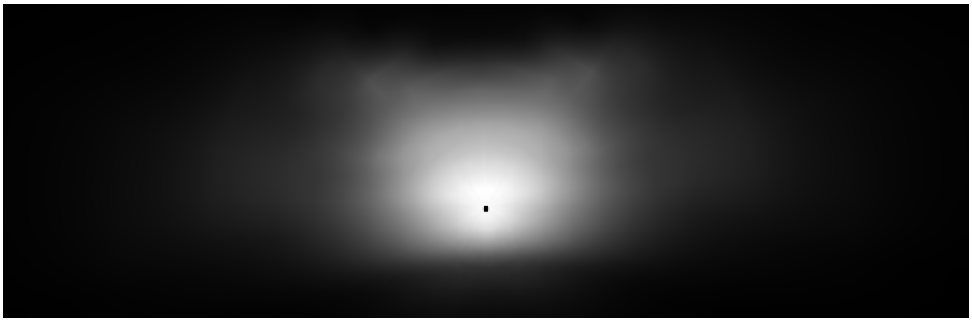

Figure 4.7: Panchromatic image of a single lamp's emissions reflecting on a single surface. Note that the intensity distribution pattern is that of a Leotek GreenCobra M2 LED street light of type 2R, at a mounting height of 10 m. The small black dot in the middle represents the physical shape of the lamp itself, which blocks the reflected light underneath from reaching the sensor.

values (Fig. 4.8b). Here, a local minimum can be found for x = 0 m and σ = 68.7. This gives an indication that SIFT, or similar algorithms, has the ability to detect single individual lamps. It could be suggested that there is also a maximum peak at the same x-coordinate. However, this peak is a result of the through that comes with the lamp's physical shape. Hence, it will no longer be useful for reasonable spatial resolution choices, as has been mentioned above.

In comparison to the along-road cross-section, the across-road case (Fig. 4.9) shows a slightly different outcome. For example, as most of the light is directed towards the road, the intensity cross-section (Fig. 4.9a) is clearly asymmetrical with respect to the lamp's centre. This asymmetry is also reflected into the DoG values, as is visible through the shift of its local minimum towards the road's centre, instead of the lamp's physical position. This positioning error, however, will be difficult to circumvent directly, even with different algorithms. The reason for this is that the aim of road lighting is to have most of its light directed at the middle of the road, instead of beneath the lamp's centre. Its light, therefore, generates a blob in the image that has its centre on the road. Nonetheless, if combined with positional data of roads, correcting for this position error should be possible. On the other hand, when two neighbouring lamps are spaced by some distance, their illumination centres will be nearer to each other.

4.3.2. Row of lamps

To arrive at recommendations concerning the spatial resolution of a nighttime VNIR sensor which focuses on artificial lighting, the spacing between different lamps, in combination with their mounting height, plays an important role. Typical values for these variables were derived from Narisada et al. [68] and lighting engineering standards [57]. This leaded to three different cases, i.e. (1) a spacing of 25 m and mounting heights of 6 m for residential roads; (2) a spacing of 40 m and mounting heights of 10 m for roads with a mixed function; and (3) a spacing of 60 m and mounting heights of 18 m for major roads. For each of these cases, simulations were then made for some sensible spatial resolution options, i.e. GSD = 1 m,

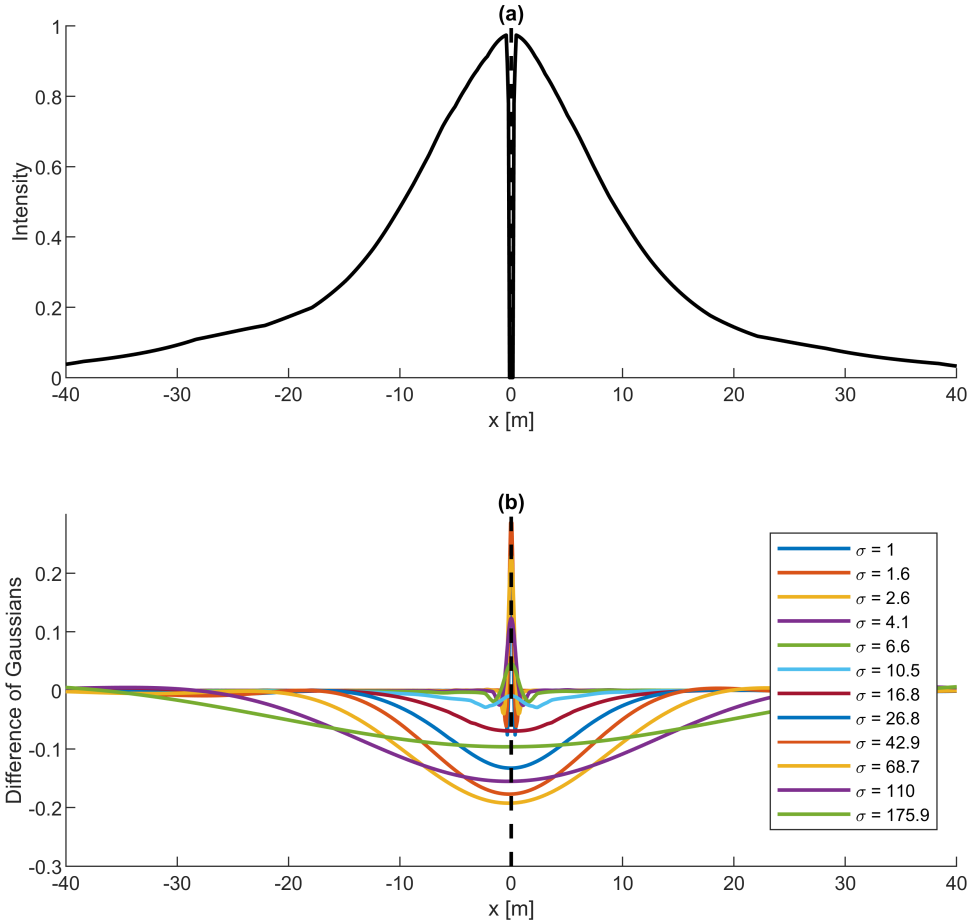

Figure 4.8: Application of DoG method to the cross-section, along a road surface, of a single lamp top-of-atmosphere radiance image with (a) intensity cross-section; and (b) DoG cross-section for different σ values. Note that the intensity distribution pattern is that of a Leotek GreenCobra M2 LED street light of type 2R, at a mounting height of 10 m. The dotted line represents the location of the lamp centre.

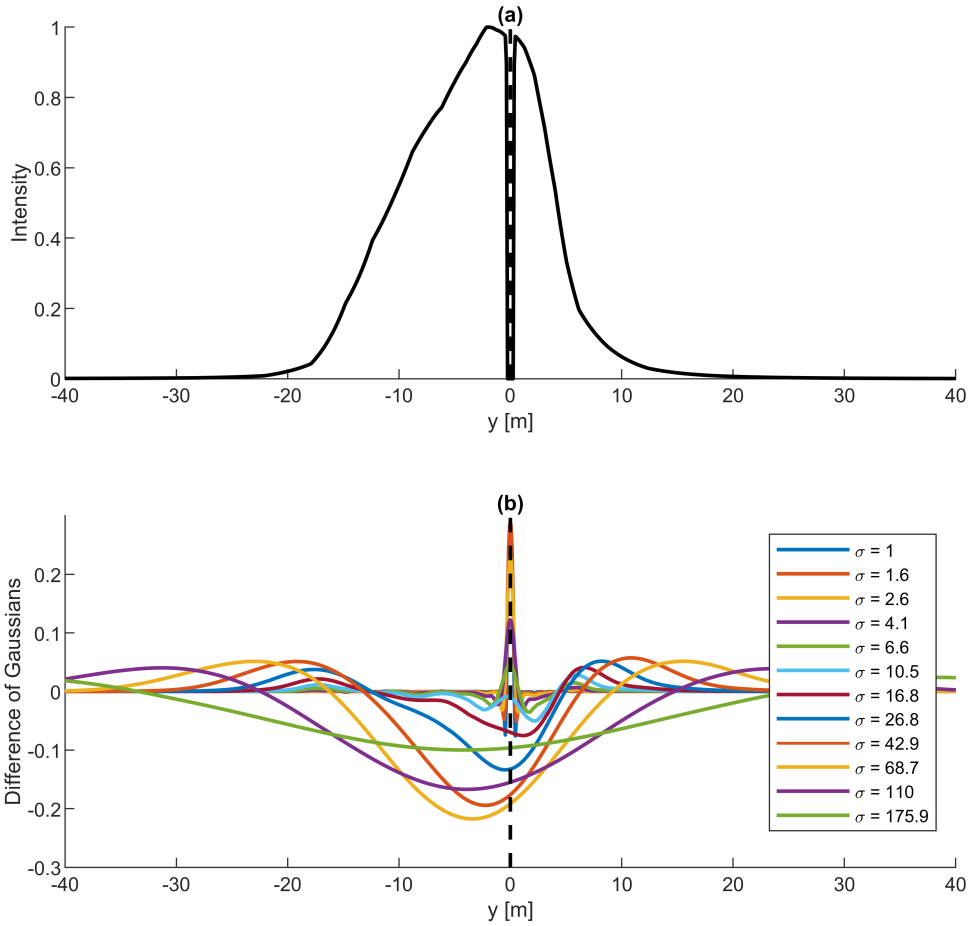

Figure 4.9: Application of DoG method to the cross-section, across a road surface, of a single lamp top-of-atmosphere radiance image with (a) intensity cross-section; and (b) DoG cross-section for different σ values. Note that the intensity distribution pattern is that of a Leotek GreenCobra M2 LED street light of type 2R, at a mounting height of 10 m. The dotted line represents the location of the lamp centre.

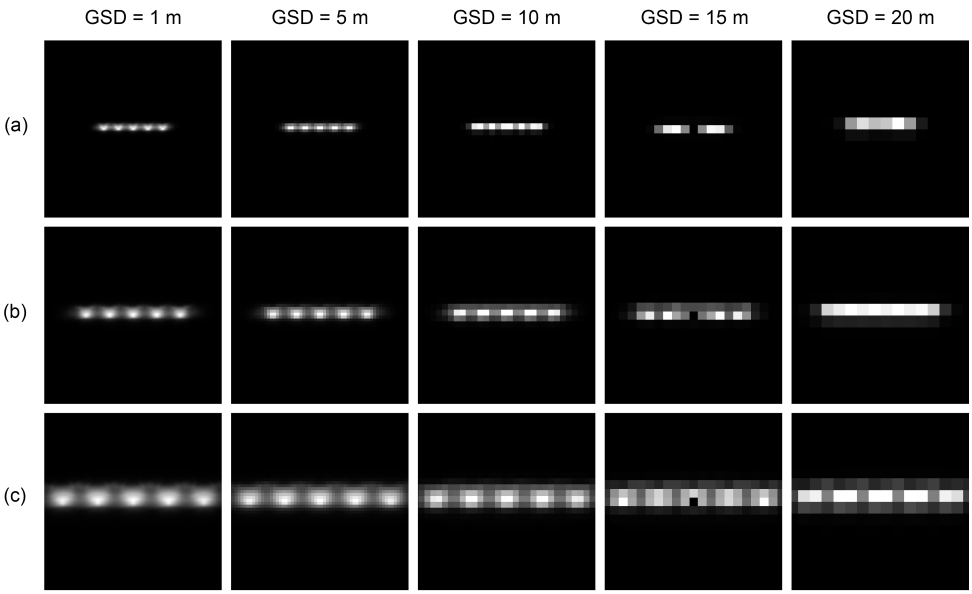

Figure 4.10: Row of five lamps with different spacing and mounting height at different spatial resolutions, with (a) Leotek GreenCobra Jr. 15H 2R 300S lamps, spacing = 25 m, height = 6 m; (b) Leotek GreenCobra Midsize 30H 2R 530 lamps, spacing = 40 m, height = 10 m; (c) Leotek GreenCobra Large 60G 2R 750 lamps, spacing = 60 m, height = 18 m.

GSD = 5 m, GSD = 10 m, GSD = 15 m and GSD = 20 m. Note that for each case, a slightly different lamp was chosen, as intensity distributions depend strongly on the mounting height for which they are designed. These differences, however, should not affect results significantly.

When considering spatial sampling and required spatial resolutions, one quickly arrives at the Nyquist sampling theorem. This theorem states that the sampling frequency should be at least twice the highest frequency contained in a signal. Applying this logic here means that the required GSD should equal half of the spacing, or less, between neighbouring lamps. With a minimum spacing of 25 m, this results in a GSD of 12.5 m or less. Lower spacing distances do occur, but are not frequent. Moreover, neighbouring lamps usually possess similar characteristics, which makes the detection of individual lamps not necessarily required in all cases.

Notwithstanding the above-mentioned prediction, road lighting does not behave like a regular point source. As has been described in Section 4.3.1, intensity distributions have a major influence on the positioning estimation of lamps. The results predicted by the Nyquist theorem, however, can be confirmed by Figure 4.10. For a lamp spacing of 60 m (Fig. 4.10c), all five lamps can be clearly identified for spatial resolutions ranging from 1 m to 20 m. In the other two cases, i.e. with a lamp spacing of 25 m (Fig. 4.10a) and 40 m (Fig. 4.10b), a GSD of 10 m is required. Similar conclusions can be drawn from Table 4.8, which shows the results from the SIFT detection. Note that the size of the error increases with increased spacing.

		GSD = 1 m	GSD = 5 m	GSD = 10 m	GSD = 15 m	GSD = 20 m
25 m spacing	100% detection	X	X	X		
	RMSE [m]	3.47	3.91	5.54	-	-
40 m spacing	100% detection	X	X	X		
	RMSE [m]	4.96	4.91	4.23	-	-
60 m spacing	100% detection	X	X	X	X	X
	RMSE [m]	6.51	6.44	6.57	6.63	9.87

Table 4.8: Detection results for a single row of lamps at various spatial resolutions.

This is a result of the fact that SIFT does not detect the position of the lamp, but instead detects the centre of the lit area. With increased mounting height, which accompanies increased spacing, the area of the lit area increases, which in turn increases the across-road positioning error. Note that, as has been mentioned previously, this error can probably be reduced by introducing data on road positions. However, further research is required here.

4.3.3. Lamp arrangements

For larger-sized roads, such as dual-carriageways, lamps are usually not arranged in single rows. Instead, there are different options for their arrangement, with the most common being a one-sided arrangement (Fig. 4.11a), a two-sided staggered arrangement (Fig. 4.11b), a two-sided opposite arrangement (Fig. 4.11c), a central arrangement (Fig. 4.11d) and a twin-central arrangement (Fig. 4.11e) [69]. Both the one-sided arrangement and the central arrangement options are sufficiently covered by the single-row arrangement, as discussed in Section 4.3.2. Simulations for the remaining arrangements are carried out for different spatial resolutions, for lamps with a spacing of 40 m (Fig. 4.12). Note that a spacing of 25 m is not relevant, as it corresponds to relatively narrow roads in a residential area, for which a single-sided arrangement would be the preferred option.

From Figure 4.11, it is already obvious that distinguishing between individual lamps might be difficult for some of the arrangements. Especially for the twin-central arrangement (Fig. 4.11c), where a simulation for ten lamps is carried out, it seems from the image that only five of them are actually there. Identical conclusions can be drawn from the SIFT detection (Table 4.9), with only 50% of the lamps

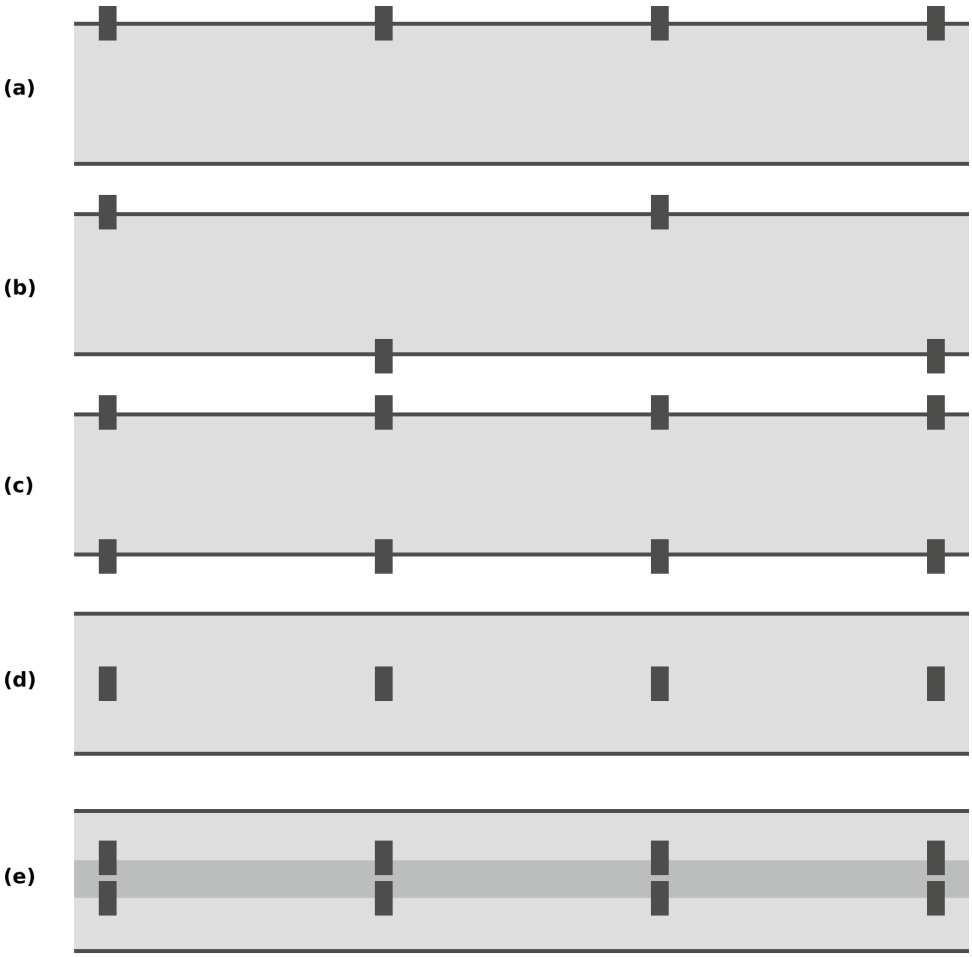

Figure 4.11: Overview of different road lighting arrangements, with (a) one-sided arrangement; (b) two-sided staggered arrangement; (c) two-sided opposite arrangement; (d) central arrangement; and (e) twin central arrangement. Adapted from *Road lighting: Fundamentals, technology and application*, by W. van Bommel, 2015, p. 184.

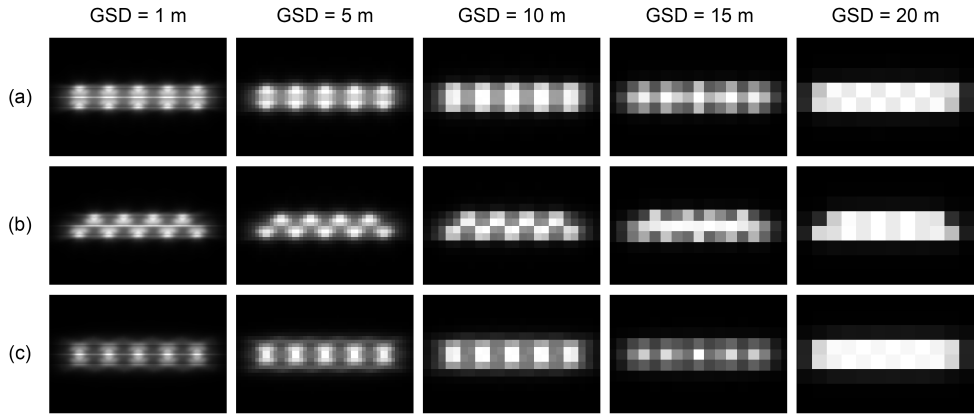

Figure 4.12: Different road lighting arrangements at different spatial resolutions, with (a) two-sided opposite arrangement; (b) two-sided staggered arrangement; and (c) twin central arrangement. The surface is composed of a dual carriageway, with the spacing between the lamps being 40 m.

detected. This is a result of the nature of such a twin-central arrangement, where two neighbouring twins are that close to each other that they have almost identical coordinates. A thorough pattern analysis of the pixels involved might lead to the conclusion that the detection in fact corresponds to two different lamps, but such analysis remains outside the scope of this thesis. Moreover, since the two twin lamps will possess identical characteristics, there is no issue in classifying them as a single lamp.

In contrast, it is considerably easier to detect individual lamps for two-sided staggered arrangements. Once more, a spatial resolution of 10 m represents the threshold for proper detection (Fig. 4.12b and Table 4.9). Note that the GSD has no significant influence on the size of the error. The two-sided opposite arrangement, on the other hand, shows results that lie somewhere in between that of the two-sided staggered arrangement and the twin-central arrangement. In other words, the lit areas of two opposite lamps do not merge for all spatial resolutions, but as the GSD increases, it becomes impossible to distinguish them.

Combining the recommended spatial resolution of 10 m with the relatively low detection limits that have been recommended in Section 4.2.1, could prove to be a difficult task. Note that, instead, there is a possibility of combining two panchromatic bands. One band could combine a high spatial resolution of 10 m with higher detection limits, thereby only focusing on lamp detection. A second band, on the other hand, could have lower detection limits, combined with lower spatial resolutions of, e.g., 20 m or 40 m.

		GSD = 1 m	GSD = 5 m	GSD = 10 m	GSD = 15 m	GSD = 20 m
Two-sided opposite	100% detection	X				
	50% detection		X	X	X	
	RMSE [m]	4.28	-	-	-	-
Two-sided staggered	100% detection	X	X	X		
	50% detection					
	RMSE [m]	2.25	2.72	1.73	-	-
Twin central	100% detection					
	50% detection	X	X	X	X	
	RMSE [m]	-	-	-	-	-

Table 4.9: Detection results for different lamp arrangements at various spatial resolutions, with a lamp spacing of 40 m.

5

Conclusion and future work

5.1. Conclusion

In order to determine the recommended spectral, radiometric and spatial characteristics of a dedicated multispectral nighttime visible and near-infrared sensor, a spectral library of top-of-atmosphere radiances was simulated, based on a combination of some typical theoretical fire spectra, lamp spectral libraries, standard luminance values for road surfaces, a surface reflectance library and the estimation of atmospheric effects. Similarly, a series of test data has been simulated as well. These test data, however, do not contain the limited choice of typical spectra, as is the case for the spectral library. Instead, spectra are randomly picked from a full range of realistic options, with a noise model additionally determining the respective noise. Based on the generated spectral library and test data, the ability of different spectral band combinations to estimate relevant light characteristics and to discriminate between lighting types, was analysed. Table 5.1 gives an overview of the recommended sensor parameters for multispectral visible and near-infrared nighttime remote sensing.

Important lighting quality parameters, both for research purposes as well as for use by the lighting industry, were found to be (1) the required electrical power, which can be approximated by a lamp's radiant power; (2) the luminous efficacy or the ability to turn electrical power into visible light; (3) the spectral G index, or the amount of emitted blue light with respect to the amount of visible light; and (4) the correlated colour temperature, assessing the perceived colour of the light emitted by a lamp. With the estimation of the required electrical power depending on a myriad of variables, of which some are rather difficult to model, its estimation remained outside the scope of this thesis. However, the ability to estimate electrical power consumption does not depend strongly on the choice of sensor characteristics. Therefore, its omission has little effect on the outcomes of this thesis. In order to determine luminous efficacy, a combination of two spectral bands was found to be optimal. One of them is band B0, with a central wavelength (CW) of 619 nm

	λ_C [nm]	$\Delta\lambda$ [nm]	detection limit [W m^{-2} sr^{-1} nm^{-1}]	saturation [W m^{-2} sr^{-1} nm^{-1}]	bit depth	GSD [m]
B0	619	510	10^{-7}	10^{-4}	12 bit	10
B1	556	125	10^{-7}	10^{-4}	12 bit	40
B2	443	120	10^{-8}	10^{-4}	12 bit	40
B3	576	15	10^{-7}	10^{-4}	12 bit	40
B4	815	35	10^{-7}	10^{-3}	12 bit	40
B5	610	75	10^{-7}	10^{-4}	12 bit	40

Table 5.1: Overview of recommended spectral bands and their radiometric and spatial resolution.

and a full width at half maximum (FWHM) of 510 nm. This band can be used to estimate a lamp's radiant power, and additionally serves as the panchromatic band. Furthermore, band B1, with a CW of 556 nm and an FWHM of 125 nm, was found to be optimal to estimate the amount of light that is visible to the human's eye. The ratio of these two bands then leads to a good estimation of luminous efficacy of radiance. Note that luminous efficacy of radiance is estimated, and not luminous efficacy. The reason for it is that luminous efficacy not only depends on optical power, but instead depends on the amount of electrical power.

Recently, with the increased attention for human environmental impacts, more focus is put on the emissions in the blue part of the spectrum. In order to be able to estimate such impacts, the spectral G index is used as a reference. It is a measure for the ratio of blue light emissions divided by the total amount of visible light. With the total amount of visible light already estimated by B1, one additional band is required in the blue part of the spectrum. The optimal blue band, B2, has a CW of 443 nm and an FWHM of 120 nm. In contrast to other existing nighttime satellites, this band offers a substantial improvement in terms of estimating blue light emissions. The last lighting parameter is that of correlated colour temperature. Since it assesses the perceived colour of a lamp and with blue light already covered by B2 and green light covered by B1, an additional band B5 in the red part of the spectrum was required for its precise estimation. Correlated colour temperature was optimally estimated with B5 having a CW of 610 nm and an FWHM of 75nm. However, it needs to be noted that the usage of correlated colour temperature has lost some of its importance in recent years. Band B5 is, therefore, the first band that can be omitted without much loss of practical utility, in case a particular sensor design does not allow six bands.

In order to estimate some of these indices, identifying the light source type can lead to valuable information. Most lights that belong to the same class share similar

properties, which can be used, e.g., for the estimation of electrical power. These classes include (1) combustion; (2) incandescent lamps; (3) high-pressure sodium lamps; (4) low-pressure sodium lamps; (5) mercury vapour lamps; (6) fluorescent lamps; (7) metal halide lamps; (8) warm LED lamps; and (9) cool LED lamps. Based on the simulated spectral library, the simulated test data and a one-vs-all k-nearest neighbour classification for different band combinations, it was found that two additional bands are optimal for discriminating lighting types, i.e. B3 with a CW of 576 nm and an FWHM of 15 nm, and B4 with a CW of 815 nm and an FWHM of 35 nm. In comparison to other band combinations, the recommended setup leads to an increase of the F1 score of about 10%, with the estimation of other indices also significantly improved.

Based on the spectral recommendations for a nighttime optical satellite sensor, typical top-of-atmosphere band-averaged radiance values were computed for lamps, leading to recommendations concerning the required detection limit and saturation values. For all bands, a detection limit of 10^{-7} W m^{-2} sr^{-1} nm^{-1} is recommended, with the exception of the blue band B2, for which a slightly larger sensitivity of 10^{-8} W m^{-2} sr^{-1} nm^{-1} is recommended. Saturation values, on the other hand, are recommended to be around 10^{-4} W m^{-2} sr^{-1} nm^{-1} for most bands, with the exception of the near-infrared band, for which a saturation limit of 10^{-4} W m^{-2} sr^{-1} nm^{-1} is preferred. After comparison of these values with typical fire, cloud and snow properties under full moon conditions, it is found that the recommended sensitivities are sufficient to allow detection in most cases.

The above-mentioned index estimations and classifications are based on data that is not yet radiometrically sampled. In order to determine the required bit depth, identical simulations have, therefore, been run for different bit depths. Results indicated that 12 bit was found to be the threshold case, with lower bit depths not sufficient for either light source identification or index estimation.

Finally, in order to determine the optimal spatial resolution of a nighttime optical sensor, a physically-based rendering software was used to generate realistic synthetic images of some basic road lighting situations. For typical lamp spacing distances, a ground sample distance of 10 m is required to identify individual lamps. However, for some lamp arrangements, e.g. the twin-central arrangement, it was impossible to distinguish between individual lamps, even at higher spatial resolutions. Instead, under these circumstances, two lamps were detected as one. With additional knowledge on street location and a pattern analysis of the radiances, for example, this could be overcome. More research is, however, required in this area. In order to make image fusion of the panchromatic and multispectral bands possible, the multispectral bands are recommended to have a ground sample distance of 40 m.

5.2. Future work

Nighttime images with high spectral and high spatial resolutions are a relatively unexplored field. The options for future research are, therefore, plentiful. One such area of interest is the estimation of radiant power. Previous research has already scratched the surface of this topic. However, further research is needed, especially

for the more specific case of higher spatial resolutions. Such estimations need accurate surface reflectance data and aerosol data. Whether such information can be deduced directly from a visible and near-infrared nighttime sensor, needs further examination. One idea to estimate surface reflectance values could be through synergies with the spectral bands with existing daytime sensors, e.g. Sentinel-2. Atmospheric transmittance, on the other hand, could be estimated by making use of time series, for example, or ground truth data on lamps with known characteristics. Additionally, in order to comply with the cloud-free assumption applied in this thesis, a proper cloud detection algorithm is required. This could be based on either the existing visible and near-infrared bands, or on the addition of a thermal sensor. Such a thermal sensor would also improve the ability to detect fires, for example.

An important index that was not covered here is the amount of upward emissions by a lamp. These emissions are generally the result of missing lamp shading. A distinction between reflected and upward emissions, however, is not easily done, if at all possible. In the second part of this thesis, only a limited number of controlled environments were simulated in order to generate realistic optical nighttime images. The next step in this process could be to simulate more complex scenes, based on in-situ measurements, digital surface models, measured reflectance spectra and adding additional noise factors such as industrial lighting or vehicle lights. Further research is also needed to develop nighttime-specific algorithms for the estimation of single lamp positions and lighting type classification. It can be stated that, With the aforementioned areas of research only touching upon a small part of the countless opportunities, simulating detailed nighttime data could be the first step towards a better understanding of nighttime visible and near-infrared remote sensing.

References

[1] Huang, Q., Yang, X., Gao, B., Yang, Y. & Zhao, Y. (2014). Application of DMSP/OLS nighttime light images: A meta-analysis and a systematic literature review. *Remote Sensing*, *6*(8), 6844–6866.

[2] Miller, S. D., Straka, W., Mills, S. P., Elvidge, C. D., Lee, T. F., Solbrig, J., … Weiss, S. C. (2013). Illuminating the capabilities of the Suomi National Polar-orbiting Partnership (NPP) Visible Infrared Imaging Radiometer Suite (VIIRS) Day/Night Band. *Remote Sensing*, *5*(12), 6717–6766.

[3] Zhao, M., Zhou, Y., Li, X., Cao, W., He, C., Yu, B., … Zhou, C. (2019). Applications of satellite remote sensing of nighttime light observations: Advances, challenges, and perspectives. *Remote Sensing*, *11*(17), 1971.

[4] Chen, Z., Yu, B., Song, W., Liu, H., Wu, Q., Shi, K. & Wu, J. (2017). A new approach for detecting urban centers and their spatial structure with nighttime light remote sensing. *IEEE Transactions on Geoscience and Remote Sensing*, *55*(11), 6305–6319.

[5] Bennett, M. M. & Smith, L. C. (2017). Advances in using multitemporal nighttime lights satellite imagery to detect, estimate, and monitor socioeconomic dynamics. *Remote Sensing of Environment*, *192*, 176–197.

[6] Cho, Y., Ryu, S. H., Lee, B. R., Kim, K. H., Lee, E. & Choi, J. (2015). Effects of artificial light at night on human health: A literature review of observational and experimental studies applied to exposure assessment. *Chronobiology International*, *32*(9), 1294–1310.

[7] Bennie, J., Davies, T. W., Cruse, D. & Gaston, K. J. (2016). Ecological effects of artificial light at night on wild plants. *Journal of Ecology*, *104*(3), 611–620.

[8] Shi, K., Yu, B., Huang, Y., Hu, Y., Yin, B., Chen, Z., … Wu, J. (2014). Evaluating the ability of NPP-VIIRS nighttime light data to estimate the gross domestic product and the electric power consumption of China at multiple scales: A comparison with DMSP-OLS data. *Remote Sensing*, *6*(2), 1705–1724.

[9] Elvidge, C. D., Ziskin, D., Baugh, K., Tuttle, B., Ghosh, T., Pack, D., … Zhizhin, M. (2009). A fifteen year record of global natural gas flaring derived from satellite data. *Energies*, *2*(3), 595–622.

[10] Elvidge, C. D., Zhizhin, M., Hsu, F. & Baugh, K. (2013). VIIRS nightfire: Satellite pyrometry at night. *Remote Sensing*, *5*(9), 4423–4449.

[11] Elvidge, C. D., Zhizhin, M., Baugh, K. & Hsu, F. (2015). Automatic boat identification system for VIIRS low light imaging data. *Remote Sensing*, *7*(3), 3020–3036.

[12] Chen, T.-H. K., Prishchepov, A. V., Fensholt, R. & Sabel, C. E. (2019). Detecting and monitoring long-term landslides in urbanized areas with nighttime light data and multi-seasonal Landsat imagery across Taiwan from 1998 to 2017. *Remote Sensing of Environment*, *225*, 317–327.

[13] Li, X., Liu, S., Jendryke, M., Li, D. & Wu, C. (2018). Night-time light dynamics during the Iraqi civil war. *Remote Sensing*, *10*(6), 858.

[14] Kingslake, R. (1942). Lenses for aerial photography. *Journal of the Optical Society of America*, *32*, 129–134.

[15] Croft, T. A. (1978). Nighttime images of the Earth from space. *Scientific American*, *239*(1), 86–101.

[16] Cinzano, P., Falchi, F., Elvidge, C. D. & E., B. K. (2000). The artificial night sky brightness mapped from DMSP Operational Linescan System measurements. *Monthly Notices of the Royal Astronomical Society*, *318*(3), 641–657.

[17] Elvidge, C. D., Cinzano, P., Pettit, D. R., Arvesen, J., Sutton, P., Small, C., … Ebener, S. (2007). The Nightsat mission concept. *International Journal of Remote Sensing*, *28*(12), 2645–2670.

[18] Doll, C. N. H. (2008). *CIESIN thematic guide to night-time light remote sensing and its applications*. Palisades, NY: Center for International Earth Science Information Network, Columbia University.

[19] Colomb, R., Alonso, C. & Nollmann, I. (2001). SAC-C mission and the international AM constellation for Earth observation-CONAE – Argentina. In H. P. Roser, R. Sandau & A. Valenzuela (Eds.), *Proceedings of the Third International Symposium of the International Academy of Astronautics, Berlin, April 2–6, 2001* (433–437).

[20] Sen, A., Kim, Y., Caruso, D., Lagerloef, G., Colomb, R., Yueh, S. & Le Vine, D. (2006). Aquarius/SAC-D mission overview. In *SPIE Remote Sensing proceedings volume 6361, 11-14 September 2006: Sensors, systems, and next-generation satellites X* (p. 63610I).

[21] Pack, D. W., Ardila, D. R., Herman, E., Rowen, D. W., Welle, R. P., Wiktorowicz, S. J. & Hattersley, B. W. (2017). Two aerospace corporation CubeSat remote sensing imagers: CUMULOS and R3. In *Proceedings of the AIAA/USU conference on small satellites, CubeSat session 3* (SSC17-III-05.2017).

[22] Jiang, W., He, G., Long, T., Guo, H., Yin, R., Leng, W., … Wang, G. (2018). Potentiality of using Luojia 1-01 nighttime light imagery to investigate artificial light pollution. *Sensors*, *18*(9), 2900.

[23] Pack, D. W. & Hardy, B. S. (2016). CUBESAT nighttime lights. In *Proceedings of the AIAA/USU conference on small satellites, CubeSat session IV: LEO missions* (SSC16-WK-44).

[24] de Miguel, A. S., Castaño, J. G., Zamorano, J., Pascual, S., Ángeles, M., Cayuela, L., … Kyba, C. C. (2014). Atlas of astronaut photos of Earth at night. *Astronomy & Geophysics*, *55*(4), 4.36.

[25] Zheng, Q., Weng, Q., Huang, L., Wang, K., Deng, J., Jiang, R., … Gan, M. (2018). A new source of multi-spectral high spatial resolution night-time light imagery: JL1-3B. *Remote Sensing of Environment*, *215*, 300–312.

[26] Levin, N., Johansen, K., Hacker, J. M. & Phinn, S. (2014). A new source for high spatial resolution night time images: The EROS-B commercial satellite. *Remote Sensing of Environment*, *149*, 1–12.

[27] Justice, C. O., Román, M. O., Csiszar, I., Vermote, E. F., Wolfe, R. E., Hook, S. J., … Masuoka, E. J. (2013). Land and cryosphere products from Suomi NPP

VIIRS: Overview and status. *Journal of Geophysical Research: Atmospheres*, *118*(17), 9753–9765.

[28] Elvidge, C. D. & Green, R. O. (2005). High- and low-altitude AVIRIS observations of nocturnal lighting. In *13th JPL Airborne Earth Science Workshop, May 24-27, 2005, Pasadena, CA*. Pasadena, CA: Jet Propulsion Laboratory, National Aeronautics and Space Administration.

[29] Walczak, K. (2019). Mission NiteLite: Rescuing the night sky. Retrieved June 13, 2019, from http://www.adlerplanetarium.org/mission-nitelite-rescuing-night-sky/

[30] Kuechly, H. U., Kyba, C. C., Ruhtz, T., Lindemann, C., Wolter, C., Fischer, J. & Hölker, F. (2012). Aerial survey and spatial analysis of sources of light pollution in Berlin, Germany. *Remote Sensing of Environment*, *126*, 39–50.

[31] Hale, J. D., Davies, G., Fairbrass, A. J., Matthews, T. J., Rogers, C. D. F. & Sadler, J. P. (2013). Mapping lightscapes: Spatial patterning of artificial lighting in an urban landscape. *PLoS ONE*, *8*(5), e61460.

[32] Zhang, Q., Levin, N., Chalkias, C. & Letu, H. (2015). Nighttime light remote sensing: Monitoring human societies from outer space. In P. S. Thenkabail (Ed.), *Remote sensing of water resources, disasters, and urban studies* (pp. 289–312). Boca Raton, FL: CRC Press.

[33] DLR. (2017). N8 (Night/Nacht) mission idea. Internal DLR report, document ID N8-DLR-PLN-001: unpublished.

[34] Elvidge, C. D., Keith, D. M., Tuttle, B. T. & Baugh, K. E. (2010). Spectral identification of lighting type and character. *Sensors*, *10*(4), 3961–3988.

[35] Persistence of Vision Pty. Ltd. (2004). Persistence of Vision Raytracer, version 3.7. Computer software. Retrieved from http://www.povray.org/download/.

[36] Meyer-Arendt, J. R. (1968). Radiometry and photometry: Units and conversion factors. *Applied Optics*, *7*(10), 2081–2084.

[37] Donatello, S., Quintero, R. R., Caldas, M. G., Wolf, O., Van Tichelen, P., Van Hoof, V. & Geerken, T. (2019). *Revision of the EU Green Public Procurement criteria for road lighting and traffic signals*. Luxembourg: Publications Office of the European Union.

[38] Foster, J. L. & Hall, D. K. (1991). Observations of snow and ice features during the polar winter using moonlight as a source of illumination. *Remote Sensing of Environment*, *37*(2), 77–88.

[39] Lee, T. E., Miller, S. D., Turk, J., Schueler, C., Julian, R., Deyo, S., … Wang, S. (2006). The NPOESS VIIRS Day/Night visible sensor. *Bulletin of the American Meteorological Society*, *87*, 191–199.

[40] Cao, C. & Bai, Y. (2014). Quantitative analysis of VIIRS DNB nightlight point source for light power estimation and stability monitoring. *Remote Sensing*, *6*, 11915–11935.

[41] Galadí-Enríquez, D. (2018). Beyond CCT: The spectral index system as a tool for the objective, quantitative characterization of lamps. *Journal of Quantitative Spectroscopy and Radiative Transfer*, *206*, 399–408.

[42] Wyszecki, G. & Stiles, W. S. (1982). *Color science: concepts and methods, quantitative data and formulae* (2nd ed.). New York, Ny: Wiley.
[43] Elachi, C. & van Zyl, J. (2006). *Introduction to the physics and techniques of remote sensing* (2nd ed.). New York, NY: John Wiley & Sons.
[44] Schott, J. R. (2007). *Remote sensing: The image chain approach* (2nd ed.). New York, NY: Oxford University Press.
[45] Beirle, S., Lampel, J., Lerot, C., Sihler, H. & Wagner, T. (2017). Parameterizing the instrumental spectral response function and its changes by a super-Gaussian and its derivatives. *Atmospheric Measurement Techniques*, *10*, 581–598.
[46] Segl, K., Richter, R., Küster, T. & Kaufmann, H. (2012). End-to-end sensor simulation for spectral band selection and optimization with application to the Sentinel-2 mission. *Applied Optics*, *51*(4), 439–449.
[47] Fried, D. L. (1965). Noise in photoemission current. *Applied Optics*, *4*(1), 79–80.
[48] Eismann, M. T. (2012). *Hyperspectral remote sensing*. Bellingham, WA: SPIE Press.
[49] IMEC. (2019). CCD-in-CMOS TDI and multispectral TDI imaging. http://www.imec-int.com/en/specialty-CMOS-image-sensors.
[50] Akenine-Möller, T., Haines, E., Hoffman, N., Pesce, A., Iwanicki, M. & Hillaire, S. (2018). *Real-time rendering* (4th ed.). Boca Raton, FL: CRC Press.
[51] POV-Ray 3.7 documentation. (2019). Retrieved June 19, 2019, from http://www.povray.org/documentation/3.7.0/index.html
[52] Kajiya, J. T. (1986). The rendering equation. *ACM SIGGRAPH Computer Graphics*, *20*(4), 143–150.
[53] Pharr, M., Jakob, W. & Humphreys, G. (2017). *Physically based rendering: From theory to implementation* (3rd ed.). Cambridge: Morgan Kaufmann.
[54] Dutré, P., Bala, K. & Bekaert, P. (2006). *Advanced global illumination* (2nd ed.). Wellesley, MA: AK Peters.
[55] Lowe, D. G. (2004). Distinctive image features from scale-invariant keypoints. *International Journal of Computer Vision*, *60*(2), 91–110.
[56] Tapia, C., de Miguel, A. S. & Zamorano, J. (2017). LICA-UCM lamps spectral database, version 2.6. Unpublished manuscript.
[57] DIN. (2016). DIN EN 13201-2:2016-06 (E), road lighting - part 2: performance requirements. Standard.
[58] Leotek. (2019). GreenCobra series street and area lighting. https://leotek.com/greencobra/.
[59] Kieffer, H. H. & Stone, T. C. (2005). The spectral irradiance of the moon. *The Astronomical Journal*, *129*(6), 2887.
[60] Wehrli, C. (1985). *Extraterrestrial solar spectrum, publication no. 615*. Davos, Switzerland: Physikalisch-Meteorologisches Observatorium and World Radiation Center.
[61] Johnston, J. M., Wooster, M. J. & Lynham, T. J. (2014). Experimental confirmation of the MWIR and LWIR grey body assumption for vegetation fire flame emissivity. *International Journal of Wildland Fire*, *23*, 463–479.

[62] Kokaly, R. F., Clark, R. N., Swayze, G. A., Livo, K. E., Hoefen, T. M., Pearson, N. C., … Klein, A. J. (2017). *USGS spectral library version 7: U.S. Geological Survey Data Services 1035*. Reston, VA: U.S. Geological Survey.

[63] Mayer, B. & Kylling, A. (2005). The libRadtran software package for radiative transfer calculations-description and examples of use. *Atmospheric Chemistry and Physics*, *5*(7), 1855–1877.

[64] Mayer, B., Kylling, A., Emde, C., Buras, R., Hamann, U., Gasteiger, J. & Richter, B. (2017). LibRadtran user's guide. http://www.libradtran.org/doc/libradtran.pdf.

[65] Bailey, A. W. & Anderson, M. L. (1980). Fire temperatures in grass shrub and Aspen forest communities of Central Alberta. *Journal of Range Management*, *33*(1), 37–40.

[66] Plank, S., Fuchs, E. M. & Frey, C. (2017). A fully automatic instantaneous fire hotspot detection processor based on AVHRR imagery - a TIMELINE thematic processor. *Remote Sensing*, *9*(1), 30.

[67] Eloholma, M., Ketomäki, J. & Halonen, L. (2004). *Luminances and visibility in road lighting - conditions, measurements and analysis*. Espoo, Finland: Helsinki University of Technology.

[68] Narisada, K. & Schreuder, D. (2004). *Light pollution handbook*. Dordrecht, Netherlands: Springer.

[69] van Bommel, W. (2015). *Road lighting: Fundamentals, technology and application*. Cham, Switzerland: Springer.